LCH Laboratoire de Constructions Hydrauliques
Laboratory of Hydraulic Constructions

ÉCOLE POLYTECHNIQUE
FÉDÉRALE DE LAUSANNE

Communication 75

Geomorphic work by gravity currents with varying initial conditions

Jessica Zordan

Editeur : Prof. Dr A. Schleiss

Lausanne, 2018

Communications du Laboratoire de Constructions Hydrauliques ISSN 1661-1179
Ecole Polytechnique Fédérale de Lausanne
Editeur: Prof. Dr A. Schleiss

Le rêve, c'est tout –
la technique, ça s'apprend.

— *Jean Tinguely*

To my family.

Preface

Gravity currents are density-driven flows which can have a high sediment transport capacity. When occurring in reservoirs, lakes and in oceans, significant geomorphic changes may occur at the bottom. The coupling between the hydrodynamics of the gravity current and sediment transport capacity is still not well known. Above all there is a lack of knowledge regarding the circulation pattern inside the currents. With her experimental research work, using advanced measurement techniques, Dr Jessica Zordan made several novel contributions answering the following question:

- What are the characteristic features in the head and body regions of a gravity current generated with the lock-exchange method and which is a common structure of the inherent vortical movements?
- With which parametrization the entrainment from the bottom can be defined taking into account the spatio-temporal variability of the gravity currents?
- Which mechanisms govern the entrainment, transport and deposition of sediment and how the hydrodynamic of the gravity currents produces geomorphic changes on a mobile bed?
- Is there an interaction between the gravity current and the entrained sediment?
- How the turbulent structure of the gravity current influences the deposition of entrained sediments?

By answering the above questions, Dr. Zordan could give new insights on the behavior of gravity currents flowing over a mobile bed. We would like to thank the members of PhD committee, Prof. Benjamin Kneller, University of Aberdeen, United Kingdom; Dr. Benoit Spinewine, Fugro Company, Bruxelles, Belgium and Dr. Damien Bouffard, Eawag, Switzerland for their valuable comments. Finally, we also gratefully thank the European Marie Curie Actions under project SEDITRANS for their financial support.

Lausanne, 15 Mai 2018 Prof. Dr. Anton Schleiss and Prof. Dr. Mario Franca

Contents

Abstract

Gravity currents are density-driven flows that are able to transport high amounts of sediment and are responsible of great geomorphic changes. Moreover they can have severe repercussions on the environment since they are conveyors of substances, e.g. pollutants, for long distances depending on their flow dynamics. The latter are determined by the release conditions and by the exchange at the upper and lower boundaries. The aim of this research study is to characterize the turbulent structure of gravity currents, as a consequence of the initial release conditions, to relate with their transport capacity.

For this purpose, saline gravity currents are experimentally created in a laboratory channel through the lock-exchange technique. Different initial conditions, representing different configurations that can be found in reality, are considered during the experiments. The tested parameters are: initial buoyancy of the current in the lock, initial volume of release (i.e. lock-length), lock slope and grain sizes of the sediment that form an erodible bed over which the current flows.

High-resolution velocity measurements, performed with an Acoustic Doppler Velocity Profiler (ADVP), allowed to describe both horizontal and vertical structures of the gravity currents. A universal criterion is established to isolate head and body of the current which are characterized by different dynamics and their extensions vary in relation with the conditions of release. A new parametrization, based on the computed temporal evolution of shear stress, allows to quantify water entrainment from the upper interface and sediment erosion capacity at the bottom.

The effect of the increment of gravitational forces on its erosion capacity is tested by introducing a slope in the lock reach. The range of considered slopes goes from horizontal to S=16%. This latter is identified as a transient case in which two mechanisms compete i.e. on one side, the current entrains more water from the upper interface due to the increment of friction, the current expands, dilutes and therefore slows down; on the other side, the head is fed by the faster rear steady current thus inducing an acceleration.

At the bottom, high shear stress associated with intense ejection and burst events influence erosion and bed load transport. The coupling of hydrodynamic mechanisms and processes of erosion, transport and deposition of sediment are investigated. It is shown that the upward motion, caused by mean and turbulent velocity components, promote vertical mixing of sediment from the channel bed. The feedback between the hydrodynamics of a gravity current and the geomorphic changes of a mobile bed are analysed. The shape of the front changes due to sediment entrainment and the deposition of sediment downstream creates characteristic

patterns whose geometry reflect the coherent turbulent structure of the current.
The scientific contributions elaborated in this research project allow to ameliorate the modelling of these flows, describing their inherent complex mechanisms under various initiation conditions and the interaction with suspended material. This helps to formulate adapted mitigation measures for the retention of these phenomena which frequently have a negative effect and e.g. induce reservoir sedimentation, subaqueous structure damages and scour processes in the vicinity of submerged pipelines or exacerbate pollutants dispersion.

KEY WORDS: gravity current, current shape, lock-length, lock-slope, transport capacity, mixing processes, ambient fluid entrainment, sediment entrainment, bed shear stress, instantaneous velocities, deposition patterns.

Résumé

Les courants de gravité sont des écoulements induits par la poussée hydrostatique entre deux fluides qui est causée par une différence de densité. Quand ces courants se reproduisent sur un lit mobile, ils peuvent transporter de grandes quantités de sédiments en créant des changements géomorphologiques importants. Ils peuvent aussi avoir des conséquences sur l'environnement vu que des substances, comme les polluants, pourraient être transportées avec le fluide qui compose le courant, en suivant donc leur dynamique. Cette dernière est déterminée par les conditions initiales de rejet et par l'échange qui se produit à l'interface supérieure, en contact avec le fluide ambiant, et au fond, avec les sédiments. L'objectif de cette recherche est de caractériser la structure turbulente des courants de gravité et de lier cela avec la capacité de transport des courants.

Des courants salins ont été reproduits expérimentalement dans un canal à section rectangulaire, grâce à la technique 'lock exchange'. Plusieurs conditions initiales, qui représentent différentes situations réelles, ont été reproduites lors des essais. Les paramètres testés sont : la poussée hydrostatique et le volume initiaux dans la première partie du canal (qui est nommée 'lock'), l'inclinaison du lock et la dimension des sédiments qui composent le lit mobile.

Des mesures de vitesses instantanées à haute résolution dans les trois directions ont été mesuré avec l'ADVP (Acoustic Doppler Velocity Profiler). Celles-ci ont permis de décrire entièrement l'hydrodynamique des courants le long de la verticale et aussi longitudinalement. Un critère universel a été établi pour identifier les deux régions qui composent le courant, la tête et le corps, qui sont caractérisés par des dynamiques propres et dont les extensions varient en raison des conditions initiales. Une nouvelle paramétrisation, qui se base sur les mesures dans le temps des forces de cisaillement, a permis l'estimation de l'entrainement d'eau depuis l'interface supérieure et de l'érosion de sédiments du fond.

L'effet des forces gravitationnelles sur la capacité d'érosion des courants a été testé avec un faux-fond qui crée une pente dans le lock. Les pentes testées vont de l'horizontale jusqu'à S=16%. Ce dernier identifie un cas de transition, où deux phénomènes se reproduisent : d'un coté le courant entraine plus d'eau depuis l'interface supérieure à cause de l'augmentation du frottement, induisant son expansion, sa dilution et, en conséquence, son ralentissement ; de l'autre coté le fluide composant le corps, plus rapide, s'accumule dans la tête du courant en causant son accélération.

Au fond, le cisaillement élevé combiné à des mouvements turbulents typiques du phénomène "bursting" influence l'érosion, le transport et la déposition de sédiments. Il a été démontré que les mouvements verticaux, en termes de vitesses moyennes et fluctuations turbulentes,

favorisent le déplacement vertical des sédiments du lit mobile. L'interaction entre l'hydrodynamique des courants de gravité et les changements morphologiques a été analysée : la forme du courant change à cause de l'entrainement de sédiments et les sédiments se déposent à l'aval en créant des géométries qui sont induites par les structures turbulentes du courant. Pour avoir une modélisation de ces courants, capable de décrire les mécanismes internes complexes du fluide et l'interaction avec les sédiments, une étude systématique a été faite. Cette dernière est à la base de la formulation de mesures de protection contre les phénomènes induits par les courants qui créent fréquemment des problèmes, notamment la sédimentation des réservoirs, des dégâts suite à l'impact avec des structures ou encore des problèmes de stabilité due à l'érosion qu'ils provoquent à proximité des conduites situées au fond des océans.

MOTS CLEFS : courants de gravité, forme du courant, longueur du lock, pente du lock, capacité de transport, processus de mélange, entrainement de fluide ambient, entrainement des sédiments, cisaillement au fond, vitesses instantanées, géométries de déposition.

Kurzfassung

Dichteströmungen sind Strömungen die bei einem Dichteunterschied zwischen zwei Flüssigkeiten auftreten. Sie können grosse Mengen an Sediment transportieren und sind verantwortlich für bedeutende geomorphologische Veränderungen. Zudem können sie schwerwiegende Auswirkungen auf die Umwelt haben, da sie Substanzen, wie beispielsweise Schadstoffe über grosse Distanzen befördern können. Geomorphologische Veränderungen werden durch die Freisetzungsbedingungen und durch den Austausch an den oberen und unter Phasengrenzen bestimmt. Ziel dieses Forschungsprojektes ist es, die Turbulenzstruktur von Dichteströmungen infolge initialer Freisetzungsbedingungen zu charakterisieren und diese mit der Sedimenttransportkapazität solcher Strömungen zu verbinden.

Zu diesem Zweck wurden salzhaltige Dichteströmungen in einem Laborkanal mit der “lock-exchange” Methode ausgelöst. Verschiedene Anfangsbedingungen, welche diverse reale Bedingungen darstellen, wurden während der Versuchsreihe untersucht. Dabei wurden folgende Parameter studiert: initiale Dichte der Flüssigkeit hinter dem Kanalverschluss (“lock”), freigesetztes Volumen, Neigung der Kanalsohle hinter dem Verschluss sowie die Korngrösse der Sedimente, welche zur Nachbildung einer erodierbaren Kanalsohle verwendet wurden.

Hochauflösende Fliessgeschwindigkeitsmessungen, durchgeführt mit einem “Acoustic Doppler Velocity Profiler” (ADVP), erlaublen die horizontalen und vertikalen Strukturen der Dichteströmung zu untersuchen. Ein allgemein gültiges Kriterium konnte definiert werden, mit welchem die Front und der hintere Teil der Dichteströmung voneinander getrennt werden können. Dieser Trennbereich ist durch grosse Dynamik gekennzeichnet und zudem ist er stark von den Freisetzungsbedingungen abhängig. Eine neue Parametrisierung, basierend auf der zeitlichen Entwicklung der aus den Geschwindigkeitsmessungen berechneten Scherspannungen, ermöglichte es den Wassereintrag an der oberen Phasengrenze und die Erosionskapazität des Kanalbetts zu quantifizieren.

Der Effekt der potentiellen Energie auf die Erosionskapazität wird mittels einer Sohlenneigung des Bereichs hinter dem Kanalverschluss untersucht. Die betrachteten Neigungen reichen von horizontal bis hin zu einer Neigung von 16% für welche sich ein Übergangszustand einstellt. Zwei gegensätzliche Phänomene treten gleichzeitig auf: Einerseits trägt der Dichtestrom durch die erhöhte Scherspannung mehr Wasser von der oberen Phasengrenze ein, was zu einer Ausdehnung und einer geringeren Dichte und somit zu einer Verlangsamung führt. Andererseits wird die Front des Dichtestromes durch den schnelleren hinteren Teil beschleunigt.

An der Unterseite des Dichtestromes beeinflussen hohe Scherspannungen die Turbulenzstrukturen, welche typisch für die Wirbelablösungen (auch "Burst"genannt), die Erosion und

den Sedimenttransport sind. Dabei wird die Kopplung der hydrodynamischen Mechanismen mit Erosion, Transport und Deposition untersucht. Es wird aufgezeigt, dass die Aufwärtsbewegung durch die zeitlich gemittelte Geschwindigkeit und die Turbulenzkomponenten eine vertikale Vermengung der Sedimente vom Kanalbett fördert. Die Rückkopplung zwischen der Hydrodynamik von Dichteströmungen und der geomorphologischen Veränderungen eines mobilen Bettes werden analysiert. Die Ausprägung der Front verändert sich durch den Sedimenteintrag und die Absetzung stromabwärts führt zu charakteristischen Ablagerungsmuster deren Geometrie die kohärente Struktur der Strömung wiederspiegeln.
Die wissenschaftlichen Beiträge, welche in diesem Forschungsprojekt erarbeitet wurden, ermöglichen eine verbesserte Nachbildung von Dichteströmungen durch die Beschreibung deren inhärenter komplexer Mechanismen unter verschiedenen Anfangsbedingungen und der Interaktion der Strömungen mit freischwebender Materie. Dies hilft geeignete vorbeugende Massnahmen zu treffen um negative Auswirkungen von Dichteströmungen, wie zum Beispiel Stauseeverlandung, Beschädigung von Unterwasserbauten oder Kolkbildung nahe von Unterwasserleitungen, zu verhindern.

SCHLÜSSELWÖRTER: Dichtestrom, Stromausprägung, “Lock”-Länge (Freisetzungslänge), “Lock”-Neigung, Sedimenttransportkapazität, Vermengungsprozess, Wassereintrag, Sedimenteintrag, Scherspannung, momentane Strömungsgeschwindigkeit, Sedimentablagerungsmuster.

Riassunto

Le correnti di densità (o di gravità) possono trasportare ingenti quantità di sedimenti e sono dunque responsabili di alterazioni geomorfologiche importanti. Possono inoltre avere gravi conseguenze sull'ambiente dato che sono in grado di trasportare sostanze, come per esempio inquinanti, per chilometri, a seconda delle condizioni idrodinamiche della corrente stessa. Quest'ultime sono dettate dalle condizioni di rilascio e dall'interazione all'interfaccia superiore con il fluido ambiente e all'inferiore con il fondo. Lo scopo di questa ricerca è caratterizzare la struttura turbolenta delle correnti di gravità che si crea in seguito a determinate condizioni di rilascio, per poter trovare una relazione tra l'idrodinamica delle correnti e la loro capacità di trasporto.

In questo progetto di ricerca, le correnti di gravità saline sono state ricreate sperimentalmente, in un canale a sezione rettangolare, attraverso la tecnica del 'lock-exchange'. Sono state simulate molteplici condizioni iniziali, riproducendo in questo modo diverse configurazioni reali. I parametri testati sono : la forza idrostatica iniziale e il volume iniziale del fluido più denso, l'inclinazione della prima parte del canale a monte e la granulometria dei sedimenti che compongono il letto mobile.

L'ADVP (Acoustic Doppler Velocity Profiler) è lo strumento utilizzato per misurare le velocità istantanee nelle tre direzioni, permettendo una descrizione completa del flusso lungo la verticale e longitudinalmente. È stato stabilito un criterio generale per identificare in modo univoco la testa e il corpo della corrente. Queste due zone sono charatterizzate da una idrodinamica peculiare e la loro estensione varia con le condizioni di rilascio. Una nuova parametrizzazione, basata sulla stima dello stress di taglio, ha permesso di quantificare l'ammontare d'acqua inglobata nella corrente all'interfaccia superiore e la quantità di sedimenti erosi dal fondo.

L'effetto dell'aumento delle forze gravitazionali nella capacità di erosione della corrente è stato testato introducendo un doppio-fondo inclinato nella prima parte del canale a monte (chiamato 'lock'). Le pendenze testate sono comprese tra l'orizzontale e S=16%. A questa pendenza si verifica un comportamento transitorio : da un lato, la corrente ingloba più acqua dall'interfaccia superiore a seguito dell'aumento dell'attrito, espande ed è diluita, causandone il rallentamento ; dall'altro lato, nella testa si accumula il fluido che compone il corpo che è più veloce, e la corrente subisce dunque un'accelerazione.

Al fondo, alti valori di sforzi di taglio sono associati a intensi e rapidi eventi di espulsione, oscillazioni improvvise e rotture del fluido (secondo un processo chiamato 'burst' di parete o scoppio), che influenzano l'erosione e il trasporto di fondo. Si è studiata l'interazione tra idrodinamica della corrente e processi di erosione, trasporto e deposizione dei sedimenti. Si

è dimostrato che la componente verticale del moto, flusso medio e turbolento, promuove il sollevamento verticale dei sedimenti dal letto mobile. È stata inoltre analizzata la relazione tra idrodinamica e variazioni morfologiche : il fronte della corrente cambia forma dopo aver incorporato i sedimenti e, a valle, i sedimenti depositano seguendo una geometria che rispecchia le stutture turbolente della corrente.
Per poter modellare accuratamente queste correnti, capire la complessa fluidodinamica che li caratterizza e il ruolo che svolgono nel trasportare massa, energia e quantità di moto, è stato condotto uno studio sistematico che analizza lo sviluppo delle correnti in seguito a varie condizioni iniziali e in presenza di sedimenti. Questo studio costituisce una prima fase necessaria per poter in futuro formulare misure di protezione adeguate contro i fenomeni indotti dal passaggio delle correnti come ad esempio l'interrimento degli invasi, danni su strutture marittime in seguito all'impatto o all'erosione in prossimità di condotte o la dispersione degli inquinanti.

PAROLE CHIAVE : corrente di gravità, forma della corrente, lunghezza del lock, inclinazione del lock, capacità di trasporto, processi di mescolamento, incorporazione del fluido ambiente, erosione dei sedimenti, sforzo di taglio al fondo, velocità istantanee, geometrie di deposizione.

List of Figures

List of Symbols

Roman Symbols

Symbol	Definition	Units
A, B	coefficients of the log fit	–
A_{ER}	total surface of the mobile bed	m^2
$A_{ER,i}$	area i in which the mobile bed is subdivided	m^2
$A_{D,i}$	area of the channel adjacent to C_i	m^2
c	speed of sound	m/s
C	constant of integration	–
Cz	dimensionless Chezy coefficient	–
C_i	cross section i recorded with the laser	–
D_{10}	characteristic grain size of the 10& in mass of the sample	μm
D_{50}	characteristic grain size of the 50& in mass of the sample	μm
D_{90}	characteristic grain size of the 90& in mass of the sample	μm
D_m	sediments diameter in the model	m
D_p	sediments diameter in the prototype	m
e	thickness of deposit	mm
$E\&T$	Ellison and Turner current height	m
e_w	coefficient of ambient water entrainment	–
f_D	Doppler frequency	Hz
f_e	frequency of the emitted wave	Hz
f_{elong}	shape factor for streak shape elongation	–
f_r	frequency of the received wave	Hz
Fr_D	densimetric Froude number	–
g	acceleration due to gravity	ms^{-2}
g'	reduced gravity	ms^{-2}
g'_0	initial reduced gravity	ms^{-2}
H	total water height	m

Symbol	Definition	Units
h	general height	m
h_0	initial fluid depth in the lock	m
h_b	bulk height of the current	m
h_c	gravity current height	m
h_i	inner layer height	m
h_m	mixing zone height	m
H_m	model water height	m
h_{max}	height of the maximum velocity	m
$H(t)$	kinematic function $H(t) = u_d(t)h(t)$	m^2/s
H_p	prototype water height	m
k	von Kármán constant	–
K	eddy viscosity	m^2/s
k_s	skin roughness	mm
l	turbulent mixing length	m
L_i	lock-length i	m
L_b	non-dimensional length of the body	–
L_h	non-dimensional length of the head	–
L_p	observation position from the gate	m
m	number of observations	–
n	number of longitudinal sections recorded with the laser	–
p	pressure	Pa
$\overline{p}$	time averaged pressure	Pa
p'	pressure turbulent fluctuation	Pa
R	aspect ratio of the denser volume	–
R^2	coefficient of determination	–
Re	Reynolds number	–
Re_0	initial Reynolds number	–
Re_D	densimetric Reynolds number	–
Re_{part}	particle Reynolds number	–
Ri	Richardson number	–
Ri_b	bulk Richardson number	–
S	slope	–
Sk	Stokes number	–
t	time	s

Symbol	Definition	Units
T_0	initial temperature in the lock	$°C$
t^*	time scale	s
T_a	initial temperature of the ambient water	$°C$
T_i	limit of integration	s
u	instantaneous streamwise velocity	m/s
$\overline{u}$	time averaged streamwise velocity	m/s
u'	streamwise turbulent fluctuation	m/s
$u'w'_d$	depth-averaged Reynolds stress	m^2/s^2
U	height-averaged streamwise velocity	m/s
u_0	initial buoyancy velocity	m/s
u_*	friction velocity	m/s
u_b	buoyancy velocity	m/s
u_c	characteristic velocity of the current	m/s
u_d	depth-averaged streamwise velocity	m/s
$<u_d>$	ensemble average of instantaneous depth-averaged streamwise velocity	m/s
u_f	front velocity	m/s
U_m	model height-averaged streamwise velocity	m/s
U_{max}	maximum streamwise velocity	m/s
U_p	prototype height-averaged streamwise velocity	m/s
u'_{RMS}	root-mean square streamwise velocity fluctuation	m/s
u_z	mean velocity at elevation z	m/s
v	instantaneous lateral velocity	m/s
V	voltage recorded by the laser	V
V_a	volume of entrained ambient water	m^3
V_{eroded}	eroded volume	mm^3
V^*_{eroded}	dimensionless eroded volume	$-$
V_i	volume of mixture in the lock with length L_i	m^3
V_p	volume available for the propagation of the release until the observation position	m^3
v_s	settling velocity	m/s
v_{s_m}	model settling velocity	m/s
v_{s_p}	prototype settling velocity	m/s
w	instantaneous vertical velocity	m/s
$\overline{w}$	time averaged vertical velocity	m/s

Symbol	Definition	Units
w'	vertical turbulent fluctuation	m/s
w_d	depth-averaged vertical velocity	m/s
$\overline{w_d}$	depth-averaged vertical mean velocity	m/s
$<w_d>$	ensemble average of instantaneous depth-averaged vertical velocity	m/s
w'_d	depth-averaged vertical velocity fluctuation	m/s
w'_{RMS}	root-mean square vertical velocity fluctuation	m/s
x	longitudinal spatial coordinate	m
y	lateral spatial coordinate	m
z	vertical spatial coordinate	m
z_0	zero velocity vertical level	m
Z_{BED}	longitudinal section recorded with the laser	
	on the mobile bed $before$ and $after$ the passage of the current	mm
z_u	maximum upper vertical position for the log fit	m

Acronyms

Symbol	Definition
$ADVP$	Acoustic Doppler Velocity Profiler
$EPFL$	École Polytechnique Fédérale de Lausanne
LCH	Laboratoires de Constructions Hydrauliques
LTP	Labortoire de Technologie des Poudres
RGB	Red Green Blue
TPU	Thermoplastic Polyurethane

Greek Symbols

Symbol	Definition	Units
α	angle of inclination of the channel bed	$^\circ$
α, β	angle of inclination of emitter and receivers in the ADVP	rad
δ_b	characteristic height of the body	m
δ_h	characteristic height of the head	m
ΔT	temperature difference mixture-ambient water	$^\circ C$
$\Delta\rho$	density excess	kg/m^3
Δx	distances in x-direction between velocity measurements points	m
Δz	distances in z-direction between velocity measurements points	m
Δy_{AVE}	average thickness of the streaks	mm
Δz_{MAX}	maximum amplitude of deposition	mm
η_y	spanwise vorticity	s^{-1}
λ_e	wavelength of the emitted acoustic wave	m
λ_r	wavelength of the received acoustic wave	m
λ_{v_s}	velocity scale ratio	–
μ	dynamic viscosity of the water	$kg/(ms)$
μ_c	dynamic viscosity of the saline mixture	$kg/(ms)$
ν	kinematic viscosity	m^2/s
ν_c	kinematic viscosity of the saline mixture	m^2/s
θ	angle formed by the line representing the evolution of the current from video analysis	rad
Φ	entrainment capacity	–
Φ_b	bottom entrainment capacity	–
$\Phi_{b\ body}$	bottom entrainment capacity due to the body	–
Φ_m	interfacial entrainment capacity	–
ρ_0	gravity current initial density	kg/m^3
ρ_a	ambient fluid density	kg/m^3
$\rho_{s\ m}$	sediment density in the model	kg/m^3
$\rho_{s\ p}$	sediment density in the prototype	kg/m^3
ρ_c	gravity current density	kg/m^3
$\rho\overline{u'w'}$	Reynolds stress	Pa
τ	shear stress	Pa
τ_b	bed shear stress	Pa
τ_b^*	normalized bed shear stress	–

Symbol	Definition	Units
τ_{DEF}	bed shear stress by definition	Pa
τ_{LOG}	bed shear stress from log-law	Pa
τ_m	interface shear stress	Pa
$\tau_{x,z}$	shear stress in the xz plane	Pa

1 Introduction

1.1 General overview and motivation

1.1.1 Nature of gravity currents

Gravity or density currents are buoyancy-driven flows that occur naturally or as a consequence of human activities (Simpson, 1997). Difference in hydrostatic pressure at the surface of contact between two fluids of different densities causes the formation of a flow where the denser fluid travels along the lower boundary while the lighter fluid flows above, in the opposite direction (Hacker et al. (1996) and Shin et al. (2004)). The density difference can be generated in two ways: (i) by a property of the fluid (e.g. temperature or salinity) causing **compositional gravity currents** (Ooi et al., 2009) or (ii) by the presence of particles in suspension, which increase the bulk density of the surrounding fluid, and in this case we refer to **turbidity currents** (Parker et al. (1986), Meiburg and Kneller (2010)). Gravity currents are first of all a geophysical flow, but these currents are also of importance in engineering applications, such as industrial flows (e.g. the sheet glass production in Figure 1.1, Lyn et al. (1992), Zhou et al. (1994)), and for environmental security (Huppert and Woods (1995), Fernández-Torquemada et al. (2009), Al-Majed et al. (2012)), because they play a fundamental role in the dispersion of the pollutants.

1.1.2 Occurrence of compositional gravity currents

In the atmosphere, examples of natural compositional gravity currents driven by differences in temperature include katabatic winds: flows developing downslope originated by radiational cooling of air on the top of a mountain. The side effect of this type of wind is that they lead to thermal inversion which can reduce the vertical mixing. Their relation with the accumulation of pollutants in some highly industrialized cities is a prevailing research topic (Ainslie and Jackson (2009), Ramšak et al. (2013)).

Examples of anthropogenic compositional gravity currents caused by dissolved substances are the release of pollutants into rivers, oil spillage in the ocean (Figure 1.1) and desalination plant outflows. The release of pollutants into rivers has severe negative environmental impacts mainly in relation to the ability of the waste fluid containing contaminants to disperse and propagate, even for long distances, flowing as a gravity current (Huppert and Woods, 1995). Oil spillage events are numerous and each year, there is an average of 5 millions tons of petroleum transported across the seas (Al-Majed et al., 2012). The heavier seawater carrying the lighter oil travels underwater horizontally as a gravity current, and it spreads making more difficult the cleaning up process due to the high dispersion of contaminant. In the case of the desalination plants, if on one side they produce new water resources, on the other side they increase the pressure on the marine environment (Fernández-Torquemada et al., 2009): hypersaline outflows disperse moving as a dense brine and can causes hypoxia of the aquatic fauna and issues for freshwater human consumption, when these releases are in the vicinity of an estuary and arrive to affect the groundwater table (Valle-Levinson, 2010). At the estuary

an alteration of the equilibrium is due to the so-called "inverse estuary": typically in subtropical and Mediterranean climates, when evaporative fluxes exceed freshwater inputs, salinity increases beyond oceanic values (Hodges et al., 2010). Water density is thus higher close to the surface inducing the denser water to spread in both the seaward and landward direction with consequent problems related to water quality (Valle-Levinson, 2010) and desalination plants may exacerbate these problems.

Recently, the hydrodynamic of dense plumes have been considered inversely as an advantage and their possible exploitation for carbon sequestration is under evaluation. Oceans are sinks for CO_2: the carbon accumulation in oceans is a natural ongoing process. The possibility of direct injecting dense plumes containing high concentration of CO_2 in deep seas, forming a sinking bottom gravity current, has been investigated by Herzog et al. (2001) as a solution for reducing the atmospheric CO_2.

1.1.3 Occurrence of turbidity currents

Lava flows, dust storm, snow avalanches, volcano eruptions, turbidity currents (Figure 1.1) are some examples of flows where suspended particles drive the density gradient. Sediment transport induced by gravity currents is of significant implications for aquatic ecosystems, since they are determinant to habitats for benthic organisms and they carry nutrients needed to the ecosystem, as well as for sustainable engineering applications (e.g. the erosion localized at hydraulic structures or beach nourishment) (Salim et al., 2017). Recently, turbidity currents originated by the presence of sediments in suspension, are becoming a subject of discussion due to their relation with reservoir sedimentation (Schleiss et al., 2016). When sediment-laden water enters an impoundment, plunges beneath the clear water (Knoblauch, 1999), and travels downstream along the submerged thalweg, it can, when strong enough, erode and transport considerable sediment volumes within the reservoir itself (Parker et al. (1986), De Cesare and Schleiss (1998)). Travelling downstream, it deposits the coarser part of sediments along the bottom, and if it reaches the dam, it accumulates to form a submerged muddy lake, causing the loss of storage capacity, a potential risk of blockage of intake structures and the eventual accumulation of polluting materials. The sustainable management of dams is thus a widely treated field of research in literature due to the important ecological and economic consequences (Palmieri et al., 2001) and the variety of techniques that are under study for sediment evacuation (Chamoun et al. (2016a), Chamoun et al. (2017b).

1.1.4 Knowledge gaps

The occurrence of density-driven flows in nature is well documented in literature but in few cases in situ measurements of these events were possible due to their destructive nature (Paull et al. (2002) and Xu et al. (2004), among others). Density-driven flows have implications on the environment since they are conveyors of particles or substances depending on their flow dynamics, which is affected by the release conditions and by the exchange at the upper

Figure 1.1: Examples of natural and anthropogenic gravity currents. a) Lava flows in Hawaii. Photo Credit: Stéphanie Demuth; b) Eruption at Eyjafjallajökull vulcano April 17, 2010. Photo Credit: Árni Friðriksson, Eyjafjallajokull-April-17, CC BY-SA 3.0; c) Sediment transported down the Rhone River into Lake Geneva. Photo Credit: Rama (https://commons.wikimedia.org/wiki/File:Leman_img_0571.jpg); d) Oil spilled after the Deepwater Horizon/BP well blowout in the Gulf of Mexico in April 2010. Photo Credit: NOAA; e) Dust storm called a Haboob, moving across the Llano Estacado toward Yellow House Canyon near the residential community of Ransom Canyon, Texas. Photo Credit: Leaflet (https://commons.wikimedia.org/wiki/File:Haboob_Ransom_Canyon_Texas_2009.jpg); f) Sheet glass production (http://www.miralglass.com).

and lower boundaries. Therefore, gravity currents have been an important research topic for numerous disciplines and they have been reproduced both numerically by Ooi et al. (2009), Tokyay et al. (2011), Lombardi et al. (2015), Ottolenghi et al. (2016b) and experimentally by Britter and Linden (1980), Huppert and Simpson (1980), Altinakar et al. (1990), García and

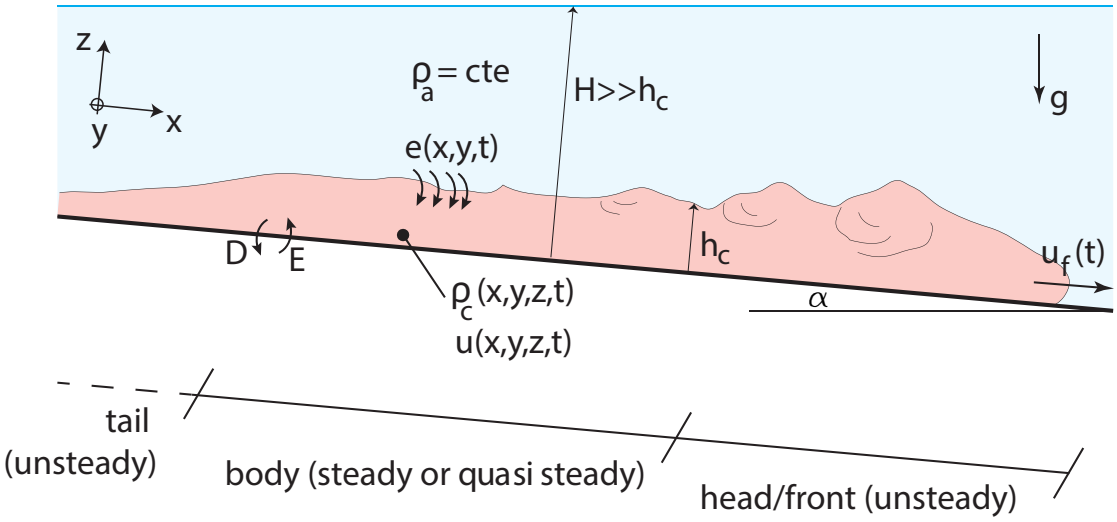

Figure 1.2: Sketch of a bottom gravity current with density ρ_c intruding in the less dense ambient fluid with uniform density ρ_a (Franca, 2017). The gravity current can flow on an inclined of slope α with a certain front velocity u_f. Mainly in the quasi steady body, it develops a streamwise velocity profile (u) and a density profile (ρ_c). Ambient fluid is entrained at the upper interface (e), in presence of a mobile bed, exchange takes place, with erosion (E) and deposition (D) of material.

Parker (1993), Shin et al. (2004), Nogueira et al. (2013), Theiler and Franca (2016) among others (see also Adduce and Franca (2018) for several examples of research on buoyancy driven flows).

Authors agree on describing the shape of the gravity current as composed by an arising highly turbulent front, called head, followed by the body and in some cases a tail is present. A vertical structure can be distinguished as well. A current composed of dense fluid presents two main surfaces: at the bottom, since it generally flows on a solid boundary, and at the top, at the interface with the lighter fluid (see Figure 1.2). These are active boundaries indeed mass and momentum exchanges are promoted at the bed and at the upper interface (Ancey, 2012). Ambient fluid is entrained due to shear and buoyancy instabilities at the upper interface (Cantero et al., 2008) resulting in the dilution of the underlying current and modifying the density profile which characterizes a gravity current under stable density stratification (Turner, 1973a). Bulk quantities can be used to estimate the mixing rate and the entrainment parametrization so far widely used comes from the work of Ellison and Turner (1959), however, the evaluation of mixing and entrainment in unsteady gravity currents is still an open issue (Ottolenghi et al., 2016a). The detail of circulation inside the current have still to be further explored in fact, even if estimating the rate of entrainment is useful, this does not indicate the extent of the mixing within the current (Hacker et al., 1996). Knowing how the heat, salt or pollution distribute in a gravity current, as a consequence of its turbulent structure and of the interaction at the top free surface and the bottom boundary, is fundamental as mixing affect the evolution of the

flow (Hacker et al., 1996).

When the gravity current travels above an erodible bed, entrainment of material from the bottom can take place, which is conveyed with the current and deposited even at large distances from their original position. Gravity currents can transport sediments or substances, e.g. pollutants, in dependence with their structure and dynamics. High shear stress associated with intense ejection and burst events influence erosion and bed load transport (Niño and Garcia (1996), Cantero et al. (2008), Salim et al. (2017)). Thus, it is of fundamental importance to understand what the hydrodynamic structure of gravity currents tell about their transport capacity.

In order to properly model these flows, describing their inherent complex mechanisms under various initial conditions and accounting for their interaction with suspended material, a comprehensive understanding is needed. This will help to formulate adapted mitigation measures to handle these phenomena which frequently result in catastrophic effects.

1.2 Research questions

In nature, the majority of gravity currents occur on complex topographies and flow over various bed compositions. The erosion, transport and deposition processes depend on the particle characteristics and on the flow hydrodynamics. The literature on gravity currents is rich, however, the hydrodynamics of density-driven flows, namely, the internal flow structure, are still not completely understood. Moreover, the coupling of hydrodynamic mechanisms and sediment transport processes have so far seldom been investigated.

Based on previous knowledge, it is hypothesized that the processes of sediment erosion, transport and deposition are governed by hydrodynamic variables such as bed shear stress, Reynolds shear stresses and the vertical component of the flow velocity (mean and fluctuating field). In this research the goal is to go further and to determine to which extent these hydrodynamic quantities of gravity currents are correlated with the sediment dynamics, which is still unknown. Furthermore, the current hydrodynamics are determined by the triggering initial conditions such as buoyancy, initial released volume and slope of the release. Their influence is tested through a parametric analysis: two groups of tests are performed aiming at systematically varying these parameters. Moreover, this has allowed to determine the best configuration for testing gravity currents flowing on a mobile bed and to identify a proper parametrization for estimating the potential entrainment.

More specifically, this research intends to answer the following questions, that are here divided into three main categories which correspond to the main chapters of the report.

Chapter 4 - Horizontal and vertical structure of gravity currents produced by varying initial volume of release

Q1 How can the head and body regions of a gravity current generated by lock-exchange method be defined and which are their characteristic features?

Q2 Which is a common structure of the inherent vortical movements of lock-released gravity currents and how does this affect the mass and momentum exchange?

Q3 Which parametrization can be adopted to quantify entrainment from the upper and lower layers that takes into account the spatio-temporal variability of the gravity currents?

Chapter 5 - Influence of incremental gravitational forces on the gravity current hydrodynamics

Q4 How does gravitational force, increased by the presence of a slope in the lock, affect ambient water entrainment and potential erosion capacity? How is the current shape modified?

Chapter 6 - Gravity currents flowing over mobile bed

Q5 Which are the mechanisms governing the entrainment, transport and deposition of sediment and how the hydrodynamic of the gravity currents act to induce geomorphic changes on a mobile bed? Which is the feedback process on the gravity current generated by the incorporation of entrained sediment?

Q6 How is the downstream deposition of sediment affected by the turbulent structure of the gravity current?

1.3 Thesis structure

This report is organized in seven chapters and four appendices. Even if the main chapters are written as scientific journal papers, the document is organized to avoid repetitions of content between sections of different chapters. The document structure is illustrated in Figure 1.3 and detailed in the following.

In this **Chapter 1**, the framework of this research is presented. An introduction and the main motivation have been presented. The gaps of knowledge in this topic are put in evidence by the research questions that are addressed by this project.

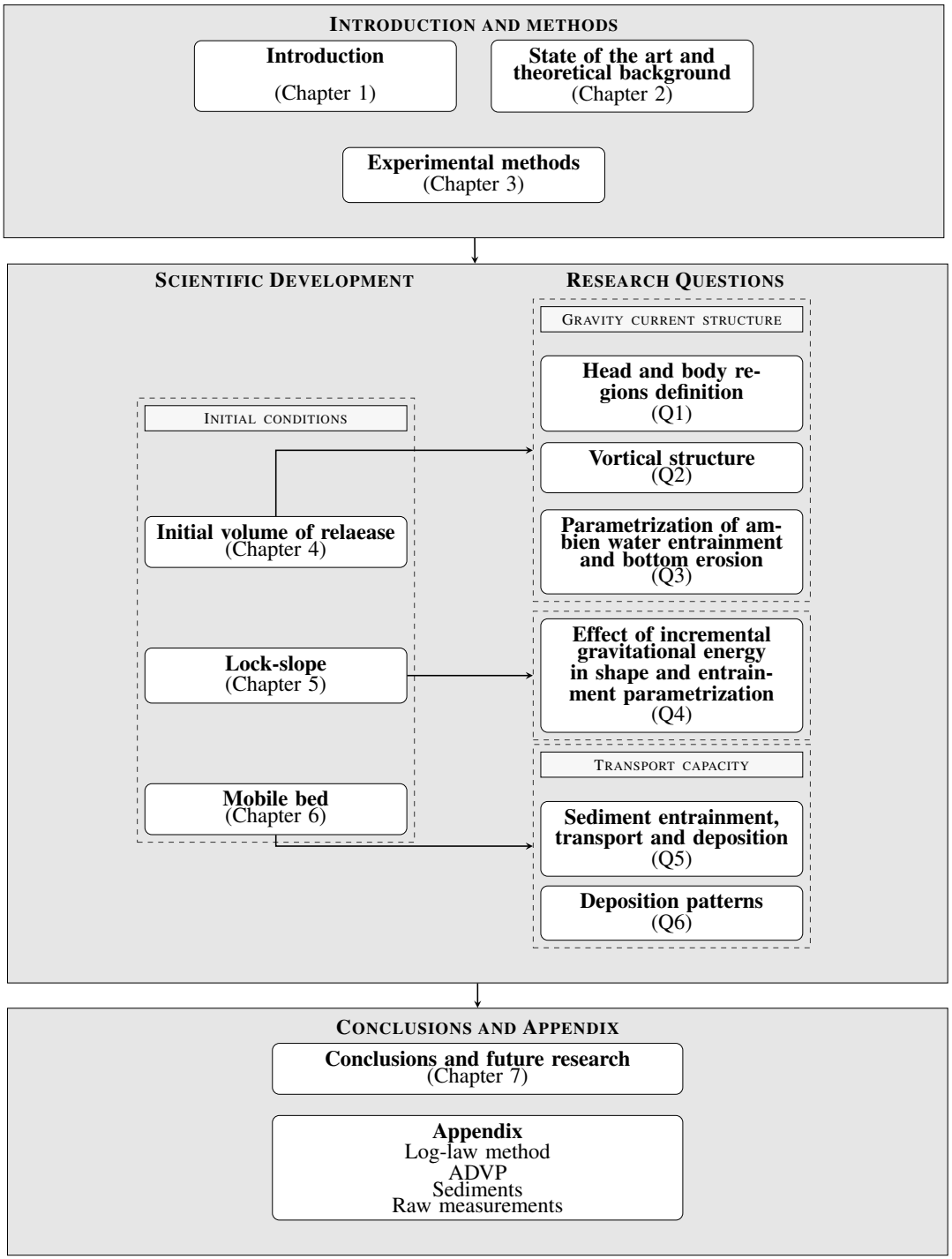

Figure 1.3: Schema of the document structure and research methodology. At the core, the subdivision of chapters by set-up configuration is highlighted using keywords of the initial conditions tested. Chapters are linked to the research questions addressed which are focussing on two topics namely the structure of the gravity current and its transport capacity.

Chapter 2 is dedicated to the state-of-the art, in which the main contributions to date on the topic are presented. This literature review focuses on the gravity currents forming by lock-exchange technique, with variable bed slope, and on mobile bed since those are the parameters tested in this research. Theoretical background and the scaling issues are also discussed.

Chapter 3 is devoted to the experimental details: the laboratory set-up, measuring equipment and experimental procedure are presented for the three groups of measurements performed. The experimental variables and parameters are summarized in this chapter.

In **Chapter 4**, the tests performed under variable lock-lengths and the corresponding results are presented. A criterion to determine the shape of the gravity current is established and the complex internal vortical structure characterized. A new method based on the shear stress time evolution that account for the entrainment capacity at the two, upper and bottom, boundaries of the gravity currents is presented.

Chapter 5 presents the group of tests performed with an inclined lock. The shape of the current is altered due to the enhanced entrainment of ambient water and mainly the body of the current results affected. How the increment of gravitational energy, due to the introduction of the slope, influences the hydrodynamics of the gravity currents, and consequently its potential transport capacity, is discussed.

In **Chapter 6**, tests of gravity currents flowing on a mobile bed are discussed and analysed. The mechanisms governing sediment entrainment, transport and deposition are described. The feedback between the hydrodynamics of a gravity current and the geomorphic changes of a mobile bed is investigated as well as the effects on the gravity currents induced by the incorporation of entrained sediment that may change its momentum by introducing extra internal stresses. The deposition patterns induced by the turbulent structure of the currents is examined and related to the flow initial buoyancy and to the size of the mobile bed sediment.

Finally, in **Chapter 7**, the main conclusions are drawn with suggestions and recommendations for future research.

Four appendices are included at the end of the report. The first, **Appendix A**, presents the logarithmic velocity profile method for shear velocity estimations computed at the bottom and upper boundaries of the currents. The second, **Appendix B**, presents the details of the Acoustic Doppler Velocity Profiler, the main instrument of measurements. The operational functioning, the improved geometric configuration and the set of equations solved for the velocity components, that are implemented on the Matlab code here created to read the Doppler frequencies, are reported. The third, **Appendix C**, presents the characteristics of the sediments used in the third group of tests (Chapter 6). Finally in **Appendix D** the instantaneous streamwise and vertical velocity time evolution at selected heights along the vertical are reported for tests presented in Chapter 6. The decomposition in mean and fluctuating components is also shown.

1.4 Context and framework of the research

The effects of floods, storm surges and other inundation hazards are greatly amplified by undesired morphological changes in rivers, estuaries and coastal areas. Also, morphological changes in reservoirs and in the vicinity of man-made structures, inland and offshore, may hinder their functions, disrupt water supply and energy production and considerably increase the risk of failure of structures. Substantial economic losses, human fatalities, disruption of the social fabric and destruction of ecosystems may thus occur as a result of unmitigated morphological changes. To understand and predict the evolution of river, estuarine or coastal morphology, a deep knowledge of sediment transport mechanisms and its relation with flow hydrodynamics is of paramount importance. Furthermore, the frequency and magnitude of disasters associated or caused by excessive morphological dynamism are likely to increase due to climate changes. Hence, the research investment is on fundamental sediment transport processes. Phenomenological insights must then be included into morphology predicting tools that, then, can be applied in the engineering realm by well-trained practitioners (http://www.seditrans.civil.upatras.gr).

Thus, it is very important to advance knowledge and train future engineers in this field. This research is part of the European project **SEDITRANS** (funded by Marie Curie Actions FP7-PEOPLE-2013-ITN-607394, Multi partner - Initial Training Networks), a network formed to train researchers in all application areas of sediment transport. The network consists of six academic (University of Patras, Université Catholique de Louvain, University of Cyprus, Università degli Studi di Trieste, Instituto Superiore Tecnico and Ecole Polytechnique Fédérale de Lausanne) and four industrial partners (Fugro GeoConsulting, Idrostudi Srl, Stucky Ltd and Laboratório Nacional de Engenharia Civil de Lisboa) and provides an elaborate and interdisciplinary training-through-research program to 12 early stage and 4 experienced researchers. It includes a comprehensive academic program, secondment at industrial partners, workshops, winter and summer schools, thematic conferences, production of guidelines and complementary activities.

The role of this research project, within the framework of SEDITRANS, is to bring knowledge on sediment transport caused by gravity currents. These flows, characterized by complex hydrodynamics, are capable of transporting high amount of sediments and are authors of great geomorphic changes. Once their turbulent structure, that is consequence of the release conditions, is described, the coupling between the evolution of the gravity current and that of the underlying substrate is explored.

In the frame of this project, a collaboration with a PhD from Università degli Studi di Trieste took place in order to reproduce numerically, through a 3D LES model (Roman et al., 2010), the experimental tests of the third group presented in this research (details in Section 3.2.2). The results of this collaboration are reported in a peer-reviewed journal (Kyrousi et al., 2017b) and in some conference contributions (Kyrousi et al. (2017c) and Kyrousi et al. (2017a)). Another collaboration was established with the company Stucky SA (Renens, Switzerland) with the

aim of testing the software BASEMENT (Vetsch et al., 2015) for a comparative analysis of 2D shallow water softwares. In this benchmark, selected softwares, including commercial and academic ones, were run by a group of researchers from SEDITRANS project in order to perform simulations of several test cases focusing on sediment transport modelling.

2 State of the art and theoretical background

2.1 The governing parameters and equations

Gravity currents are created when two fluids of different densities get into contact under the action of the gravitational force. Hydrostatic pressure conditions are present in the two contacting fluids of different densities: $\partial p/\partial z = -\rho_i g$ (with g the gravitational acceleration acting in the vertical direction, $-z$, and ρ the density of the fluids with the index i that can take values $i = a,\ c$, where a stands for ambient fluid and c for gravity current). When there is a difference in ρ between the fluids, it produces a pressure excess in the denser fluid, $\propto (\rho_c - \rho_a)gh$. At the interface, variations in the height of the current h along the streamwise-direction (x) give rise to pressure differences in this direction so that the longitudinal pressure gradient in the current can be written as:

$$\frac{\partial p}{\partial x} \propto (\rho_c - \rho_a) g \frac{\partial h}{\partial x} \tag{2.1}$$

This is particularly important since it is linked to the main internal driving force of the current. The fluid is pushed into the streamwise-direction by the so-called pressure (buoyancy) force and this effect is independent of z. This behaviour of the pressure field supports the basic feature of the gravity current which is a dominant horizontal propagation accompanied by slow variations of thickness (Ungarish, 2012).

The typical velocity of propagation of the gravity current could be estimated in the lock-exchange configuration from the energy conversion as it was formulated by Von Kármán (1940) and explained in the following. The dense fluid is stored in a lock of height h_0 and so the mean potential energy of a particle in the lock is $(1/2)g'h_0$ per unit mass. Here, the gravity effect associated with the density difference is referred to as the reduced gravity:

$$g' = g\left(\frac{\rho_c - \rho_a}{\rho_a}\right) = g\left(\frac{\Delta\rho}{\rho_a}\right) \tag{2.2}$$

Converting the potential energy into kinetic energy $(1/2)u_0^2$, the velocity scale is defined as:

$$u_0 = (g'h_0)^{1/2} \tag{2.3}$$

that is the initial buoyancy velocity by considering negligible the viscous friction.

The governing equations for conservative gravity currents can be derived directly from the basic principles of mass and momentum conservation of the current presented below in tensorial notation, where i and j take values 1, 2 and 3, corresponding to the directions x, y and z, respectively, leading to $(x_1; x_2; x_3) \equiv (x; y; z)$ and $(u_1; u_2; u_3) \equiv (u; v; w)$:

$$\frac{\partial \rho_c}{\partial t} + \frac{\partial \rho_c u_i}{\partial x_i} = 0 \tag{2.4}$$

$$\frac{\partial \rho_c u_i}{\partial t} + \frac{\partial \rho_c u_i u_j}{\partial x_j} = -\frac{\partial p}{\partial x_i} + \frac{\partial}{\partial x_i}\left(\mu_c \frac{\partial u_i}{\partial x_j}\right) + \rho_c g_i \tag{2.5}$$

where p is the pressure, μ_c the dynamic viscosity of the saline mixture and g_i the component of acceleration due to gravity in the i^{th} direction.

Assuming that the density differences between current and ambient fluid are relatively small $(\rho_c - \rho_a)/\rho_a << 0.1$ (Graf et al., 1998), the Boussinesq approximation can be applied and the density differences can be neglected in the inertia terms, appearing only in the term associated with gravity since this is the flow driving force.

The instantaneous quantities in the equations above can be separated into their mean and fluctuating components by application of the Reynolds decomposition:

$$a(x,y,z) = \overline{a}(x,y,z) + a'(x,y,z) \tag{2.6}$$

where a is a certain quantity whose $\overline{a}(x,y,z)$ represents its time averaged and $a'(x,y,z)$ is the correspondent turbulent fluctuation, being $\overline{a'} = 0$. The Reynolds decomposition is applied to velocity, $u_i = \overline{u_i} + u_i'$, and pressure, $p_i = \overline{p_i} + p_i'$, terms in equations 2.4 and 2.5. Time-averaging over a time-period small enough that the unsteady character of the flow is still described (Baas et al., 2005) (see Appendix B), the mean conservation equations for mass and momentum are obtained:

$$\frac{\partial \overline{u_i}}{\partial x_i} = 0 \tag{2.7}$$

$$\frac{\partial \overline{u_i}}{\partial t} + \frac{\partial \overline{u_i u_j}}{\partial x_j} = -\frac{1}{\rho_a}\frac{\partial \overline{p}}{\partial x_i} + \frac{\partial}{\partial x_i}\left(\nu \frac{\partial \overline{u_i}}{\partial x_j} - \overline{u_i' u_j'}\right) + \frac{\rho_c}{\rho_a} g_i \tag{2.8}$$

Equation 2.7 is the continuity equation for an incompressible fluid and states that the divergence of the velocity field is zero. In Equation 2.8, terms on left side represent the rate of change of momentum per unit volume of the mixture, and the first and second terms are the local and advective flow accelerations, respectively. On the right side are the forces responsible for fluid acceleration: the first two terms correspond to the contact forces due to local pressure and viscosity, the last term representing the forces of mass, induced by the action of gravity. By time-averaging the Reynolds decomposed Navier-Stokes equations, a new term appears in Equation 2.8: the Reynolds stresses $-\rho_a \overline{u_i' u_j'}$, which represents the transport of fluctuating momentum by the velocity fluctuations in the mean flow.

The nondimensionalization of the governing equations gives rise to a dimensionless parameter, the Reynolds number, that takes into account if the flow is inertial (inviscid) or viscous and it

is given by:

$$Re = \frac{u_0 h_0}{\nu} = (g' h_0)^{1/2} \frac{h_0}{\nu} \tag{2.9}$$

where ν is the kinematic viscosity coefficient.

2.2 The structure of a gravity current

Gravity currents' shape is widely recognised to be composed of a highly turbulent frontal region, the head, and a shallower following flow, the tail (e.g. Hacker et al. (1996)). *Frontogenesis* is the name of the process that leads to the development of a region of strong density gradient which is called front (Simpson and Linden, 1989). This is effectively a discontinuity in which the isopycnals, the lines connecting points of equal density, become squeezed together at the location of the change in density gradient, as described by Hacker and Linden (2002). It is in this region where the main transfer of momentum (between the current and the ambient fluid) takes place. The furthermost point of the current, is known as the nose and is elevated from the bottom (Hacker and Linden, 2002). The current head is characterized by a three-dimensional unsteady flow, being related to two dominant modes of instability: Kelvin-Helmholtz billows and lobe-and-cleft structures. The first are mainly due to the shear at the upper and rear part of the elevated head (Simpson, 1972). The second originate close to the bed, in correspondence with the advancing front which is subjected to no-slip condition at the surface and result in a complex three-dimensional structure. They have been interpreted as the consequence of the gravitational instability of the less dense fluid over-run by the gravity current head (Simpson and Britter, 1979).

A quasi-steady region, called body, can form between head and tail, for a sufficient volume of heavy fluid released. Considering this steady part of a gravity current, a general shape of the mean velocity profile is identified that is similar to the case of a turbulent plane wall jet (Kneller and Buckee, 2000). It is composed by an inner and an outer region separated by the velocity maximum $u = U_{max}$, that is situated at a height, h_{max}. The height of the velocity maximum is controlled by the ratio of the drag forces at the upper and lower boundaries (Kneller and Buckee, 2000) and it was experimentally found to occur at about 0.2 of the height of the current (Altinakar et al., 1996). For a smooth boundary , the flow column can be considered as composed by two overlapping regions (Turner (1973b) and Dey (2014)): (1) the inner (wall) region for $z < h_{max}$, here turbulence is created by the bottom shear where sediment entrainment and detrainment take place; (2) the outer region, $z > h_{max}$, where turbulence is created in the mixing layer between the current and ambient fluid, and water entrainment takes place (Altinakar et al., 1996).

The surfaces of contact of a gravity current, at the bottom and at the interface with the ambient fluid, highly influence the dynamic of the current. High mixing occurs in these regions that enhance transport processes into the current. It is well known that the current exchanges

at the upper surface: mixing and entrainment, resulting from the competition of shear and buoyancy, take place. The competition between the stabilizing effect of buoyancy and the destabilizing shear is captured in a dimensionless parameter, the gradient Richardson number. The gradient Richardson number is used to determine the growth or damping of turbulence by stable vertical stratification, and is widely used in oceanic and atmospheric fluid dynamics. For a continuously stratified flow, a more global form of Ri which characterises the stability over the whole depth rather than at specific positions is the bulk Richardson number, Ri_b:

$$Ri_b = \frac{g' h cos\alpha}{u_c^2} \tag{2.10}$$

where g', h and u_c are the reduced gravity, vertical length scale and characteristic velocity of the current, respectively, and α is the slope angle and it is related to the densimetric Froude number by:

$$Fr_D = Ri_b^{-0.5} \tag{2.11}$$

For small Ri, shear dominates buoyancy, and the flow is unstable to Kelvin-Helmoltz instability. A critical value for the local Ri number has been found after theoretical studies of small disturbances on laminar stratified shearing flows conducted by Turner (1973b) corresponding to 0.25.

Due to the high exchange with the ambient water at the upper interface, this is not a sharp boundary. Instead a layer forms, which is hard to classify as gravity current or as counter-flow and whose parametrization is awaited. The contribution of Ellison and Turner (1959) laid the groundwork since they defined the height and velocity of the current considering the velocity distribution through the depth by using the integral scales:

$$Uh = \int_0^\infty u dz \tag{2.12a}$$

$$U^2 h = \int_0^\infty u^2 dz \tag{2.12b}$$

where h is the flow layer thickness and U the layer-averaged flow velocity. In these equations, the upper limit ∞ can be replaced by the distance from the bed to the zero velocity interface between the current and the ambient water above, as in Sequeiros et al. (2010a). The height h, as defined by Ellison and Turner (1959) (here identified by the notation $E\&T$), corresponds to the point where the density is the average of the ambient water and the initial density of the gravity current.

2.3 Lock-exchange gravity currents

Field studies have provided quantitative information on the nature of turbidity currents in lakes and reservoirs (Chikita (1990), Chikita et al. (1996), De Cesare et al. (1998), De Cesare

and Schleiss (1998)), but direct measurements are difficult to perform given the difficulties in handling the instrumentation: gravity currents have a destructive force that often makes it impossible to keep any type of installation (Parker et al., 1987). Thus, the utility of controlled laboratory experiments becomes evident (Parker et al., 1987). Advances in experimental technology have increased our understanding from broad description of the gravity current morphology to the inner structure of turbulence in these currents (Kneller and Buckee, 2000).

Gravity currents experiments have traditionally been simulated through the lock-exchange configuration that consists of the release of a volume of dense fluid into the lighter one, with the two fluids that are at the beginning at rest and separated by a gate. The earliest laboratory experiments of gravity currents made use of the lock release method and were carried out by Keulegan (1957). Performed over a range of initial densities, it was found that, after the gate was removed the currents propagate and evolve experiencing three distinct phases as firstly described by Huppert and Simpson (1980) and Simpson (1997). In the first stage, the *slumping phase*, the front advances at constant velocity and maintains nearly constant depth. In the second stage, the *similarity phase*, the current decelerates, as $t^{1/3}$ and decreases in depth. If the Reynolds number of the gravity current decreases sufficiently, a third phase occurs in which viscous forces are important (Hacker et al., 1996).

More recent simulations of gravity currents through lock-exchange technique were performed by Adduce et al. (2011), Nogueira et al. (2014a) and Theiler and Franca (2016), among many others. The aspect ratio of the denser volume is generally of the order of one ($R = h_0/L_i \approx O(1)$, h_0 the water column depth and L_i the lock length). Although partially idealized, such conditions provide a functional initial configuration for both theoretical considerations and numerical simulations (Hogg, 2006) and a closer affinity to real conditions. Continuous release of dense mixture is a second type of experiments that have been developed to produce currents that, by running much longer time periods than lock-exchange currents, develop a stationary body. This brings the advantage of using averaging procedures to characterize the current (Tokyay et al., 2011). Recently, in order to overcome the restrictions imposed by both set-up, gravity currents have been more frequently produced by lock-exchange with a lower aspect ratio: the initial volume of heavier fluid is comparable to the volume of the lighter one in the second part of the channel (Shin et al., 2004). This configuration allows the formation of an extended slumping phase in which the front velocity is almost constant. In these conditions, a quasi-steady regime is formed, similar to the steady state observed for constant feed gravity currents. Once the flow becomes steady, one can use methods developed to analyse constant-density channel flow for the study of the turbulence structure (Tokyay et al., 2011).

2.4 Gravity currents down a slope

A gravity current in nature generally occurs on variable topographies and most of the time travels along inclined slopes. Examples are powder snow avalanches, river discharge of

heavier fluid in a lake, leaks from liquefied natural gas reservoirs or gravity currents flowing on submarine continental shelf, which contribute highly to geomorphological evolution (Huppert, 2006). Ross et al. (2002) showed that only after some time the effect of the slope influences the gravity current and that initially the current behaves like a current on a horizontal surface. Beghin et al. (1981) were among the first to investigate the role of the slope on the physic of a gravity current. They proposed a bulk parametrization of the motion of the current head which propagates down the channel with a fixed amount of buoyancy. In their model, the head entrains ambient fluid and develops with a self-similar form throughout its motion. He showed that for very small slopes, typically less than 5°, a front velocity first goes through an acceleration phase followed by a deceleration phase. This is because of the fact that although the gravitational force increases as the slope becomes steeper there is also increased entrainment, both into the head itself and into the flow behind. This produces an increased retarding force on the current as momentum is imparted to the entrained fluid.

Some more recent contributions (Maxworthy and Nokes (2007), Maxworthy (2010)) propose a modified version of the theory of Beghin et al. (1981), accounting for buoyancy variation instead of the original assumption of constant buoyancy. They found that the head is continuously fed by the tail current from initiation until the maximum front velocity is reached. After the flux of negatively buoyant fluid into the current head ceased, it could be assumed that the current would then propagate as a current with constant buoyancy, i.e. with a velocity that eventually decreases. It has in fact been shown that, while with currents flowing along a horizontal boundary, the head is the controlling feature (Britter and Linden, 1980), down a slope, the body becomes more determinant in the gravity current evolution since it is up to 30-40% faster than the head velocity, in dependence on the slope, being able therefore to move faster material into the head.

Britter and Linden (1980) indicate that a critical angle exists over which buoyancy force is large enough to counteract the bottom friction and produce a steady flow, and this was found to be of around one degree. At this point two mechanisms affect the evolution of the current: the current entrains water from the upper surface due to the increment of friction and the head is fed by the rear steady current. Dai (2013) found that for high slopes angles, the edge of the head experiences a large upheaval and enrolment by ambient fluid towards the end of the deceleration phase, while for low slopes, the gravity current head maintains a more streamlined shape without violent mixing with ambient of the deceleration phase. He also confirmed that in the deceleration phase, the patterns for gravity currents on a very low slope (in his case of 2°) are similar to those on a horizontal bottom. In fact, the mixing at the front increases dramatically with slope and the effect of entrainment is seen in the measurements in the growth of the height of the head with distance down the slope (Britter and Linden, 1980). Ambient fluid entrainment implies that dilution of the fluid in the current is considerably greater when it flows down a gradient rather than along the flat and the head begins to lose buoyancy-containing fluid from its rear by the detachment of large, weakly vortical structures. At the same time it is still entraining fluid over the majority of its surface so that its mean density is reduced (Maxworthy, 2010). A good estimate of the amount of buoyant fluid that

enters the head during its motion becomes thus the crucial point (Maxworthy, 2010). Ellison and Turner (1959) showed that the rate of turbulent entrainment into a steady constant flow-rate inclined plume is a function of the overall Richardson number. An unsteady extension of this work is advisable. Moreover, the case of gravity currents driven by particles or moving on a mobile bed so that bottom entrainment can take place has also to be considered. In this case, particle deposition to and erosion from an underlying bed will also be available to change the head buoyancy (Rastello and Hopfinger, 2004). There will still be buoyancy gain by a following flow and loss by shedding into a wake, but this other contribution should be taken into account.

2.5 Gravity currents flowing on mobile bed

2.5.1 Sediment entrainment

In reality, most of the gravity currents not only happen on complex topographies but they also flow on varied bed compositions. When a gravity current is set into motion over an erodible bed, particles can be eroded, transported within the current and deposited much further downstream (Figure 2.1) and this process depends on the particle characteristics and on the flow hydrodynamics (García and Parker, 1993). Moreover entrained sediments can passively be advected by the current or they can have an influence on the current dynamics since they can fuel a self-accelerating current (Parker (1982), Parker et al. (1986), Eames et al. (2001)): entrainment of sediment can increases the buoyancy of the current itself (Akiyama and Stefan, 1985). These currents are called self-sustaining and they must comply with the auto-suspension criteria given by Bagnold (1962). This extra-buoyancy component has an influence in the current dynamic and it causes the current to increase its velocity. Conversely, settling of particles reduces current density and consequently the gravitational forces which maintain the flow, causing the current propagation velocity to decrease (Gladstone et al., 1998). Lower velocity means less turbulent energy and less sediment-carrying capacity, which induces additional settling and further reduces the gravitational driving force and velocity (García and Parker, 1993). This process of sediment loss and velocity reduction continues until motion stops. Clearly, erosion and deposition processes and consequent topography changes are dependent (Parker, 1982).

In the early studies of Ellison and Turner (1959), Parker et al. (1987), García and Parker (1993) sediment entrainment was investigated experimentally and expressed through empirical functions that depend (i) on the absolute density difference and on "some parameter in the form of a Richardson number specifying the stability of the layer" in presence of high enough Reynolds numbers (Ellison and Turner, 1959) or (ii) on particle characteristics through the particle Reynolds number (Re_{part}) and the settling velocity (v_s) and on the friction velocity (u_*). More recent contributions (Baas et al., 2005) discussed the coupling between the flow and sediment behaviour that is found to be controlled by the relative importance of gravitational settling and upward directed components of turbulent velocity. Salim et al. (2017) studied the

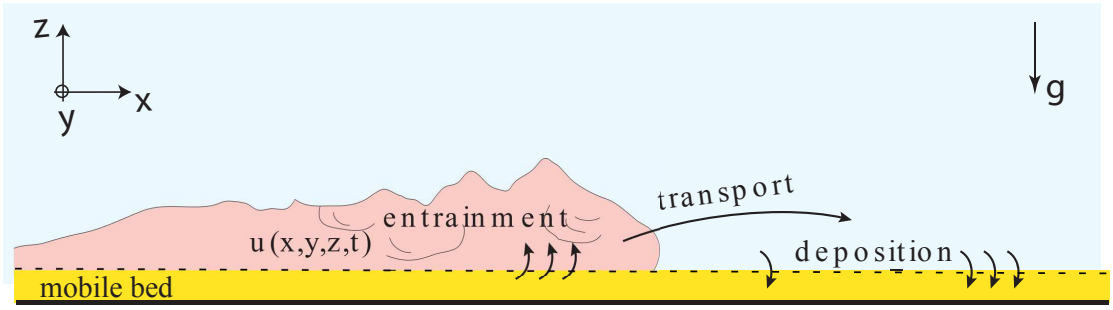

Figure 2.1: Sketch of a bottom gravity current flowing on an erodible bed. Entrainment of material from the bottom takes place which is transported within the gravity current and deposited downstream.

role of turbulent bursting events in sediment resuspension, claiming that turbulent effects have to be incorporated in order to improve the existing models based on the definition of threshold values (mean velocity or shear stress) for a better prediction of sediment transport.

The equilibrium of bed sediment depends on gravitational forces and interlocking between the bed particles, as resisting actions, and of forces that destabilize, such as (i) bed shear, (ii) impact (momentum transfer) and (iii) lift (buoyancy, vertical velocity-gradient pressure and upward turbulence) (Hickin, 1995). In a highly turbulent flow, as in the case of many gravity currents, the mean flow is often associated with velocity fluctuations that may play a critical role in dislodging grains from the bed (Hickin, 1995). But bed shear is accepted as the most important of the impelling forces, and since it is correlated with all the other involved forces, it provides a "surrogate measure" of them (Hickin, 1995). The magnitude of the shear stress at the lower boundary layer determines the sediment transport capacity of saline currents and whether erosion or deposition processes dominate the regime at the bottom boundary (Cossu and Wells, 2012).

2.5.2 Bed shear stress

Bed shear stress τ_b is not measured directly but inferred from estimates of the friction velocity u_*. Due to the quadratic relationship between τ_b and u_*, high-quality estimates of u_* are required in order to obtain reliable bed shear stress estimations (Bagherimiyab and Lemmin, 2013). A number of methods are available for estimating friction velocity: logarithmic mean velocity profile, turbulent kinetic energy (TKE) profile, wall similarity and spectral methods among others. Unfortunately, the near boundary region is the most difficult layer from which to obtain reliable velocity measurements since it is where the higher velocity gradients are located (Yang et al., 2012).

For a smooth boundary, the flow column can be considered as composed by two overlapping

regions: the inner and the outer layers (Dey (2014), among many others). The passage of the density current does not correspond to a steady process. However, it is possible to identify time intervals where the flow properties remain quasi invariant and consider a zone-averaged flow (Franca and Brocchini, 2015). Under the assumptions of flow gradually varied in the longitudinal direction, essentially two dimensional in vertical plane, and with high relative submersion, the streamwise velocity in the overlapping layer can be fitted to the logarithmic law of the wall (Ferreira et al., 2012). A friction velocity can so be calculated, and from this the bed shear stress. The von Kármán-Prandtl law of the wall is:

$$\frac{u(z)}{u_*} = \frac{1}{k} \ln \frac{z}{z_0} \tag{2.13}$$

where $u(z)$ is generally averaged over a sufficiently long time scale, u_* is the friction velocity, which is the velocity scale corresponding to the bed shear stress (Chassaing, 2010), k is the von Kármán constant, z is the vertical coordinate and z_0 is the zero-velocity level. If the flow boundary is assumed to be smooth, the classic value of the von Kármán constant of $k = 0.405$ is adopted but more discussions on the estimation of k can be found in Ferreira (2015).

The total bed shear stress related to the friction velocity u_* is written as:

$$\tau_b = \rho_c u_*^2 \tag{2.14}$$

being ρ_c the density of the current at a point close to the bed, here taken as the initial density of the gravity currents ρ_0.

2.6 Scaling

Geometric similarity, distorted scale modelling, unscaled analogues, Froude number similarities are among the options that we can find in literature (Kneller and Buckee, 2000). The range of slopes here proposed for the second group of tests (see Section 3.2.2) is of the order of magnitude of the canyons incised into continental margins (Sequeiros et al., 2010a) and they are thus in agreement with a geometric similarity. Because gravity effects are important in these types of flows, dynamic similarity is maintained by preserving the Froude number (Imran et al., 2017), which is the ratio of inertial to gravitational (buoyancy) forces acting on a fluid flow. Assuming the same viscosity at laboratory and field scale, i.e. that of water, it is not possible to satisfy Reynolds similarity and Froude similarity simultaneously thus Reynolds number is often relaxed. However, the range of Reynolds numbers for all flows considered here are high enough so that the flow can be considered fully turbulent and the assumption that the effects of viscosity are negligible is valid. To impose densimetric Froude similitude, the equality of the densimetric Froude number, Fr_D, in nature (prototype) and laboratory (model) is required:

$$\left(\frac{U}{\sqrt{g'H}}\right)_p = \left(\frac{U}{\sqrt{g'H}}\right)_m \tag{2.15}$$

where subscript 'p' and 'm' denote prototype and model, respectively. In a flow dominated by suspension, grain size should be scaled using fall velocity, v_s, rather than using the same scaling as for the main flow. Thus, (i) considering the relation of bed resistance valid in the case of open-channel flows, formulated in terms of a dimensionless Chezy number Cz:

$$Cz = \frac{U}{u_*} \tag{2.16}$$

where U is the depth-averaged flow velocity and u_* the bed shear velocity, and (ii) the threshold of suspension with the condition:

$$\frac{u_*}{v_s} = 1 \tag{2.17}$$

where v_s denotes the fall velocity of the sediment, the link between shear velocity and mean velocity is found. Combining (i) and (ii), being the same Cz number in laboratory and in the field and assuming a similar fractional density excess, the following relation for the velocity scale ratio λ_{v_s} is valid:

$$\lambda_{v_s} = \frac{v_{s_p}}{v_{s_m}} = \sqrt{\frac{H_p}{H_m}} = \frac{U_p}{U_m} \tag{2.18}$$

The flow thickness at field scale is expected to be at least two orders of magnitude larger than at laboratory scale, resulting in fall velocities at field scale being one order of magnitude larger than at laboratory scale (Sequeiros et al., 2010a). This way, sediment particle size D is not directly scaled down: to model a sand with a settling velocity of 5 cm/s, a silt should be used (Middleton, 1993). But such fine sediments may exhibit cohesion. We know that settling velocity in a fluid at rest mainly depends on size, density, shape and roundness of the particles (Dietrich, 1982). Under the assumption of spherical particles, it follows that the settling velocity is only function of the specific gravity of the sediment (i.e. the particle's density ρ_s) and its diameter (D) (Jiménez and Madsen, 2003). Therefore, to overcome the problems related to the use of very fine material, many authors have used sediment with a reduced density and greater size to keep the scale between the settling velocity of the prototype and model. This is the solution adopted in this research as well.

2.7 Conclusions influencing the present research project

2.7.1 Experimental set-up

Previous researches have demonstrated that lock-exchange technique is a convenient configuration for studying gravity currents through theoretical, numerical or experimental studies and it is the technique that is therefore chosen for the present research. The choice is supported by the fact that natural gravity currents are created by the movement of a given volume of denser fluid (snow avalanches, turbidity currents, oil leakages among many other examples),

as is the case for lock-exchange reproduced in laboratory. While designing the experimental set-up, a main concern was to allow the visualisation of the flow since video records were planned. Glass walls were therefore adopted for building the channel. The reflexion of the gravity current at the final section of the channel is usually a limitation for having longer records of the current body and this problem is here solved by placing a dumping system which is a final big tank that allows the currents to plunge and dissolve in it (as presented in the following Chapter 3).

2.7.2 Initial conditions

Head and body of the current are known to have different hydrodynamics and consequently different roles in sediment entrainment and transport of mass and momentum. The influence of the initial volume of release in the development of these two regions has been systematically tested as was never attempted before. The outcome of these preliminary tests have confirmed the importance of the body in the mixing process and that an extended quasi-steady body region is suitable for analysing the interaction between the hydrodynamics of a gravity current and the geomorphic changes of a mobile bed, which is one of the main focusses of this research. Changing initial conditions produces variations in the structure of the gravity currents and affect therefore the inherent mixing processes of these highly turbulent flows. The variation in the evolution of the gravity currents produced by methodically varying initial density of the denser fluid, initial volume of dense release and inclination of the bottom is here investigated. The range of slopes tested was intended to explore the behaviour of the gravity current for the critical angle that has been identified by Britter and Linden (1980), which intervenes for relatively small bed inclinations. The bed slopes up to 5° received relatively little attention in previous studies of gravity current down an inclined. By testing the inclinations up to a limit case in which two mechanisms take place (the current entrains water from the upper surface due to the increment of friction and the head is fed by the rear steady current) the transition from a friction governed flow to a flow in which gravitational forces become more and more important is here investigated.

2.7.3 Sediment transport

Understanding the physical processes governing sediment entrainment, transport and deposition within a gravity current has significant implications in nature (sediments play an important role in the natural cycle of the aquatic environment or as a sink for substances or pollutants) and for engineering applications (e.g. reservoir sedimentation or stability of hydraulic structures among others) but have so far seldom been investigated. In order to study the coupling mechanism between the evolution of the gravity current and sediment transport, the lock-exchange technique, but with a volume of release that is comparable to the volume of ambient water in which the current forms, is therefore used, for the first time to the best of our knowledge. Moreover scaling effects are taken into account by carefully choosing the sediment used to reproduce the mobile bed.

3 Experimental methods

Chapter 3 is based on the scientific articles "Measurement of the deposition of fine sediments in a channel bed" by S. Chamoun, J. Zordan, G. De Cesare and M.J. Franca published in *Flow Measurement and Instrumentation* and "Image processing and laser measurements for the determination of gravity current erosion and deposition" by J. Zordan, C. Juez, A.J. Schleiss and M.J. Franca submitted to *Measurement Science and Technology*. The experimental work and the analysis presented hereafter is original and was performed by the author.

3.1 Introduction

Gravity current experiments have been performed in laboratory through many different techniques. The lock release was chosen in the present study. The experiments were performed in a set up specifically designed for the purpose at the Laboratoire de Constructions Hydrauliques (LCH) of EPFL.

Three configurations of the channel were tested: (1) horizontal bottom with variable lock-length; (2) lock with variable slope with constant water depth and consequently lock-volume reduction; (3) horizontal bottom with the longest lock-length and with mobile bed.

Five lock volumes are created by shortening the upstream wall of the channel so reducing the length (L_i) of the portion of the channel where the heavier fluid is situated.

The slope was created by introducing an inclined bottom in this upstream part of the channel (the lock). With this set-up, the head velocity is not affected since the relative submergence of the current, i.e. h_c/H, didn't vary (Altinakar et al., 1990): the flume depth at the section where measurements were collected is constant among tests.

The mobile bed consisted of a reach of 1 cm depth depression with a flat bed, where the erodible material is placed. The erodible bed is situated at a distance from the gate which ensures the complete formation of the gravity current flowing on it and to leave a downstream reach along the channel where deposition can take place.

3.2 Experimental set-up

3.2.1 Flume set-up and procedure of tests

The rectangular flume shown in Figure 3.1 is 7.5 m long and 0.275 m wide and it is divided into two sections of comparable volumes by a vertical sliding gate. The bed of the downstream part of the channel is horizontal and smooth. An upstream reach of the channel (the lock) serves as head tank for the dense mixture and is filled with salty water. The downstream reach is filled with fresh water reaching the same height as the upstream one and it is here where the current propagates and where the main measurements are made.

When the gate is removed through a system of pulleys, with a falling weight to produce an instantaneous full-depth release, differences in the hydrostatic pressure cause the denser fluid to flow downstream near the bed of the channel, while the lighter fluid flows in the opposite direction at the top, as described in Shin et al. (2004). The current is dissipated flowing down into a final large tank that was conceived to avoid the reflexion of the current at the final section. The final tank is 4 m long, 1.8 m wide, 1.5 m height (Figure 3.1). The channel in which the current is produced is connected to the tank at a height of 1 m from the floor in order to let the current plunge into the reservoir.

The experiments are prepared by firstly filling the channel with clear water reaching a water depth of h_0=0.2 m. The water depth is the same in the lock and in the main channel (Figure 3.1). In the lock an amount of sodium chloride is added, stirred and completely dissolved, in order to reach the predefined density of the fluid. A mechanical mixer positioned inside ensured that no density stratification occurred. Density and temperature were checked by means of a densimeter and a thermometer before each test. The two fluids (ambient water and the denser salty water) are initially at rest, then the gate is released and the current forms.

In Figure 3.2, the experimental installation with (a) the upstream tank, (b) the downstream reservoir, (c) the gate and (d) the Acoustic Doppler Velocity Profiler instrument for velocity measurements, is shown.

3.2.2 Experimental parameters

Three group of tests were conducted. Three buoyancy differences are tested in combination with:

- five lock-lengths;
- five slopes of the head tank;
- three grain sizes of the material composing the erodible bed.

First group

Five lock volumes are created by shortening the upstream wall of the channel so reducing the length (L_i) of the portion of the channel where the denser fluid is situated (see Chapter 4).

Second group

Five inclinations of the bottom of the lock are created by introducing a slope on the channel lock-reach. In this way, the volume of denser fluid is reduced. The slopes ranges from 0 to 16% (which correspond to an inclination of the lock-bed from 0° to 9.09°) and the volume-reduction corresponds to the ones tested in the first group of tests (see Chapter 5).

Third group

In the third configuration the channel presents at the bed, that is kept horizontal and smooth, an erodible bed reach, 2.5 m downstream from the gate. A depression on the flat bed of 1 cm of depth, is filled with Polyurethane artificial fine sediments. This erodible section has the same width as the channel and a longitudinal extent of 0.6 m. Three grain size distributions of the material composing the erodible bed were tested (see Chapter 6).

The main parameters are presented in the non-dimensional form by adopting the following dimensionally independent scales: h_b as the vertical length scale, here considered as one third of the total water depth h_0, which is 0.2 m, ($h_b = h_0/3$). The length scale is chosen since preliminary tests have revealed that the height of the body of the current is, on average, one

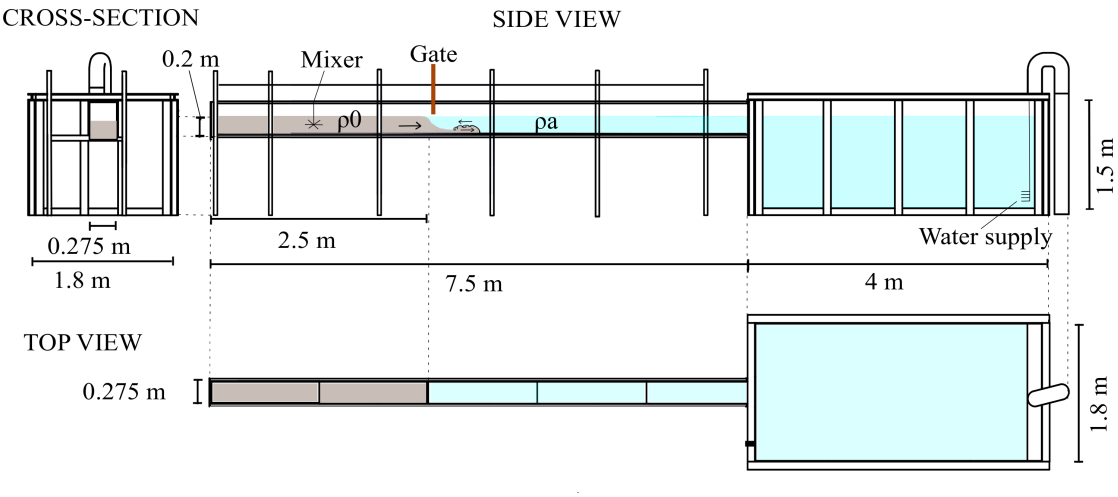

Figure 3.1: Side view, cross section and top view of the experimental set-up.

Figure 3.2: Experimental set-up at the Laboratoire de Constructions Hydrauliques (LCH) of EPFL with the upstream tank (a), the downstream reservoir (b), the gate (c) and the Acoustic Doppler Velocity Profiler (d) instrument for velocity measurements.

third of the total water column. The time scale is therefore defined as:

$$t^* = \frac{h_b}{u_b} \tag{3.1}$$

with u_b the buoyancy velocity which is the velocity scale and it is defined as:

$$u_b = \sqrt{g' h_b} \tag{3.2}$$

3.3 Measurements

3.3.1 Types of instrumentation

The measurements conducted are based on four different instruments: the Acoustic Doppler Velocity Profiler collects instantaneous 3D velocity measurements, a high speed camera takes video from the transparent side wall, a laser technique combined with photogrammetry are finally used to measure the sediment morphology of the bottom.

While for the first and second groups of tests the ADVP only was used, for the third group the whole set of instruments was synchronously operated. Figure 3.3 shows a general view of the complex of measurements collected at the passage of the gravity current during the third group.

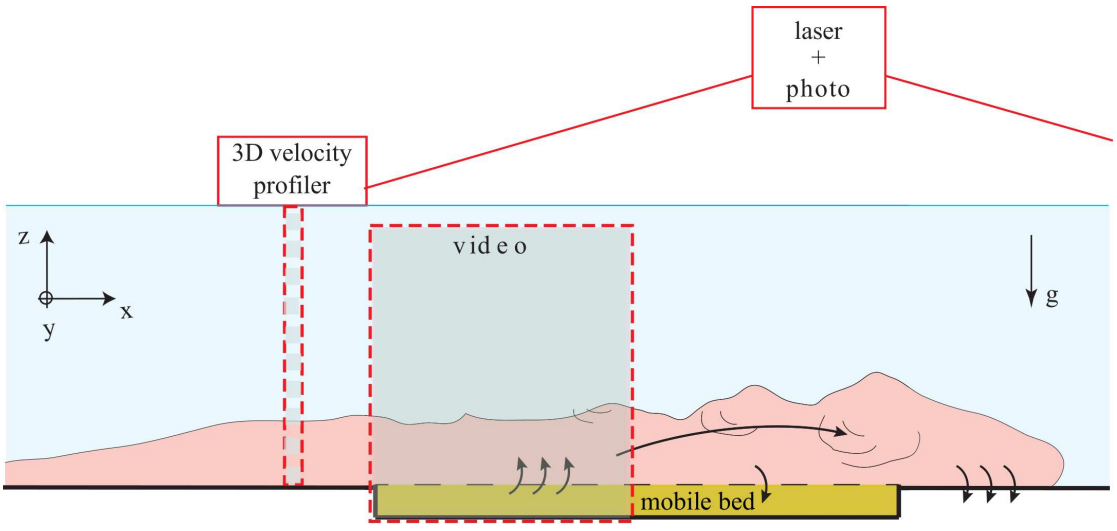

Figure 3.3: Sketch of a bottom gravity current and details of the instrumentation used: the 3D velocity profiler (ADVP) placed just upstream the mobile reach, the high speed camera takes video from the transparent side wall covering the zone in correspondence of the erodible bed, a laser technique combined with photogrammetry measure the sediment morphology of the bottom.

3.3.2 Acoustic Doppler Velocity Profiler

The 3D Acoustic Doppler Velocity Profiler (ADVP) (Lemmin and Rolland (1997), Hurther and Lemmin (2001), Franca and Lemmin (2006)) is a non-intrusive sonar instrument that measures the instantaneous velocity profiles using the Doppler effect without the need of calibration. It is placed 2.5 m downstream from the gate, immediately upstream from the mobile bed (see details in Section 6.2, Figure 6.1). This distance was large enough to assure the gravity current formation and also that its characteristics are not affected by the release conditions. It measures simultaneously 3D instantaneous velocity components during the passage of the density current, over an entire vertical profile, including the upper counter-flow. The minimum number of pulse-pairs is here fixed at 32 which corresponds to a frequency of acquisition of 31.25 Hz (Lemmin and Rolland, 1997). The instrument consists of a central emitter surrounded by four receivers (for details see Appendix B). The geometric configuration is the result of an optimization of the instrument that allows noise reduction by creating redundancy information for the velocity components by using four receivers (Blanckaert and Lemmin, 2006). Additionally, the signal despiking procedure proposed by Goring and Nikora (2002) was used, and results in a considerable reduction of the noise level. The instantaneous velocity components are measured in time along a vertical profile that is divided into volumes, called "gates", that are consecutively scattered by the sound waves (Hurther and Lemmin, 2000). Figure 3.4 displays a dataset of the instantaneous component of the streamwise velocity for one test (R1.fine, see Table 6.1 for test definition). On the x-axis of Figure 3.4 is the time and on the y-axis the gate numbers, numbered from the surface to the bottom of the flume. A total of 44 gates in the vertical are measured which means that the total fluid height of 200 mm is divided in gates of about 5 mm each.

The zero of the vertical coordinate system is fixed at the bed, with the axis directed towards the water surface, while the reference for time x-axis is at the moment when a first positive streamwise velocity is detected, i.e. when the ADVP detects the arrival of the front of the gravity current (see Figure 3.4).

By touching the water surface, the ADVP housing perturbs the flow in a region of less than 2 cm near the water surface (Blanckaert, 2010). This region is, for this reason, masked in the velocity field representation of the following chapters.

3.3.3 ADVP data post-processing

By means of the analysis of the power spectra of the raw data collected with the ADVP, noisy frequencies were mainly detected above 8 Hz (Figure 3.6). The instantaneous measurements were thus low-pass filtered with 8 Hz as cut-off frequency.

To determine the time-series of the mean velocities ($\overline{u}$, $\overline{w}$, respectively for streamwise and vertical directions), for the unsteady gravity current, the analysis proposed by Baas et al. (2005) (similar to a zone-average as defined in Franca and Brocchini (2015)) is here adopted. A

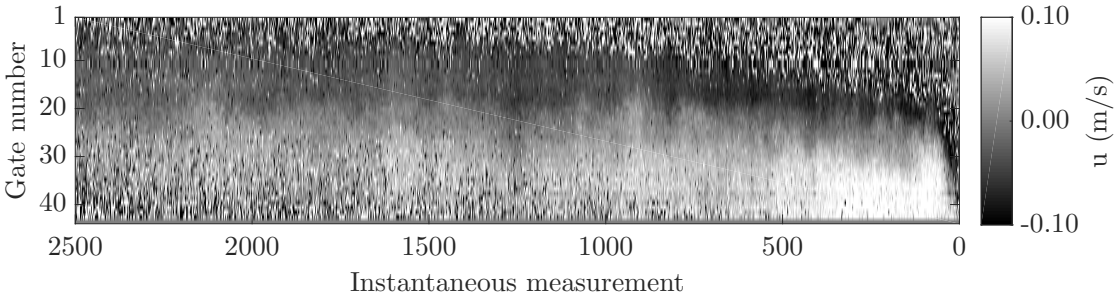

Figure 3.4: Instantaneous streamwise velocity for test R1.fine. The vertical is divided in 44 gates, of about 5 mm each. The magnitude of the velocity is indicated by the coloured bar.

time-window of 0.32 s is chosen to apply for a moving average since the analysis of the power spectra confirms that with this window the harmonics of all the meaningful frequencies are still recognisable while, increasing the time window, the harmonics of progressively smaller frequency gradually lose power and they become impossible to distinguish from white noise. This procedure is made to both streamwise and vertical components. This moving average defined the mean streamwise and vertical velocities $\overline{u}$ and $\overline{w}$ which, following the Reynolds decomposition, are related with the instantaneous velocities (u, w) and the turbulent fluctuations (u', w') as defined in Equation 2.6.

The vertical profiles of $\overline{u}$ are shown in Figure 3.5 for one exemplar test (R1.fine, see Table 6.1 for test definition) at several instants, in a composite image with on the back the time evolving mean streamwise velocity field.

The cleaning procedure of the signals and corresponding spectra is shown in Figure 3.6.

Because the turbulent motions associated with the eddies are approximately random, we can characterize them using statistical concepts. The scales of turbulence velocity are defined as the root-mean square (RMS) of the streamwise and of the vertical fluctuating components (second order moment of the velocity distribution) as defined by Kneller et al. (1997):

$$u'_{rms} = \left[\frac{1}{m} \sum_{i=1}^{m} (u_i - \overline{u})^2 \right]^{0.5} \tag{3.3}$$

$$w'_{rms} = \left[\frac{1}{m} \sum_{i=1}^{m} (w_i - \overline{w})^2 \right]^{0.5} \tag{3.4}$$

where m is the number of observations and i refers to the observation.

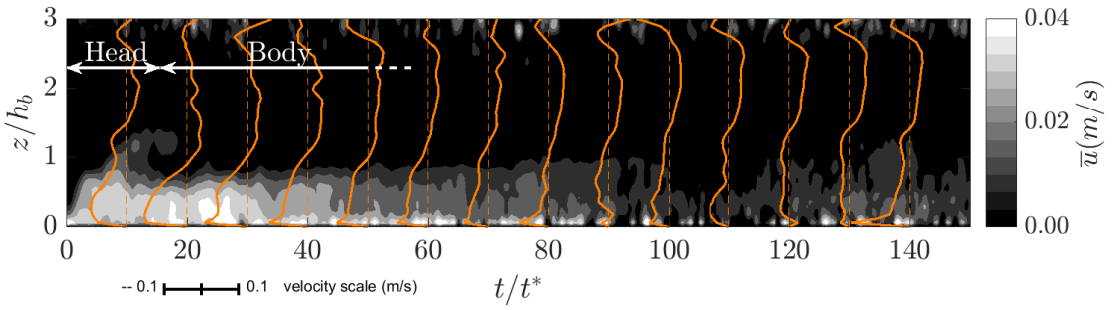

Figure 3.5: Composite representation of the vertical profiles of mean streamwise velocity (in orange) and instantaneous streamwise velocity map. The regions of the currents are also identified.

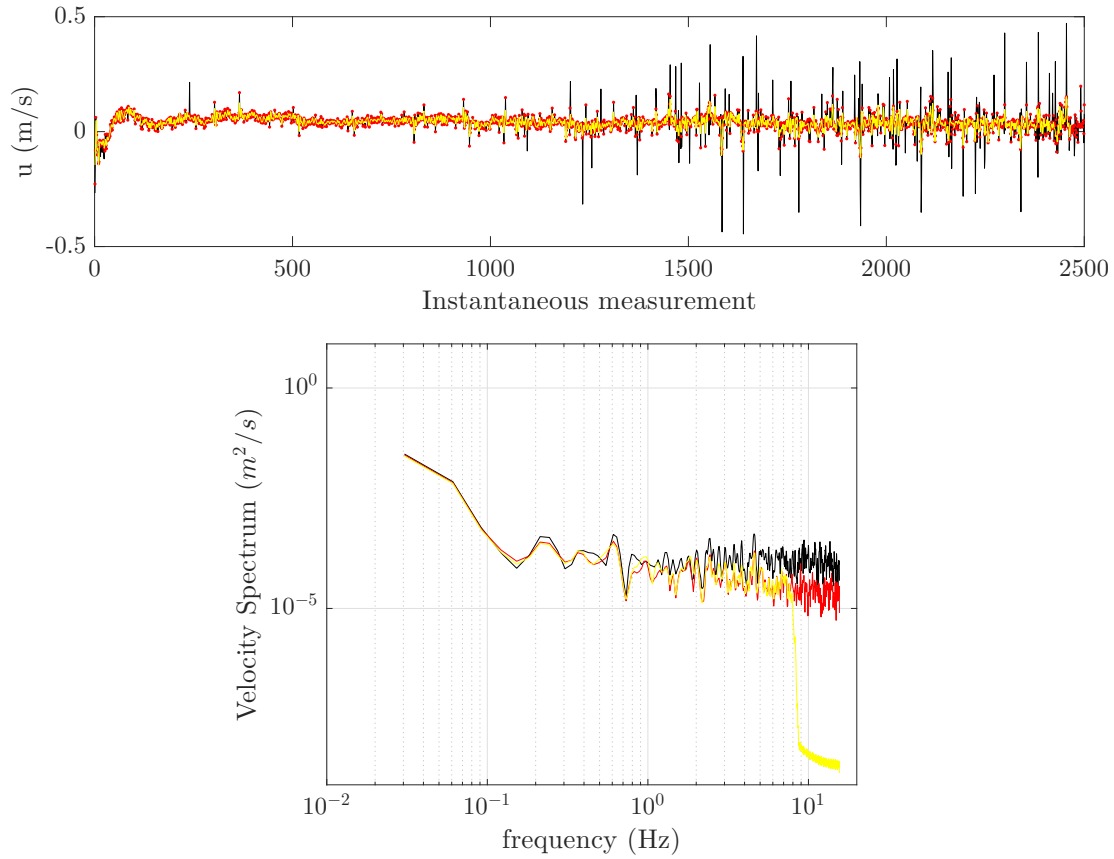

Figure 3.6: Raw velocity data (black) and despiked data (red) obtained with the procedure proposed by Goring and Nikora (2002). Then, through the analysis of the velocity spectra (figure at the bottom), the cut-off frequency of 8 Hz has been identified in order to low pass filter the noisy frequencies (yellow line).

3.3.4 Pulsed red laser diode

A Baumer OADM13 laser is used to measure the topography of the mobile bed reach and of the downstream channel bed, before and after the passage of the current. It is a photoelectric distance-measuring compact sensor composed of a laser emitter that produces a light source and a photodiode line working as receiver. The measuring range of this pulsed red laser diode is of 50-350 mm and it has an accuracy of 0.01-0.4 mm. It is typically used in production processes (e.g., for flaw detection in industrial application) but recently applied in a wider range of applications (Chamoun et al., 2016b).

In Figure 3.7 the dimensions and a sketch of the triangulation working principle, which allows to measure the distance from an object, are reported: the laser beam strikes an object and the receiver reads the angle of incidence of the backscattered light. The angle of incidence changes according to the distance (in Figure 3.7, two points placed at a distance A or A+B produce a backscatter light that has a difference of inclination α). The receiver converts the backscattered light into a current and an integrated microcontroller detects the position of this point. The controller calculates the angle from the light distribution on the photodiode line and then deduces the distance to the object (Baumer, 2015).

The measuring range can be adjusted by the user within the maximum measuring range of 50-350 mm (imposed by the factory setting). The analog output has its full span within this range that is also called "Teach-in" range. Changing the measuring range causes a variation in the resolution and a linearity error (deviation between calculated value and measured value due to technical reasons). In other words, the closer the furthest point of the measuring range is to the sensor, the better the resolution and the same goes for having a lower linearity error. The Teach-in feature is designed to choose a smaller range within the nominal measuring range for optimizing the resolution and linearity. Two positions must be taught: the first Teach-in position aligns with 0 V (or 4 mA), the second position aligns with 10 V (or 20 mA), therefore the current or voltage output adapts to the new range. A voltage converter translates the current into a voltage signal which is finally sent to the PC. The evolution of the signal in time is shown by a graphical interface which acquires, displays and stores the data.

The calibration equation needed in order to link the output voltage to the distance of the laser light source from the top of the sediment deposit and so to derive the topography of the bottom, is obtained in experimental operating conditions using gauges of different known thickness. The characteristic derivation of the calibration line of the laser is presented in (Chamoun et al., 2016b) and, in the operation conditions of this set-up, is given by:

$$e = -0.1746V + 7.2613 \tag{3.5}$$

where e (mm) is the thickness of the deposit at the bottom and V (Volts) the output of the laser. The values were highly correlated with $R^2 \approx 0.99$. Equation 3.5 is implemented in the software, and the output measurements are therefore directly provided as thickness of the deposits.

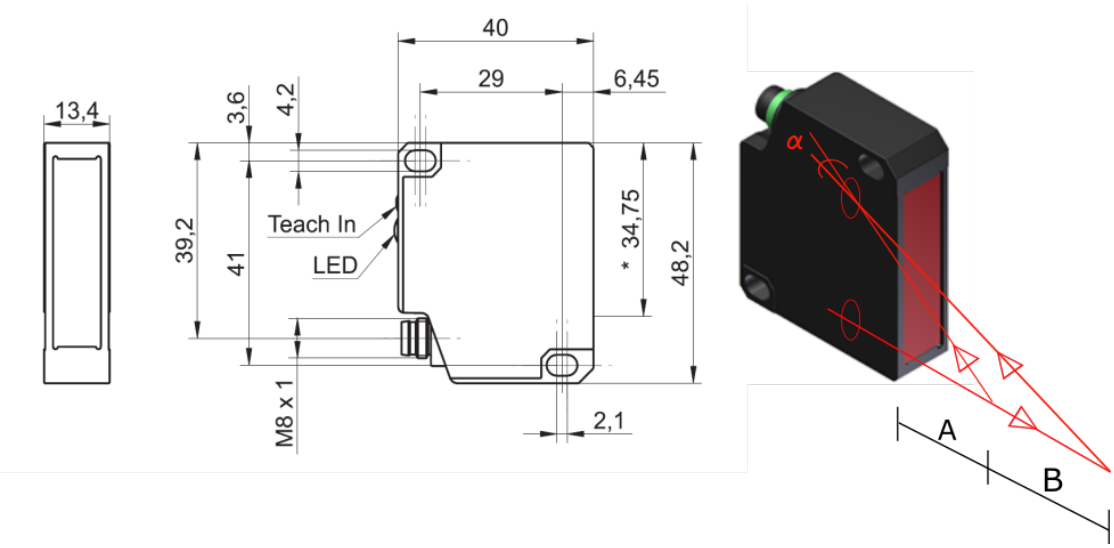

Figure 3.7: Laser Baumer OADM13 dimensions (Baumer, 2015) and sketch representing the triangulation principle of the laser beam.

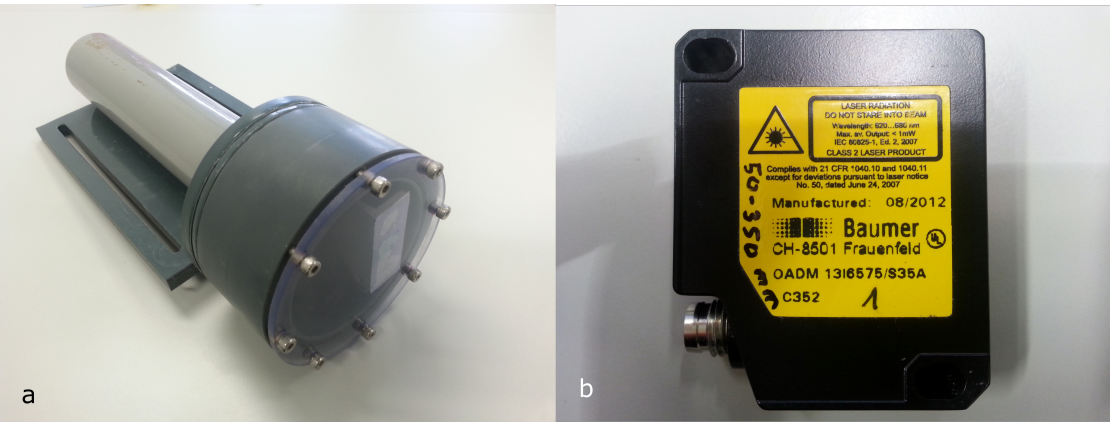

Figure 3.8: The laser waterproof box (a) and the laser Baumer OADM13 used for the tests (b).

The measurements were collected with the channel still filled with water to avoid flushing away the fine sediment while emptying it. Thus, for operation, the instrument is placed in a water-proof box (Figure 3.8), at an arbitrary height from the reference bottom (here 100 mm).

A sliding system allows the instrument to be pulled steadily letting the laser light cross the transparent bottom of the box to streak the bed of the channel along established paths. The structure is moved at a constant velocity and the instrument collects data at a fixed frequency of 20 Hz.

The laser recorded point measurements of distance to the first solid surface encountered. The instrument is placed at a known distance from the bottom so, whether a deposition layer is present, the information in distance can be converted, by difference, into thickness of deposit, by composing the surveys made after and before the reference condition.

The laser collects data on the mobile bed reach and for a length of 500 mm downstream, as shown in Figure 3.9:

- the laser is slid along eight longitudinal profiles ($Z_{BED,i}$) of the mobile bed reach (which total surface is A_{ER});
- the laser is slid over eight equally spaced cross-sections, from x=700 mm to x=1100 mm.

Figure 3.10 displays the result of the linear interpolation of the data collected with the laser. The passage through the original sampled points is forced for the interpolation. The current flowed from left to right.

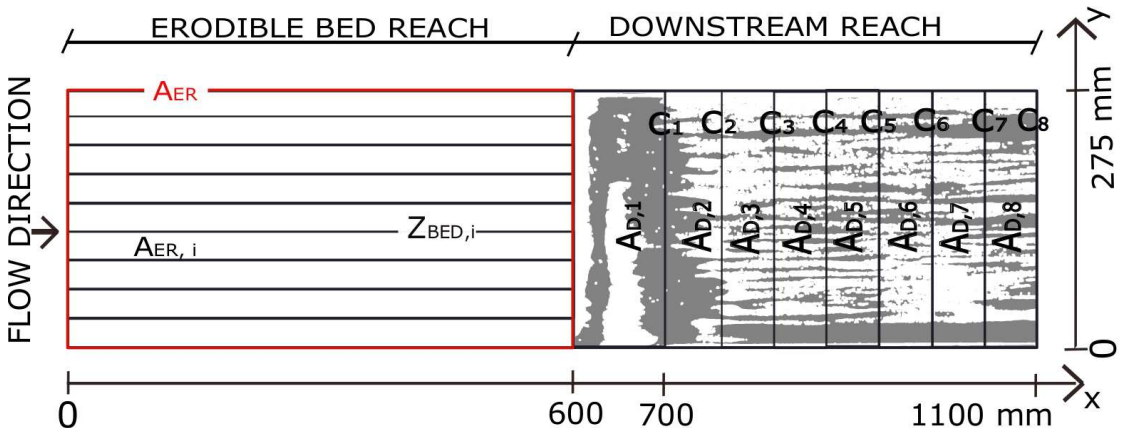

Figure 3.9: Sketch of the sections surveyed by the laser on the mobile bed reach and on the downstream reach of deposition. The mobile bed reach is subdivided in nine areas $A_{ER,i} = A_{ER}/(n+1)$, with A_{ER}=0.275 x 0.6 m^2 the total surface of the mobile bed and $n = 8$ the number of equidistant longitudinal sections recorded ($Z_{BED,i}$). The downstream zone of deposition is surveyed by 8 equidistant cross-sections (C_i) covering the bed surface from 100 mm after the mobile bed for a length of 400 mm. $A_{D,i}$ are the areas adjacent to the correspondent C_i which subdivide the downstream reach. The pictures are taken in order to cover the whole downstream reach.

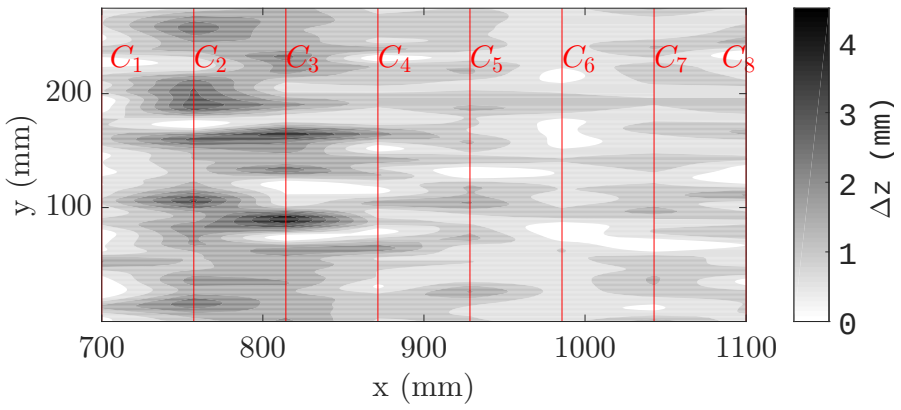

Figure 3.10: Result of the linear interpolation of the data collected with the laser with indication of the eight cross sections recorded.

3.3.5 High speed camera

The passage of the density current over the erodible bed was recorded laterally by a SMX-160 camera. The acquisition frequency was 25 Hz and the area of interest, with dimensions of 0.245 x 0.18 m^2 as indicated in Figure 3.11, had a spatial resolution of 0.5 mm/px. This resolution was bigger than the size of the sediments but accurate enough for distinguishing suspended sediments/gravity current and gravity current/ambient water interfaces. The captured frames were converted into gray scale matrices (256 gray levels) for their subsequent data treatment.

Two halogen spots of 1000 W were placed at the opposite side of the camera. Between the spots and the transparent wall of the channel a filter screen was inserted for achieving an homogeneous illuminated area. This system provided back lighting, which allows one to distinguish easily the movement of the current, and decreased the required exposure time, preventing blurred images. The reference time for the initialization of the experiments was chosen as the first moment where the current is entering in the visual field of the camera. In the collection of images taken during the experiments, four characteristic flow regions were identified: (i) a layer of clear water, (ii) a density current layer with the brine, (iii) a mixture layer with brine and few sediments and (iv) a dense layer of sediments. These flow regions were recognized by a semi-automatic threshold based procedure resulting in the definition of the relevant interfaces. The result of the data treatment is illustrated in Figure 3.11 where the original and the post-processed images are shown. The interface between the water and the density current was identified by the subtraction between the current frame and a frame without the current. The pixels corresponding to the sediments were isolated and the value annotated. A threshold value was identified and it was used for filtering the surface of the image covered by the cloud of sediment. Furthermore, the pixels whose value was above that threshold and below an average value of the pixels belonging to the density current layer they were labelled as a mixture layer. Thanks to the aforementioned protocol it was possible to measure the evolution of the current and of the cloud of suspended sediment within the interrogation window.

3.3.6 Reflex camera

The deposition patterns were captured through pictures that are taken from the top (Figure 3.9) in order to cover the whole width (y=0-275 mm) and a sufficient longitudinal reach (x=600-1100 mm). The camera used for this work, a Nikon D60, has a sensor resolution of 10.2 megapixels (sensor size is 23.6 mm x 15.8 mm), and offers ISO sensitivity ranging from 100 to 1600. It has a lens 18-55 mm, f/3.5-5.6.

The image processing comprised three steps: (1) image acquisition, (2) image analysis (treating the image and measuring objects) and (3) data processing (filtering the data) (Pennekamp and Schtickzelle, 2013). The most crucial step for automatic image analysis is to create a sharp contrast between the objects of interest (foreground) and their environment (background), so they can be accurately distinguished. This process is called segmentation (Gonzalez and

Woods, 2007) and is described later in this section. Ideally, the foreground will contain only the objects which have to be measured. However, some misidentified objects can also be comprised in the foreground, which need to be removed.

Images are usually represented as arrays, where the height and width in pixel give the row and column dimensions of the 2-D array (a matrix). The numerical values correspond to the intensity (i.e. a value between 0 and 255 for grayscale images). In fact, based on hardware considerations the number of intensity levels usually is an integer power of two, with the most common number being 8-bits. This is the case of the images used for this study which thus have a range of 2^8.

The choice of the material was aiming at improving the distinction between fore- and background: dark plastic was used for the bottom of the channel and white material for the sediment. Illumination was optimized to provide a homogeneous background and strong contrast. A lighting system permits a homogeneous repartition of the luminosity to distinguish the target objects independently of their position in the recorded frame. Illumination intensity needs to be high enough to allow for short exposure time and hence avoid blurring images (Pennekamp and Schtickzelle, 2013).

Images from the top of the deposition reach were taken from above the water surface. The recorded area was (500x275) mm with a resolution of (1818x1000) pixels. Images were converted from a truecolor image, RGB, to a grayscale image. Subsequently, a histogram equalization was used for enhancing the appearance of images. In order to produce a more uniformly distributed histogram, the gray levels need to be "stretched out" to produce an image that becomes much clearer (Maini and Aggarwal, 2010). For an 8-bit grayscale image there are 256 different possible intensities, and so the histogram graphically displays 256 numbers showing the distribution of pixels amongst those grayscale values. An example in Figure 3.12 shows the histograms for one test of raw image and of the image after histogram equalization. In Figure 3.13 the image treatment procedure is presented: from the equalized image, segmentation is performed and then it is converted into a binary image. The description of the procedure is also reported in Figure 3.13.

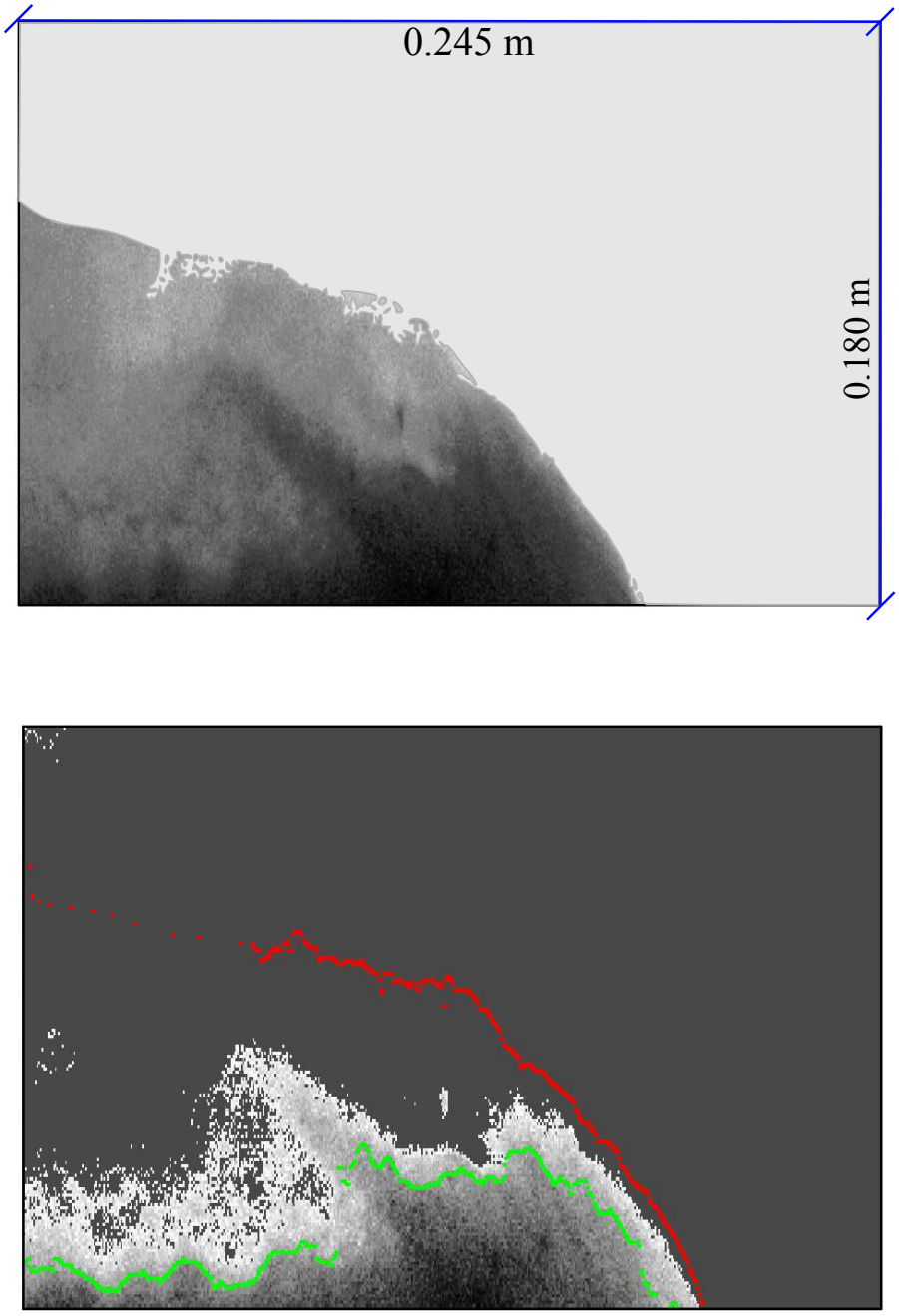

Figure 3.11: Detection of relevant flow interfaces. Original image (top) and post-processed image (bottom) with the interfaces between the clear water and the current (red line) and the current and the cloud of suspended sediments (green line).

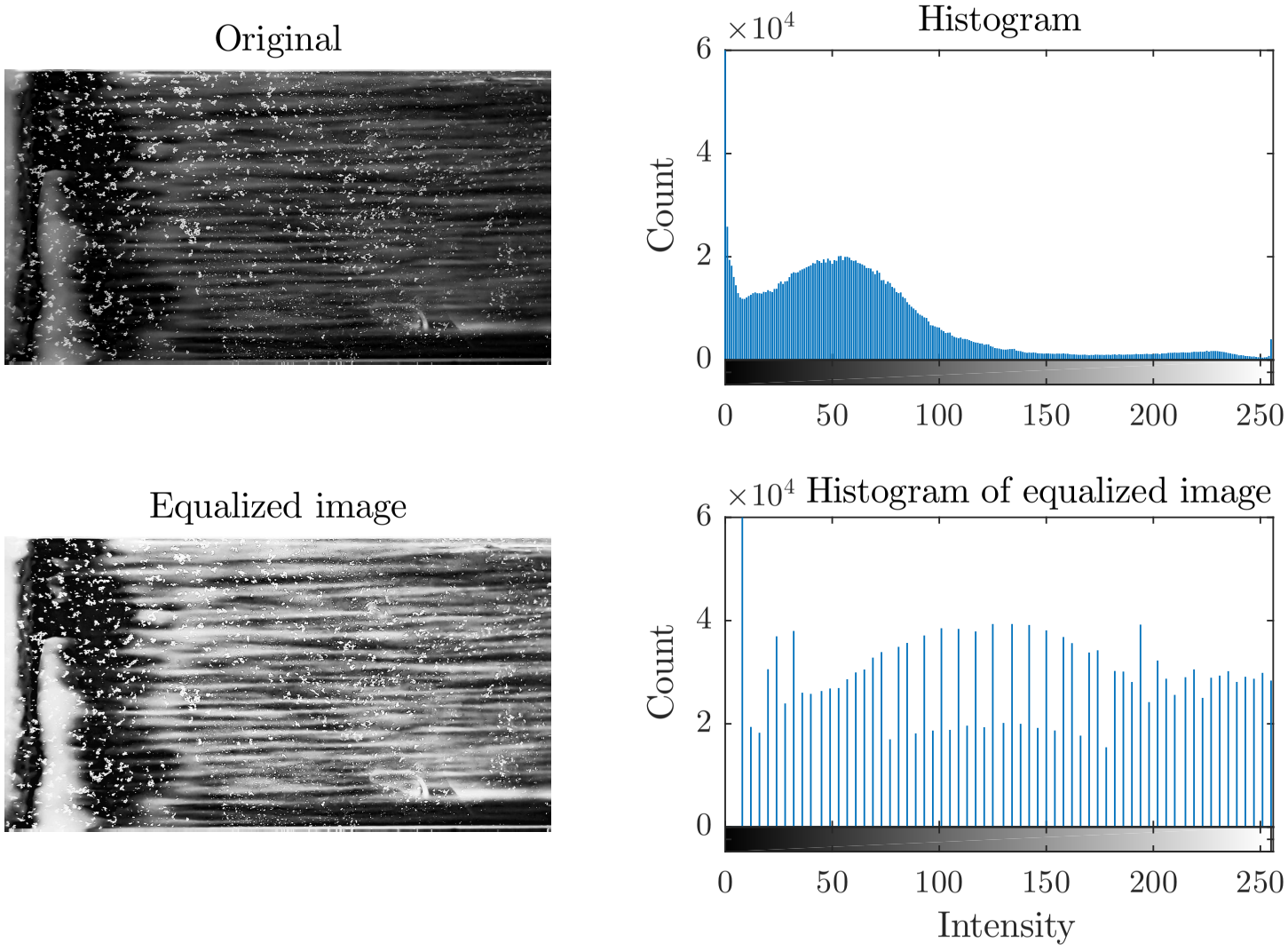

Figure 3.12: The original image and its histogram, and the respective equalized versions.

a) Identification of objects having a radius less than a certain amount of pixels. This allows to distinguish the pixels representing the dust floating on the water surface, in the fore-ground.

b) Separation of the segment previously identified by subtracting this from the equalized image.

c) Conversion of the image into a binary image (BW). The output image BW replaces all pixels in the input image with luminance greater than a certain level with the value 1 (white) and replaces all other pixels with the value 0 (black).

d) The final binary image is obtained by further removing all connected components (objects) that have fewer than a certain amount of pixels (here 50). This operation is known as an area opening and enhances the morphological noise removal.

Figure 3.13: Images treatment for test R1.fine step by step: (a) equalized image; (b) identification of rounded objects that is the dust floating on the water surface; (c) subtraction of the segment previously identified from the equalized image; (d) conversion of the image into a binary image (BW) by further removing all connected components with less than 50 pixels.

4 Horizontal and vertical structure of gravity currents produced by varying initial volume of release

Chapter 4 is based on the scientific articles "Structure of dense release produced by varying initial conditions" by J. Zordan, A.J. Schleiss and M.J. Franca under revision in Environmental Fluid Mechanics and "Influence of the initial volume of lock exchange gravity currents on sediment entrainment capacity" by J. Zordan published in Book of abstracts of IAHR 2017 conference, Kuala-Lumpur, Malaysia. The experimental work and the analysis presented hereafter is original and was performed by the author.

4.1 Introduction

Gravity currents are originated by the release of a certain amount of heavy fluid into another one of different density. Lock-exchange technique has been adopted by many authors (see Chapter 2.3) to reproduce these phenomena in laboratory. This has many advantages since it provides a functional initial configuration for both theoretical considerations and numerical simulations and moreover it recreates many gravity currents as they are generated in reality. Gravity currents at geophysical scale are in fact typically initiated by a given volume of dense fluid. Figure 1.1 showed some examples. Turbidity currents in ocean basins are often caused by slumps of sediment from the upper continental slopes (Heezen et al. (1954), Piper et al. (1985), Hallworth et al. (1993)). Avalanches of airborne snow are originated due to the detachment of a mass of snow from the main compacted snowpack (Bates et al., 2014). Considering extreme flooding storms in wetlands, these flows carry particles into suspension and a gravity current develops. Different flooding event intensities can be reproduced in laboratory by different volumes of dense mixture by changing the lock-length of the channel (Serra et al., 2017). Man-made gravity currents such as oil slicks depends on the amount of contaminant dispersed. In industry, examples are numerous as well: sheet glass production consists of a certain supply of molten glass across a horizontal surface (Huppert, 2006).

When the current forms, a well defined shape is recognised: a highly turbulent frontal region, the head, and a shallower following flow, the tail (Hacker et al., 1996). A quasi-steady region called body can form between head and tail and its extent vary in relation to the initial conditions e.g. the amount of heavy fluid released. A sketch of a gravity current is shown in Figure 4.1 where the characteristic variables are reported. Once a criterion for the identification of the lengths of head (L_h) and body (L_b) is established, their characteristic heights can be measured as well (δ_h and δ_b).

In terms of dynamic properties of the flow, gravity flows differ significantly from open-channel flows (e.g. rivers) regarding their velocity profile (Manica (2012) and many prior references). In the case of gravity flows, the shear at the upper interface (τ_m) has a main role and causes the creation of a *mixing zone* characterized by an high exchange between gravity current and ambient water. At the bottom, as a result of the no-slip condition, the resistance with the surface creates high shear (τ_b) and a *inner layer* with a higher density is formed. The vertical extent of these two layers are respectively indicated as h_m and h_i in Figure 4.1.

The objective is therefore to determine the shape of the gravity current produced by lock exchange, to establish a universal rule to allow the distinction of head, tail and the possible body. These regions have different dynamics and extent that vary in relation with the condition of release. These latter are parametrized by the length of the lock, i.e the initial volume of dense fluid released, and the initial buoyancy of the mixture in the lock. Secondly, the relative importance of the boundary layers, which are the upper mixing zone between gravity current and ambient fluid and the inner layer at the bottom, is analysed and determined.

The first challenge consists in identifying the zones composing the gravity current which are

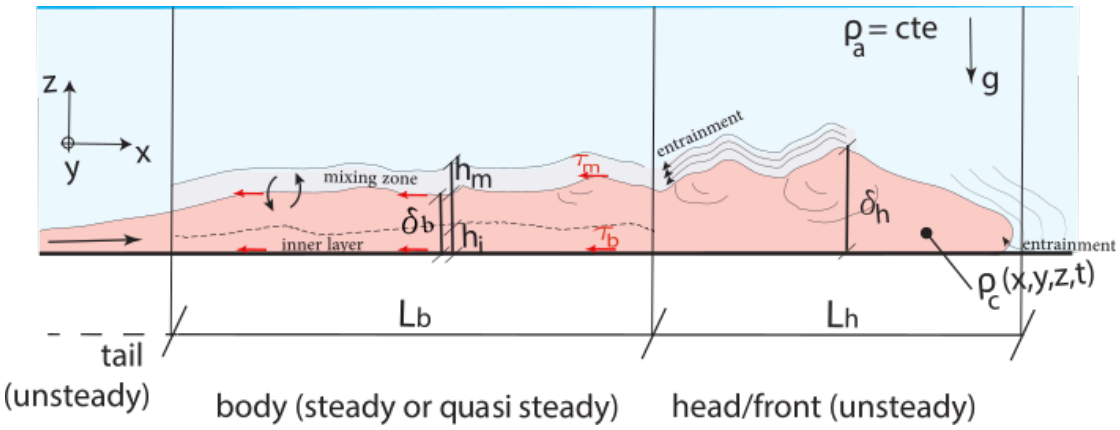

Figure 4.1: Schematic of a gravity current (description of all terms is provided in the text).

characterized by distinctive turbulent dynamics. Due to friction, substantial mixing occurs, mainly in the early stages of the evolution of lock-release gravity currents, and this mixing leads to the formation of a complex internal density structure (Hacker et al., 1996). Inner and upper layers, even if affected by different vortical movements, are mutually interacting. For this reason, simplified models, such as two-layer shallow water models need a suitable entrainment parametrization to correctly simulate the dynamics of a lock-release gravity current (Fragoso et al. (2013), Ottolenghi et al. (2016a)). This brings to the last point, that concerns the entrainment parametrization. It is proposed to estimate the entrainment capacity on the base of the shear stress time evolution. Assuming a logarithmic velocity distribution in the vicinity of the bed, the friction velocity and consequently the bed shear stress can be estimated. Bed shear stress measurements for each instantaneous averaged profile are determined and so the impact on the flow transport capacity may be assessed for the different regions of the current (head and body).

Finally, it is shown that the variation of the initial conditions have consequences on (i) the configuration of the currents and on (ii) the hydrodynamics of the currents, including mass and momentum exchanges, which are in addition mutually dependent.

4.2 Methods

This is the first group of tests, as explained in Section 3.2.2. The configuration of the flume is shown in Figure 4.2. For this set-up, the bottom of the channel is horizontal and smooth. Five lock volumes are created by shortening the upstream wall of the channel so reducing the length (L_i) of the portion of the channel where the denser fluid is situated. The rest of the set-up is unchanged. Three initial densities in the lock are tested, combined with five sizes of the upstream reach of the channel. The experimental parameters are reported in Table 5.1.

The Acoustic Doppler Velocity Profiler (ADVP) is used to record instantaneous 3D velocities along a vertical, 2.5 m downstream from the gate (Figure 4.2). A despiking procedure (Goring and Nikora, 2002) and a low-pass filter applied to the noisy frequencies, after analysis of the power spectra of the raw data, allowed considerable reduction of the noise, as explained in Chapter 3.3.3.

4.3 Results

4.3.1 Flow description

The mean streamwise velocity field is shown in Figure 4.3 by a color map which contains on the top the 2D vector field corresponding to the streamwise and vertical components. Normalization is made using the time scale $t^* = h_b/u_b$, where h_b is the vertical length scale and $u_b = \sqrt{g' h_b}$ the buoyancy velocity (c.f. Chapter 3.2.2).

In Figure 4.3, we can notice that shorter currents are formed by increasingly shorter lock lengths, beginning with an initial length of the lock of 2.5 m. Increasing initial current densities results in larger streamwise velocities. For all the tests, a well defined arising head is identified. This is the region where the higher values of streamwise velocity are detected, at around one third of the current height, as was also observed in literature (Kneller and Buckee, 2000). On the rear part of the head, at around $t/t^* = 15$, the interface is characterized by a zone of instabilities with the formation of billows. The vector field allows the visualization of the Kelvin-Helmholtz type of instabilities caused by the shear between the head and the ambient fluid, that moves fluid clockwise enhancing mixing and ambient water entrainment.

The general shape of the gravity currents is composed of an arising head followed by a body, with stable condition, then a tail where flow velocities and flow depth decay. The extent of the body is seen to increase for longer lock lengths. Corresponding to the dense flow that moves at the bottom in the positive streamwise direction, an opposite movement of ambient water forms on the top. This counter-current does not have a defined front but shows a jet-like configuration that is more defined for higher gravity current velocities.

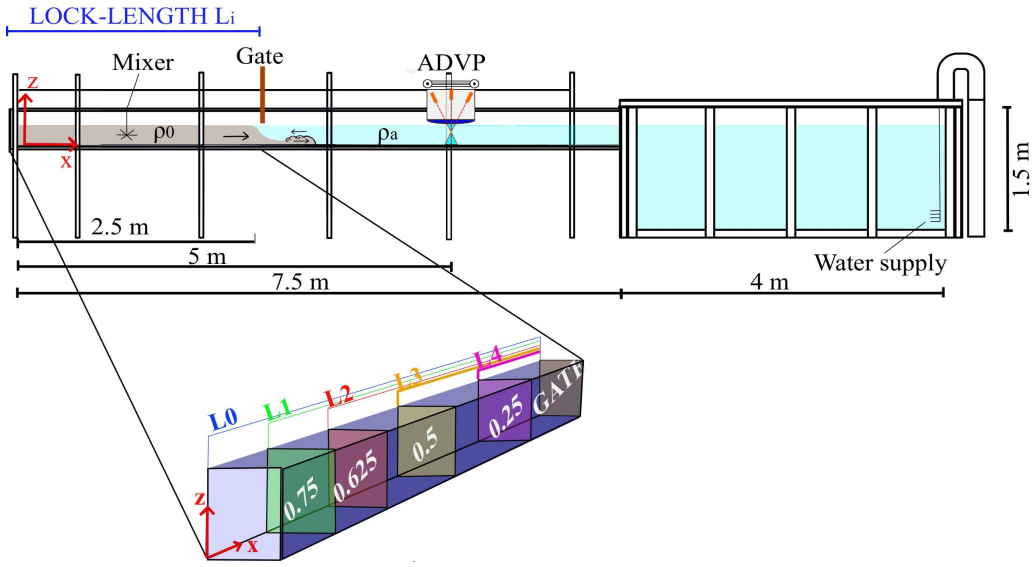

Figure 4.2: Side view of the experimental set-up.

$\mathbf{L}_i$ **Exp.**	ρ_0 (kg/m^3)	L_i (m)	V_i/V_0 $(-)$	R_i $(-)$	g_0' (m/s^2)	u_0 (m/s)	Re_0 $(-)$	ΔT $(°C)$
R1.L0	1028	2.500	1.000	0.080	0.29	0.24	48166	
R1.L1	1028	1.875	0.750	0.107	0.29	0.24	48166	
R1.L2	1028	1.563	0.625	0.128	0.29	0.24	48166	≤ 1
R1.L3	1028	1.250	0.500	0.160	0.29	0.24	48166	
R1.L4	1028	0.625	0.250	0.320	0.29	0.24	48166	
R2.L0	1038	2.500	1.00	0.080	0.39	0.28	55857	
R2.L1	1038	1.875	0.750	0.107	0.39	0.28	55857	
R2.L2	1038	1.563	0.625	0.128	0.39	0.28	55857	≤ 1
R2.L3	1038	1.250	0.500	0.160	0.39	0.28	55857	
R2.L4	1038	0.625	0.250	0.320	0.39	0.28	55857	
R3.L0	1048	2.500	1.000	0.080	0.49	0.31	62610	
R3.L1	1048	1.875	0.750	0.107	0.49	0.31	62610	
R3.L2	1048	1.563	0.625	0.128	0.49	0.31	62610	≤ 1
R3.L3	1048	1.250	0.500	0.160	0.49	0.31	62610	
R3.L4	1048	0.625	0.250	0.320	0.49	0.31	62610	

Table 4.1: Experimental parameters. ρ_0 is the initial density of the mixture in the upstream tank (measured with a densimeter), L_i is the length of the upstream reach, V_i/V_0 the proportion of volume of the upstream reach with respect to the configuration L_0, $R_i = h_0/L_i$ is the aspect ratio of the lock with $h_0 = 0.2$ m the total height of the water column, g' is the reduced gravity corresponding to ρ_0, $Re_0 = u_0 h_0/\nu_c$ is the Reynolds number based on initial quantities with $u_0 = \sqrt{g' h_0}$ the initial buoyancy velocity and ν_c the kinematic viscosity of the denser fluid and ΔT is the difference in temperature between the temperature of the mixture, T_0, and the temperature of the ambient water, T_a (measured with a thermometer before each experiment).

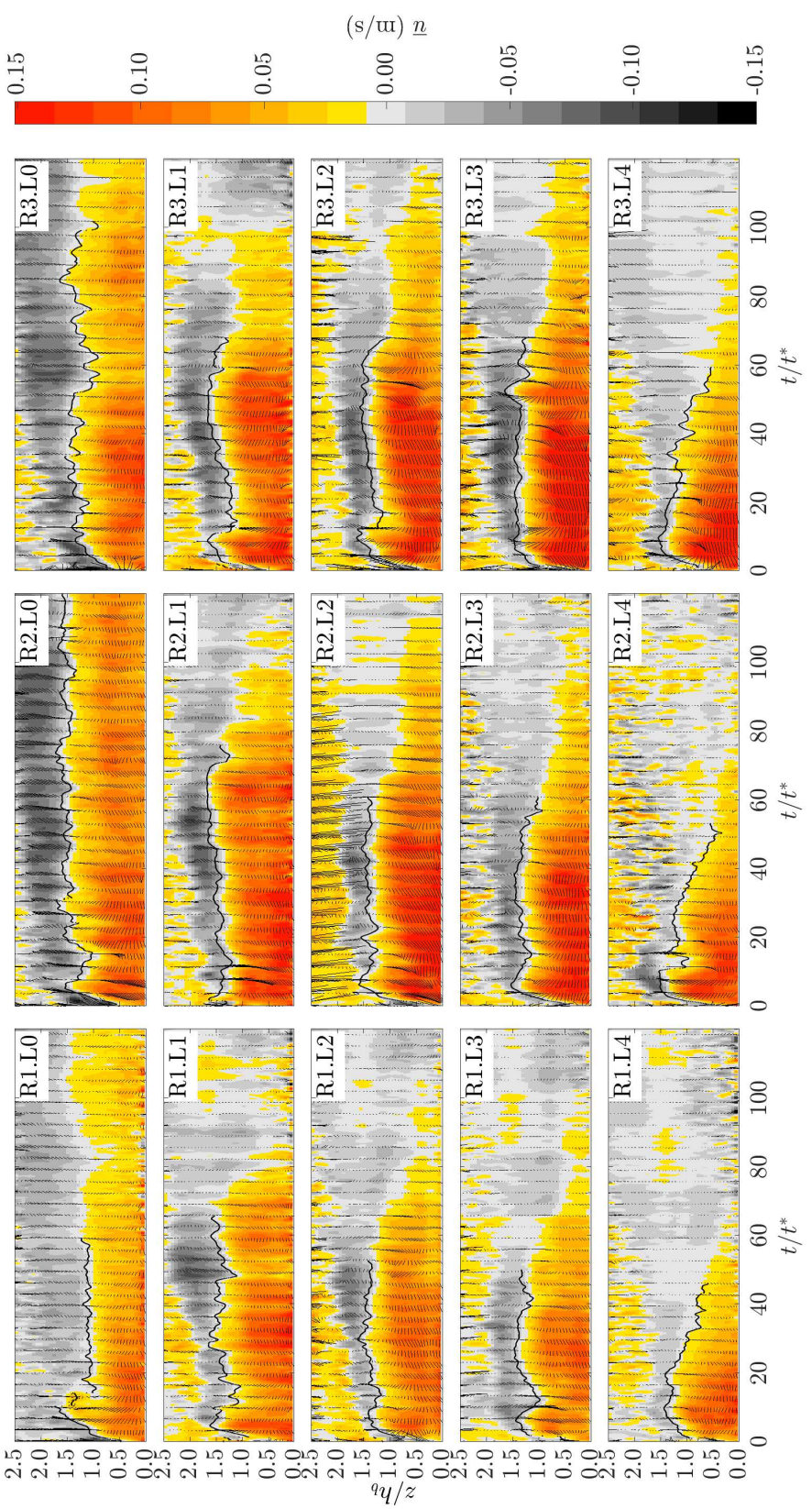

Figure 4.3: Mean streamwise velocity field with on the top the 2D vector field, corresponding to the streamwise and vertical components. The zero streamwise velocity contour is also traced

4.3.2 Anatomy of lock-released gravity currents

Head and body are known to have different hydrodynamics and consequently different roles in sediment entrainment and transport of mass and momentum.

The head is the region of the current where most of the mixing processes take place and it is characterized by a three-dimensional behaviour (Allen (1971), Britter and Simpson (1978), Nogueira et al. (2014a)). Billows due to Kelvin-Helmholtz instability are detected in the shear zone at the upper and rear part of the elevated head (Simpson, 1972). The elevation of the head can reach twice the height of the following steady flow, as confirmed by the literature (Simpson (1972), Nogueira et al. (2014b)). The lower boundary has been confirmed to play an essential role in the structure of the head by Simpson (1972), so when analysing the feedback between the density current and the bed it is important to identify the head.

To characterize and isolate the head, the kinematic function (H) is used. The downstream limit of the head is identified by the first meaningful local minimum of the function H, that is defined as:

$$H(t) = u_d(t)h(t) \tag{4.1}$$

being $u_d(t)$ the instantaneous depth averaged streamwise velocity computed as:

$$u_d(t) = \frac{1}{h}\int_0^h \overline{u}(z,t)dz \tag{4.2}$$

and $h(t)$ the current height that is here identified by the position where the streamwise velocity is equal to zero. This is in fact considered the upper limit of the gravity current: it corresponds to the point of inversion of the streamwise velocity profile and a fluid moving with negative streamwise velocity is recognised as not belonging to the current. Moreover we can notice that by dimensional analysis the function H corresponds to a discharge per unit width.

The downstream limit of the head is identified by the first meaningful local minimum of the function H starting from the front. In Nogueira et al. (2014a) a similar procedure was adopted where the head was identified by considering the product of the depth averaged streamwise velocity by the depth averaged density of the current. The algorithm used herein to detect the limit of the head evaluates how much the minimum of H is separated from the other maximum values. A low isolated trough can be more prominent than one that is higher but is surrounded by many peaks. In Figure 4.4 the variables composing the function H are presented for one representative test.

Figure 4.5 shows the computed function H for all the tests of this first group. The square symbols identify the first meaningful local minimum of H and the vertical black lines represent the averaged positions of the head limit in time (L_h), considering the tests grouped by the same lock-length.

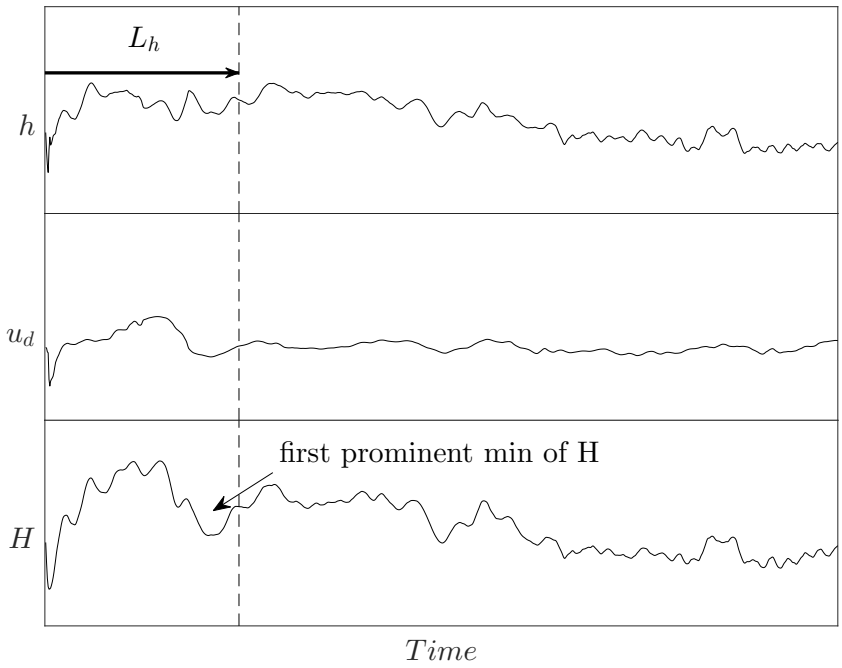

Figure 4.4: Definition of the gravity current head from the identification of the first prominent minimum of the function H. This point identifies the head length (L_h). To determine the function H (i) the contour of the current, $h(t)$, is identified, (ii) the instantaneous depth averaged velocity is calculated and (iii), by multiplying the two previous variables, $H(t)$ is found.

The observation of the temporal series of the instantaneous streamwise velocity field of the current (Figure 4.3), revealed that after the head passed, there is a period of fairly constant streamwise velocity which is longer lasting with the increase of the lock length. This is also observed in the time-series of H in Figure 4.5, where a nearly flat region can be noticed after the head limit. In order to identify the extent of the body, the cumulative sum of H ($\sum H$) is used (an example is shown in Figure 4.6 for tests with lock-length L2). In Figure 4.6 the head extension (L_h) is marked by the vertical lines. Variable $\sum H$ has a linear evolution which is fitted by a linear regression with least squares method for progressively longer portions of the accumulated summed data (red lines). The R^2 value was analysed in order to find the optimum extension of the linear portion which corresponds to the temporal extent of the body region (L_b).

The extensions of the head (L_h) and body (L_b) so determined are compared in Figure 4.7a, for tests with different initial buoyancies and varying lock-length (L_i). A proper parametrization for the x-axis was found after dimensional analysis as in Hallworth et al. (1993) and it is here

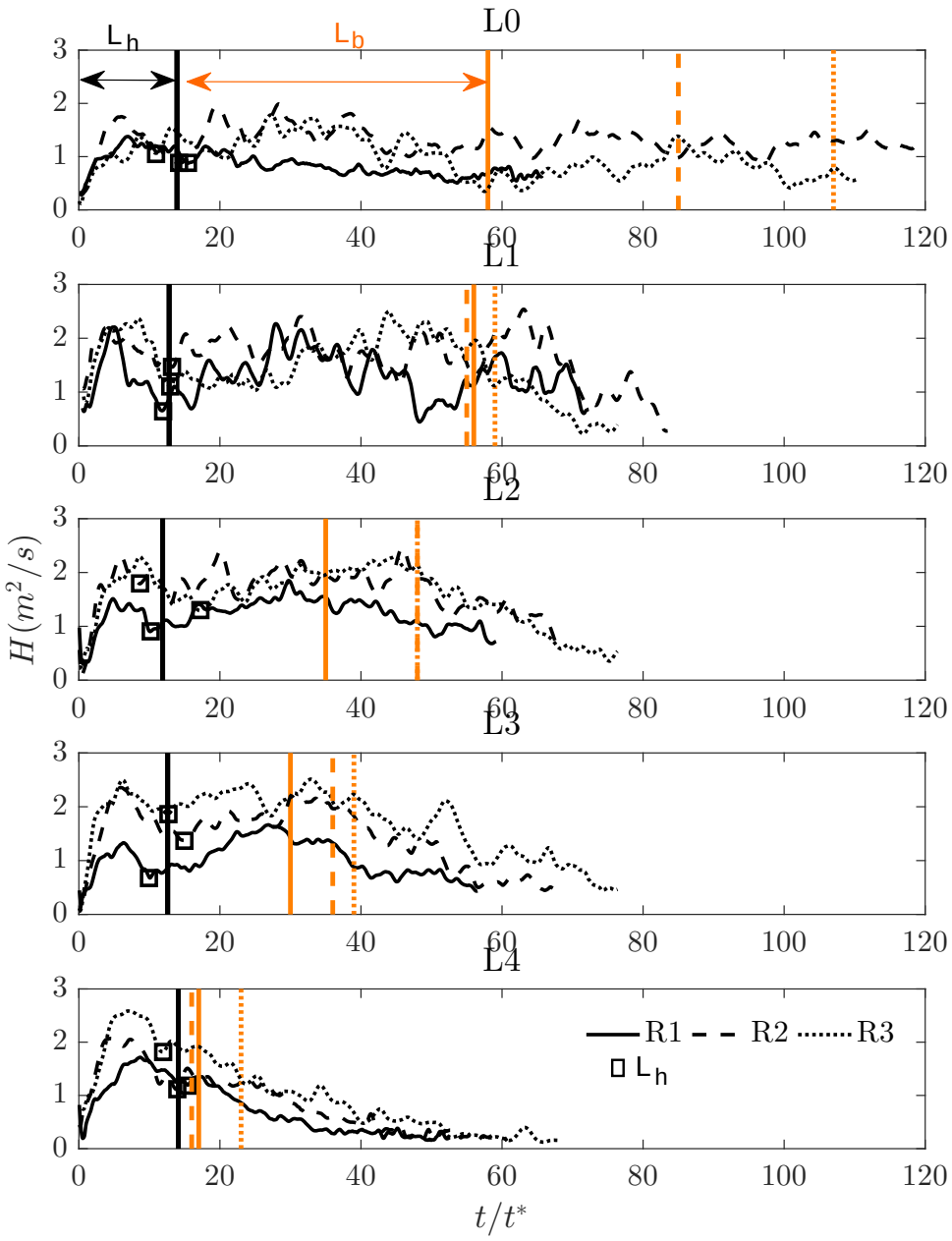

Figure 4.5: Definition of the gravity current head from the identification of the first prominent minimum of the function H. This point identifies the head length (L_h). The extension of the body, as identified by the cumulative sum of H, is also traced with the red vertical lines.

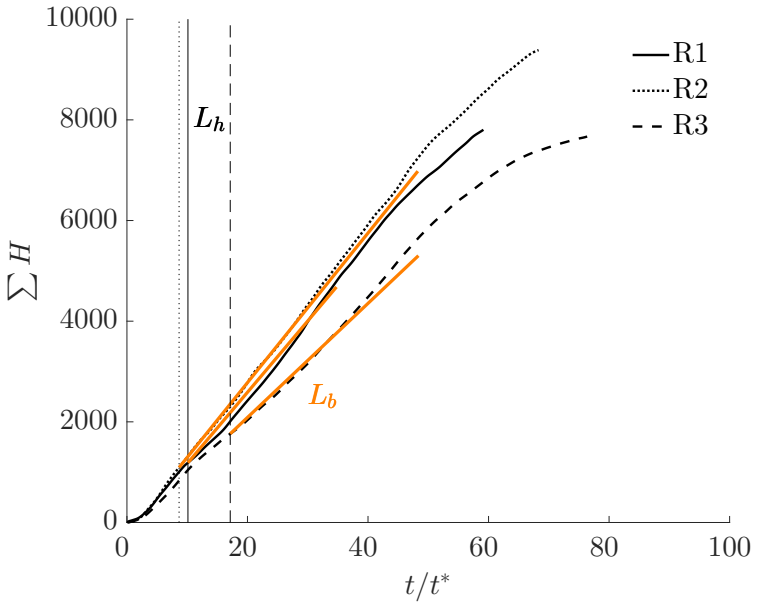

Figure 4.6: Time evolution of the cumulative sum of the function H, defined as in Equation 4.1. Vertical black lines delimit the head extension (L_h) and red line are the linear regression of the function from L_h to the limit of the body (L_b).

adopted. Consider V_i the initial volume of release contained in the lock, which density is ρ_0. As suggested in Hallworth et al. (1993), the variation on the shape of the current, mainly consequence of water entrainment, depends on: V_i, of dimension $[L^3]$, the initial reduced gravity g'_0, of dimension $[L/T^2]$, and the distance from the release point, L_p, $[L]$. If we define the variation of the volume of the gravity current as $V_i/(V_i + V_a)$ where V_a is the volume of entrained ambient water, it follows that, since this latter is dimensionless, it must be independent of g'_0 that is the only one containing the temporal scale $[T]$. The dependence is therefore just on: initial volume and distance from the release of the point of observation (here measurements are collected at a distance L_p from the gate). In order to take into account both, the normalization proposed is V_i/V_p, where V_i is the initial volume of release and V_p the volume available for the propagation of the release until the observation position, which divided by the constant cross section of the channel, results equivalent to L_i/L_p.

In Figure 4.7b, the thicknesses of these regions (δ_h and δ_b) are also compared by considering (i) for the head, the maximum value of the contour of the current along the extent L_h; (ii) for the body, the average value of the contour of the current along the extension L_b. Here it is shown that the maximum height of the head and the average height of the body generally increase with longer lock-lengths. The influence of the initial buoyancy appears not to be relevant. The length of the body, as expected, increases for longer lock-length. Instead, the head length is kept fairly constant and independent from the initial density in the lock and from the volume of release.

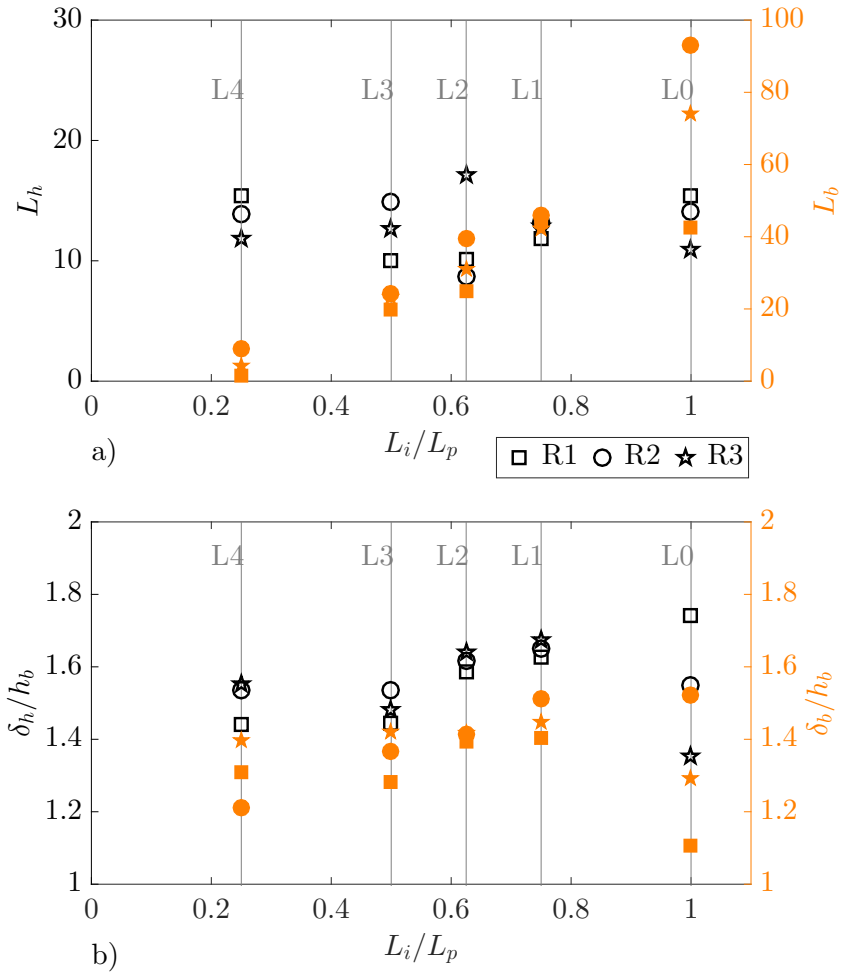

Figure 4.7: a) Length in normalized time (t/t^*) of the head (L_h) and of the body (L_b) for gravity currents formed by changing lock-lengths (L_i/L_p). b) Comparison of normalized maximum height of the gravity currents head (δ_h/h_b) and average height of the body (δ_b/h_b). Empty symbols refers to the head and filled are for the body.

4.3.3 Vorticity field

The analysis of the turbulent dynamics can be attempted by computing the vorticity field. Figure 4.8 shows the current spanwise vorticity computed as:

$$\eta_y = \frac{\partial w}{\partial x} - \frac{\partial u}{\partial z} \tag{4.3}$$

with the following algorithm as proposed by Sveen (2004) and Raffel et al. (2013):

$$\left.\frac{\partial w}{\partial x}\right|_{i,j} = \frac{2w_{i+2,j} + w_{i+1,j} - w_{i-1,j} - 2w_{i-2,j}}{10\Delta x} \tag{4.4}$$

$$\left.\frac{\partial w}{\partial z}\right|_{i,j} = \frac{2u_{i,j+2} + u_{i,j+1} - u_{i,j-1} - 2u_{i,j-2}}{10\Delta z} \tag{4.5}$$

where i and j are the streamwise, x, and vertical, z, coordinates of the measuring point, respectively, Δx and Δz being the distances in both directions between adjacent points. For the vertical direction the distance between two subsequent gates is considered (Δz) while for the streamwise (Δx), the conversion from time to length scale is made using Taylor frozen hypothesis considering the current front velocity as advection velocity. This is allowed if we consider that the turbulent eddies are not deformed by the transport imposed by mean and turbulent velocity fields and so the link between the two dimensions can be made (Franca and Brocchini, 2015).

The spanwise vorticity field in Figure 4.8 shows a region of high negative vorticity, indicating the presence of clockwise movements of vortical structures. It is here where the higher rate of exchange between the two fluids takes place mainly as entrainment of ambient water into the gravity current. Two lines are also marked in Figure 4.8. The green line corresponds to the zero velocity contour ($\overline{u} = 0$). The blue contour is identified using the integral time scales of Ellison and Turner (1959) ($E\&T$) as reported in Equations 2.12a, b. The mean streamwise velocity time series is used for the calculation of the integral scales and the result is a time dependent depth-averaged current thickness. In Equations 2.12a, b, the upper limit ∞ is replaced by the distance from the bed to the zero velocity interface between the current and the ambient water above, as was done by Sequeiros et al. (2010a).

The region of intense vorticity appears to be delimited by those two previously defined contours (the green and blue lines in Figure 4.8): even if clear boundaries cannot be defined, the zero-velocity contour and the Turner's height prove here to be a valid indicator of the approximate limits of the mixing zone and they will be used hereafter. A verification was also performed by checking the position of $du(t)/dz = max$. At this point the shear stress is maximum and so is the momentum transfer (Lofquist, 1960). This height can be used to differentiate an inner region and outer region of the flow with opposite velocity gradient (Kneller et al., 1999). It is here therefore verified that this ($du(t)/dz = max$) is located between the two previously identified contours.

The thickness of the mixing zone is compared among tests and shown in Figure 4.9. A clear tendency with the initial reduced gravity is not distinguished. Instead there is a weak dependency on the lock-length with the exclusion of tests in configuration L0. The linear trend line has been traced in Figure 4.9, by omitting points R1.L0 and R3.L0 and it suggests that the extension of the mixing zone increases with the volume of release.

In Figure 4.8, the bodies of the gravity currents present a zone of intense negative vorticity in correspondence with the mixing zone, which fades downward toward the bottom. Residual negative values of vorticity with lower intensity occur along the body.

Positive vorticity, with counter-clockwise movement of vortical structures, is mainly present in the core of the head and in the vicinity of the bottom. This region is more evident in tests originated by shorter lock-lengths and by greater initial buoyancy.

In order to summarise the general structure of the vorticity field that is typically recognised in the tests here performed, a sketch is shown in Figure 4.10. Three main zones are identified and indicated with the dashed contours. In red there is the upper layer of the gravity current that strongly interacts with the ambient fluid. The flow in this mixing zone is dominated by movements which go inversely with respect to the direction of the main flow and this is evidence of the presence of Kelvin-Helmholtz vortices that are shear layer instabilities whose strength decreases with time, becoming almost absent in the tail of the current. In green there is the region which is highly influenced by the vortical structure in the mixing zone. Residual negative vorticity expands from the upper layer towards the bottom, showing progressively lower intensity. The interaction between the upper layer and the bottom was already pointed out by the numerical investigation of Cantero et al. (2008) and here confirmed by experimental evidence. In blue is the intense positive vorticity at the core of the head which confirms the presence of an inner movement rotating in the direction of the principal motion.

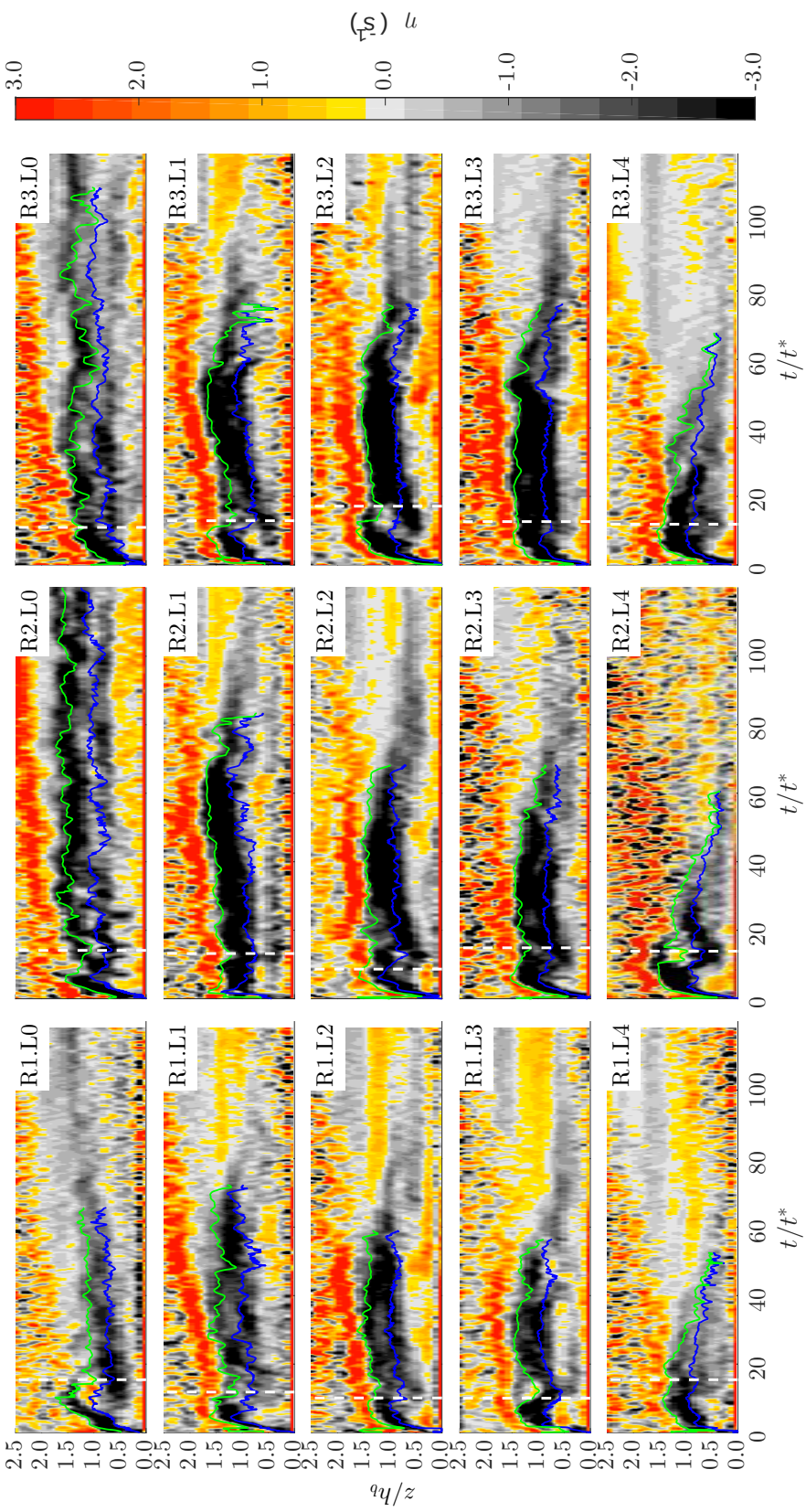

Figure 4.8: Spanwise vorticity field calculated following Equation 4.3. The green lines are the zero velocity contours ($\overline{u}$=0) and the blue lines are the contours identified using the integral time scales of Ellison and Turner (1959) (Equation 2.12a,b, *E&T*) .

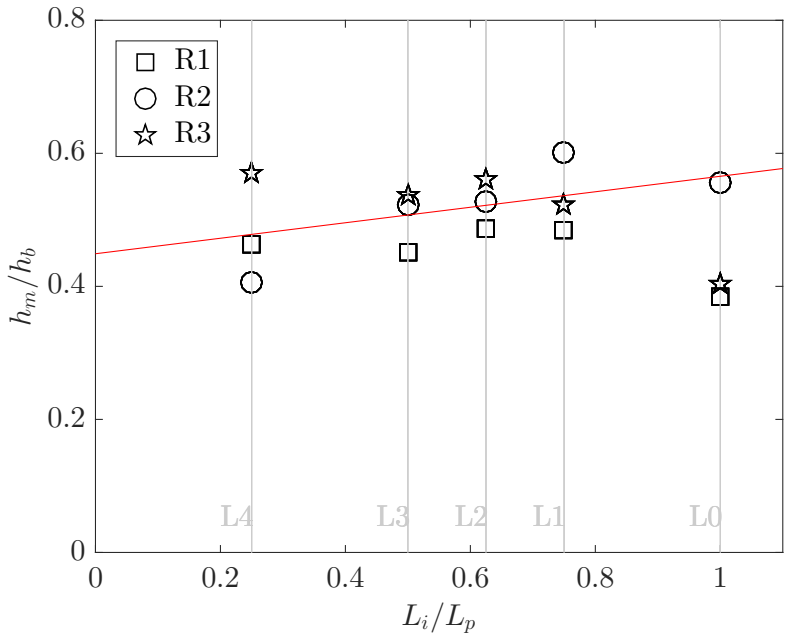

Figure 4.9: Thickness of the normalized mixing zone (h_m/h_b) compared for gravity currents formed by changing lock-lengths (L_i/L_p).

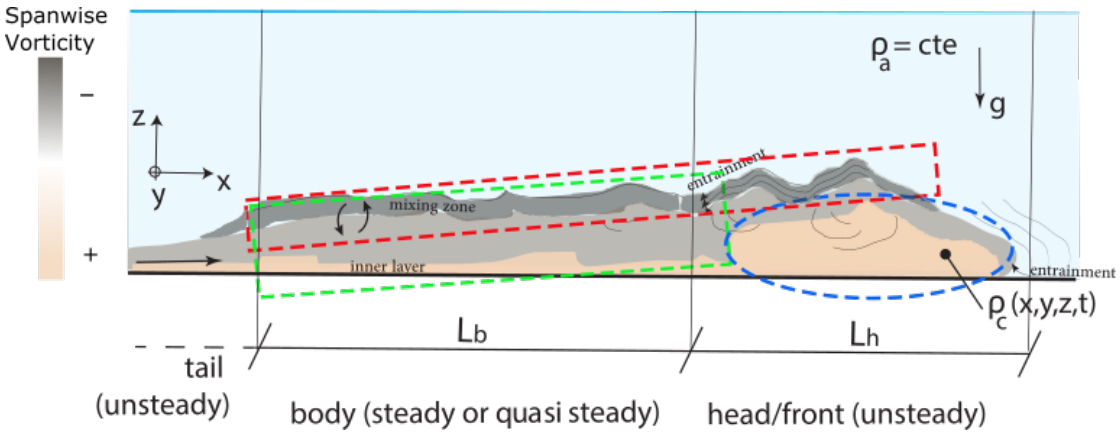

Figure 4.10: Sketch of the general structure of the spanwise vorticity field with the three main zones highlighted by the dashed contours.

4.3.4 Bed and interfacial shear stresses

The time evolution of the shear stress, at the bottom and at the interface with the ambient water, is here calculated. The fitting of the logarithmic law of the wall is used in order to estimate a friction velocity (as described in Appendix A). The fitting procedure of the logarithmic layer is adopted for each instantaneous mean profile collected with the ADVP instrumentation thus an estimation of the bottom (τ_b) and interfacial shear stress (τ_m) is made for each measuring instant.

(1) For the bed layer the presence of the logarithmic layer can be inferred by assuming a flow that is essentially two dimensional in the vertical plane and with high relative submergence. The bed shear stress is therefore computed as explained in Chapter 2.5.2.

(2) For the upper boundary of the gravity current, studies on turbulent flow near a density interface confirmed that under certain conditions, the turbulent boundary layer theory can be applied (Lofquist (1960), Csanady (1978)). In particular, the velocity distribution shows a viscous sublayer and a buffer layer (Csanady, 1978). Even if some key parameters change with respect to the conditions along a solid wall, the "law of the wall" is still suitable. The classic value of the von Kármán constant of $k = 0.405$ can here be adopted, as confirmed by Csanady (1978). Instead the effective viscosity and the hydrodynamic roughness are found to vary with respect to the smooth boundary layer condition. The effective viscosity increases due to the presence of viscous wavelets and the roughness is affected by the instability of the interface (Csanady, 1978). If the computation is done under the assumption of hydraulically smooth flow and considering a constant mean value of water viscosity, there will be a deviation in the estimation of the actual absolute value of interface shear stress. Since the purpose is to have an indication of the temporal development of shear at the interface, to the detriment of the quantification, a qualitative estimation is attempted. In this case the fitting procedure of the logarithmic layer is determined by considering the mixing layer as defined in Chapter 4. This layer is delimited at the top by the zero streamwise velocity contour and at the bottom by the height of the current as defined by the Turner's integral scales (Ellison and Turner, 1959). Within this layer the at-least-three consecutive measurement points along the velocity profile which were giving the highest R^2 were considered for fitting.

The evolution of the shear stresses is shown in Figure 4.11. The shear stresses generally show greater values in the frontal region of the current. Values are greater for currents of larger initial density and in the case of shorter lock-length. The body presents large peaks of interfacial shear stress, for a length that is proportional to the extension of the body itself, followed by a steep diminution. The evolution of the bed shear stresses within the body is instead characterized by progressively lower values.

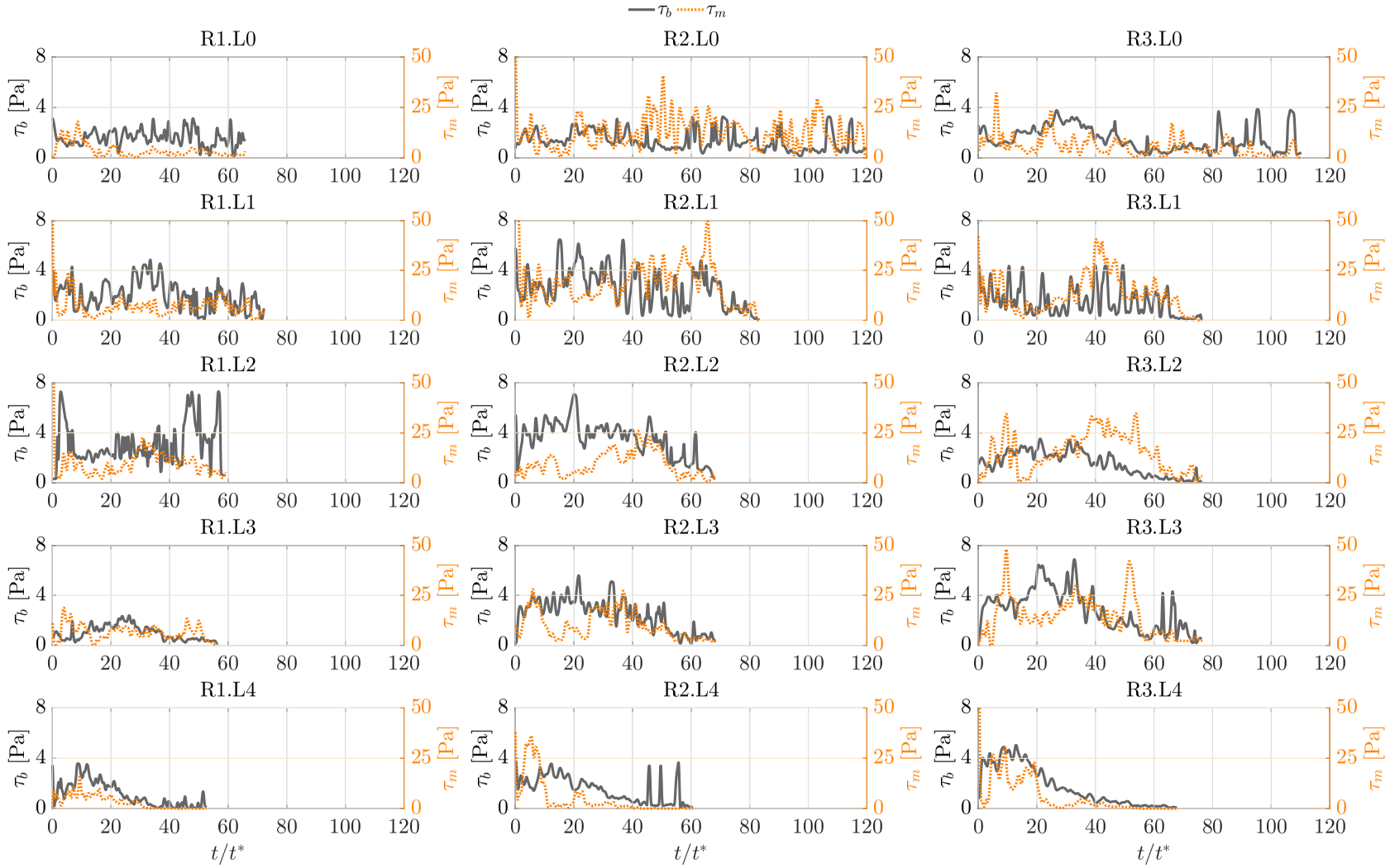

Figure 4.11: Temporal evolution of bed and interfacial shear stresses calculated by fit of the log law.

4.3.5 Ambient entrainment and bottom erosion

A new quantity is defined which accounts for the potential water entrainment capacity of the gravity current on the basis of the computed time evolution of the interfacial shear stress (τ_m). It is computed as the non-dimensional time integral of the shear stress which represents, after dimensional analysis, the work done over a determined duration, per unit surface for a given advection velocity, being the initial buoyancy velocity, u_0, a proxy of this latter. This quantity Φ_m is calculated as:

$$\Phi_m = \int_{T_1}^{T_2} \tau_m(t)\, dt/t^* \tag{4.6}$$

Similarly to the interfacial water entrainment capacity, the sediment potential entrainment capacity, is here computed as:

$$\Phi_b = \int_{T_3}^{T_4} \tau_b(t)\, dt/t^* \tag{4.7}$$

The limits of integration T_i are in this case chosen to be $T_1 = 0$ and $T_2 = L_b$ since the relevant water entrainment takes place along the whole upper interface and and $T_3 = L_h$, $T_4 = L_b$, in order to focus on the bottom entrainment capacity of the body, the region that has been found to be most affected by the variation of the initial conditions.

Figure 4.12 shows that the entrainment capacity from both bottom and upper layers is increasing for tests with longer lock-lengths.

4.4 Discussion on the entrainment parametrization

When the density difference of a gravity current is originated by a dissolved substance that has a low diffusivity, its horizontal propagation is generally much larger than its vertical extent (Huppert, 2006). Thus standard shallow water theory can be applied since, for high enough Reynolds numbers, the equilibrium is established mainly between inertial and buoyancy forces (Whitham and Fowler, 1975). These models are robust and accurately describe the front speed and height of the flow, but they cannot resolve the spatio-temporal entrainment of ambient fluid for which they thus need a parametrization.

Entrainment from the upper and bottom layers into the gravity current modify the structure of the flow and its dynamics. At the upper boundary, if the turbulence is not damped by the buoyancy effect, instability occurs due to shear at the surface of contact with the ambient water. The competition between the stabilizing effect of buoyancy and the destabilizing shear is captured in a dimensionless parameter, the gradient Richardson number. For a continuously stratified flow, a more global form of Ri, which characterises the stability over the whole depth

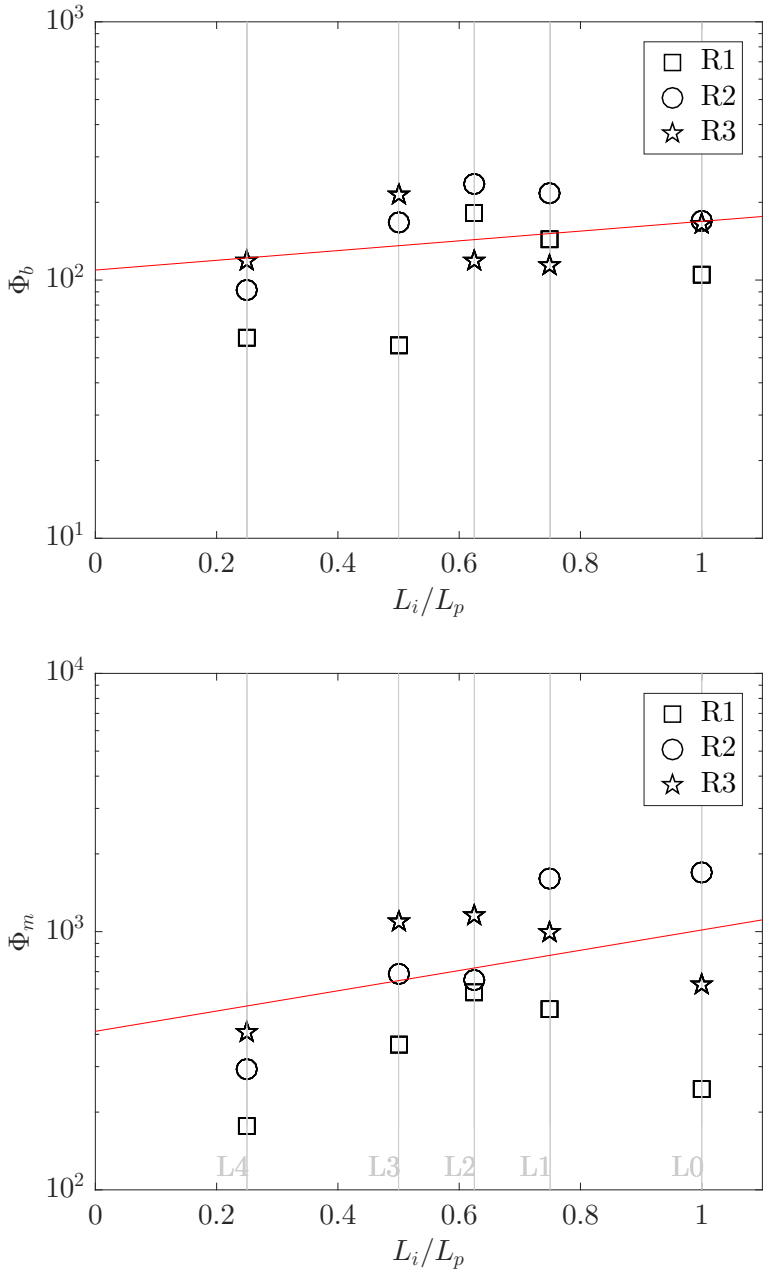

Figure 4.12: Respectively potential bottom and upper entrainment, Φ_b and Φ_m, compared for gravity currents formed by changing lock-lengths (L_i/L_p). The lines help to visualize the general trend.

rather than at specific positions, is the bulk Richardson number, Ri_b:

$$Ri_b = 1/Fr_D^2 = \frac{g' h_b}{U} \tag{4.8}$$

where Fr_D is the densimetric Froude number and U is the layer-averaged velocity, a characteristic velocity of the current. For high enough Reynolds numbers ($Re > 10^4$), the mixing transition is passed, thus 3D turbulent inertial range develops and the mixing completely homogenises the fluid captured by the Kelvin-Helmholtz instability (Wirth, 2015).

The relation between water entrainment and bulk Richardson number is well known in literature and numerous empirical fits to the experimental data have been proposed since Ellison and Turner (1959) (Parker et al. (1987), Johnson and Hogg (2013)). The upper resistance of the flow is certainly linked with the water entrainment and is here proved by comparing the time integral of the shear stresses as Φ_m with the Richardson number Ri_b (Figure 4.13). The data, similarly to the work of Parker et al. (1987) and as sustained by Johnson and Hogg (2013), show that entrainment decays approximately as $\Phi_m \sim Ri_b^{-1}$, that applies for high Richardson numbers. This supports the validity of the new here defined Φ_m as an indicator for water entrainment.

In Figure 4.14, Φ_m is plotted against the mean thickness of the mixing zone (h_m). The relation between the extent of the mixing layer with the interfacial shear stress, and in particular with the potential water entrainment i.e. Φ_m, is here demonstrated. Larger mixing layers were found to be responsible for a greater entrainment discharge of ambient water from the upper surface into the gravity current (Theiler and Franca, 2016). On the other hand a higher rate of water entrainment is responsible for the dilution of the mixing zone which is likely to thicken. Moreover water entrainment is shown to be independent of the initial density in the lock, as confirmed in Hallworth et al. (1993) and Hallworth et al. (1996) through the dimensional analysis as reported in Section 4.3.2.

At the bottom, in order to evaluate the potential contribution for erosion by the body of the current on the total bottom erosion capacity of the current, the ratio $\Phi_{b\ body}/\Phi_b$ is computed. In Figure 4.15 it is shown that for the shortest lock-length tests the body plays a minor role. Indeed in this case the body of the current is so reduced that the potential entrainment of sediment from the bottom is governed by the highly turbulent head. For the rest of the experiments with longer locks it is instead the body that drives the erosion capacity.

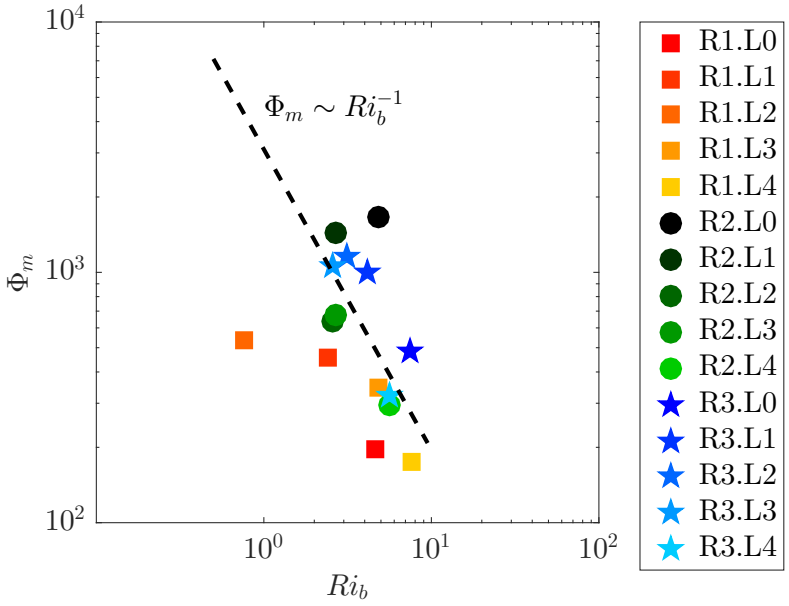

Figure 4.13: Gravity current entrainment capacity Φ_m related with bulk Richardson number Ri_b. The continuous black line indicates the fit of the data (excluding one outlier, test R1.L2).

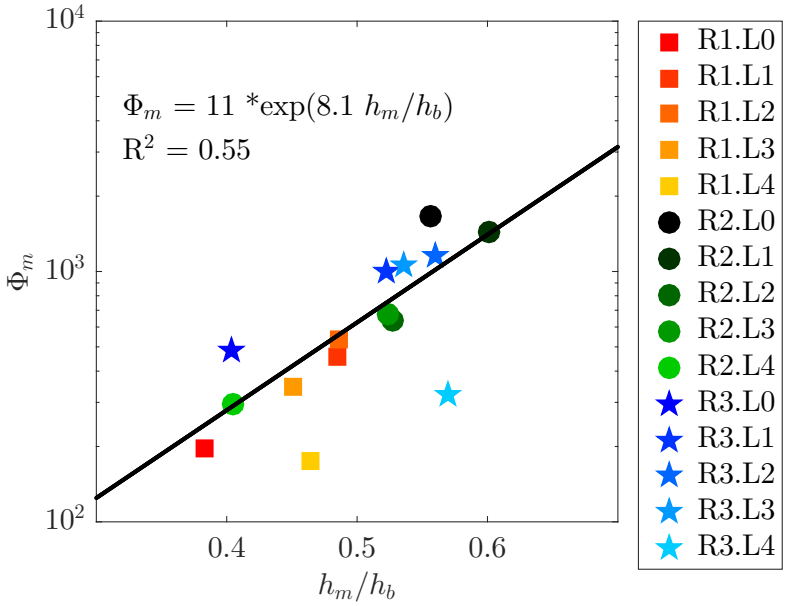

Figure 4.14: Relation between mean thickness of the normalized mixing zone (h_m/h_b) and time integral of the interfacial shear stress Φ_m. The data are exponential fitted by the relation reported on the plot. The R^2 coefficient of determination is also reported.

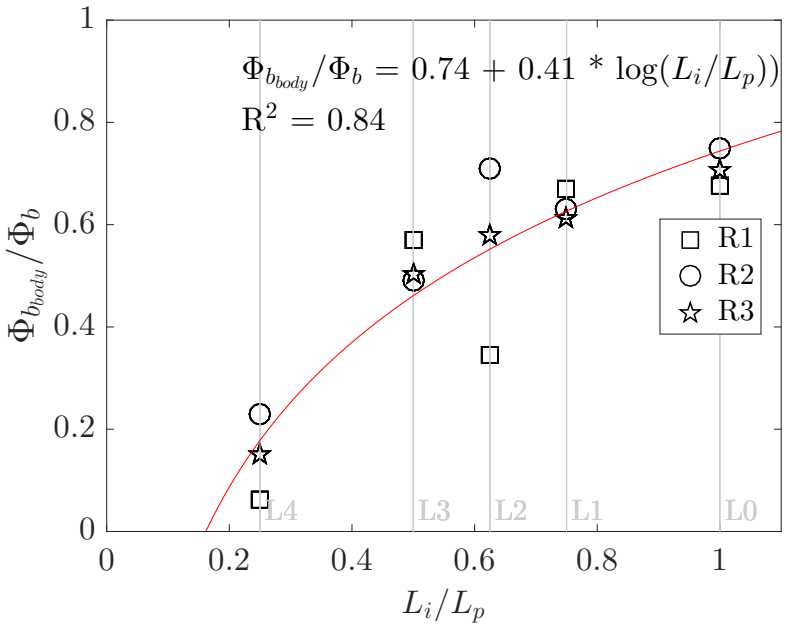

Figure 4.15: Rate of potential contribution for bottom erosion due to the body of the gravity current on the total bottom erosion capacity ($\Phi_{b\ body}/\Phi_b$) for gravity currents formed by several lock-lengths (L_i/L_p). A fitting is reported in order to give evidence of the general trend. The R^2 coefficient of determination is also reported.

4.5 Conclusions

In this Chapter the horizontal and vertical structure of gravity currents produced by varying lock-released initial volumes is investigated. A method to distinguish the head and body regions is established. The flow field of a gravity current has been characterized paying particular attention at the bottom and interface layers. It is shown how the lock-length influences the horizontal extent of the body of the gravity current while the head is not affected by the initial volume of the release.

Vertical transport through the gravity current is influenced at the bottom by the solid wall over which the current flows, and at the upper interface by the contact with the ambient water. The characterization of the shear stress is of importance since it competes with the buoyancy determining mixing and entrainment. Therefore the time evolution of shear stress at both the interface and bottom are calculated. With a proper normalization that take into account the dependence of the gravity current evolution on both initial volume of release and point of observation, a relation between the resistance at the bottom and at the upper interface with the initial lock-length has been found, while their independence from the initial density in the lock confirmed.

The turbulent flow enhances redistribution of contaminants or sediments from the bottom, and entrainment of water at the upper interface. At the interface, the mixing zone thickness, characterized by the presence of Kelvin-Helmholtz instabilities, increases exponentially with the time integral of the shear stress as a consequence of the dilution due to water entrainment. At the bottom, inner vortical structures rotating in the direction of the principal motion are detected. Those are stronger in tests with shorter locks and greater initial reduced gravity. The contribution of the body in the potential sediment entrainment capacity from the bottom is generally more significant than the one of the head for all the tests except the shortest lock where the current is composed of head and tail only.

5 Influence of incremental gravitational energy on gravity current hydrodynamics

Chapter 5 is based on the scientific article "Geomorphic implications of gravity currents created by changing initial conditions" by J. Zordan, A.J. Schleiss and M.J. Franca under revision in Earth Surface Dynamics. The experimental work and the analysis presented hereafter is original and was performed by the author.

5.1 Introduction

In most practical situations gravity currents are flowing on an inclined bed. This introduce extra gravitational energy which is affecting its hydrodynamic. Snow avalanches down the slopes of the mountain or turbidity currents which follow the inclined thalweg of a reservoir until reaching the dam are common examples. In the shallow shelf region of the lake it is observed that cold water, relatively denser than that in open waters, starts to descend down the slope as a cold gravity current (Fer et al., 2002). The plume is able to transport suspended sediment together with their dissolved components, oxygen, and pollutants into deeper water.

Frequently, the slope is not continuous and, as it is along the continental slope or in the lakes, a shelf-slope break is present. Therefore an extra potential energy is imparted to the plumes which are initiated along the inclined, due to the raised position of the center of mass with respect to the following horizontal bottom.

While for gravity currents travelling on a horizontal bed, pressure gradient and buoyancy forces are the driving factors, the dynamics of flows on slope are controlled by the balance between the gravitational acceleration and dissipation forces. The main purpose is here to investigate how the increment of gravitational energy, due to the introduction of a slope in the lock, affect the hydrodynamics of gravity currents and consequently their transport capacity. A range of lock-slopes is tested, going from horizontal to a limit case in which two mechanisms compete, i.e. the current entrainment of water from the upper surface due to the increment of friction and the head feeding by the rear steady current.

5.2 Methods

This is the second group of test, as explained in Section 3.2.2. The configuration of the flume is shown in Figure 5.1. Three buoyancy differences are tested in combination with five lock-slopes, ranging from $S = 0\%$ (horizontal bed) to $S = 16\%$ (which corresponds to tests S0 to S4 as it is shown in Figure 5.1). By introducing a slope on the channel lock reach, the volume of denser fluid is reduced. The lock-contraction that follows the introduction of the lock-slope (since the water level is unvaried) corresponds to the volumes that are tested during the first phase, as presented in Chapter 4. The experimental parameters of this group of tests are reported in Table 5.1.

The Acoustic Doppler Velocity Profiler (ADVP) is used to record instantaneous 3D velocities along a vertical, 2.5 m downstream the gate (Figure 5.1). A despiking procedure (Goring and Nikora, 2002) and a low-pass filter applied to the noisy frequencies, after analysis of the power spectra of the raw data, allowed considerable reduction the noise, as explained in Chapter 3.3.3.

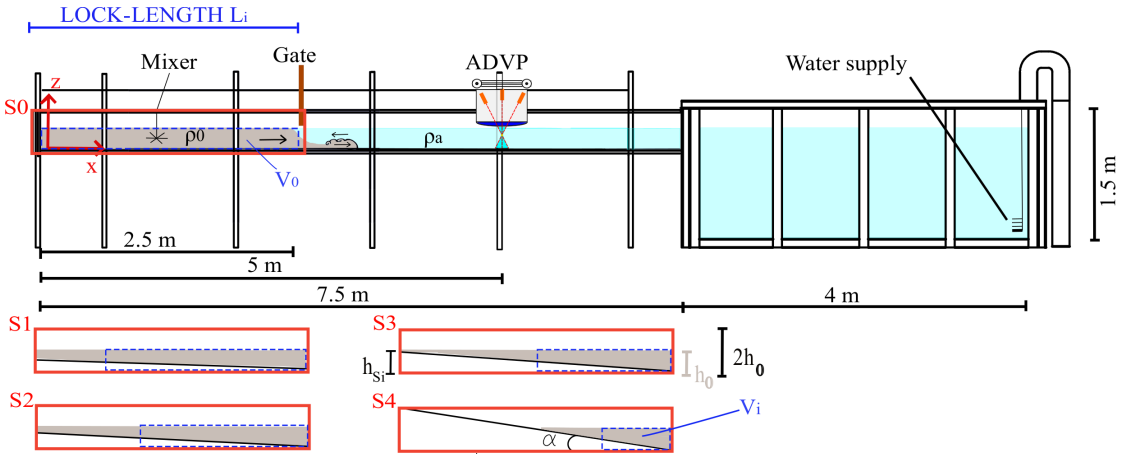

Figure 5.1: Longitudinal view of the experimental set-up showing tested slope configurations S0 to S4 of lock volumes V_i corresponding to tests presented in Chapter 4 with variation of lock-length.

$\mathbf{S}_i$ **Exp.**	ρ_0 (kg/m^3)	g'_0 (m^2/s)	u_0 (m/s)	Re_0 $(-)$	S (%)	α (°)	V_i/V_0 $(-)$	ΔT (°C)
R1.S0	1028	0.29	0.24	48166	0	0.00	1.000	
R1.S1	1028	0.29	0.24	48166	4	2.29	0.750	
R1.S2	1028	0.29	0.24	48166	6	3.43	0.625	≤ 1
R1.S3	1028	0.29	0.24	48166	8	4.57	0.500	
R1.S4	1028	0.29	0.24	48166	16	9.09	0.250	
R2.S0	1038	0.39	0.28	55857	0	0.00	1.000	
R2.S1	1038	0.39	0.28	55857	4	2.29	0.750	
R2.S2	1038	0.39	0.28	55857	6	3.43	0.625	≤ 1
R2.S3	1038	0.39	0.28	55857	8	4.57	0.500	
R2.S4	1038	0.39	0.28	55857	16	9.09	0.250	
R3.S0	1048	0.49	0.31	62610	0	0.00	1.000	
R3.S1	1048	0.49	0.31	62610	4	2.29	0.750	
R3.S2	1048	0.49	0.31	62610	6	3.43	0.625	≤ 1
R3.S3	1048	0.49	0.31	62610	8	4.57	0.500	
R3.S4	1048	0.49	0.31	62610	16	9.09	0.250	

Table 5.1: Experimental parameters. ρ_0 is the initial density of the mixture in the upstream tank (measured with a densimeter), g' is the reduced gravity corresponding to ρ_0, $u_0 = \sqrt{g'h_0}$ is the initial buoyancy velocity with $h_0 = 0.2$ m the total height of the water column, $Re_0 = u_0 h_0/\nu_c$ is the Reynolds number based on initial quantities where ν_c is the kinematic viscosity of the denser fluid, S is the lock-slope expressed in percentage (h_{S_i}/L_0, with h_{S_i} the height as in Figure 5.1) and α is the correspondent angle of inclination of the bottom in the lock, L_i is the length of the upstream lock-reach, V_i/V_0 the percentage of volume of the upstream lock-reach with respect to the configuration L_0, ΔT is the difference in temperature between the temperature of the mixture, T_0, and the temperature of the ambient water, T_a (measured with a thermometer before each experiment).

5.3 Results

5.3.1 The shape of the current

The criterion established in Chapter 4.3.2 is used to identify the two main regions of a gravity current: the head and the body and to analyse the current shape changes due to the presence of the slope in the lock. The kinematic function H, defined in Chapter 4.3.2 as the product of the instantaneous depth averaged streamwise velocity, $u_d(t)$ and the current height, $h(t)$ ($H(t) = u_d(t)h(t)$) is computed in order to identify the extension of the head region. The body length is also analysed by using the cumulative sum of the function H as defined in Chapter 4.3.2. In Figure 5.2 the development of the function H is shown for the tests with the lock-slope. The first prominent minimum of the function allowed the determination of the head region while the body is identified by the extent of the linear portion of the cumulative sum of the function (details in Chapter 4.3.2).

In Figure 5.3 the contours of each test with the lock-slope, identified by the zero streamwise velocity contour, are compared with the correspondent reference test with lock-length variation, as it was analysed in the previous Chapter 4. The results are grouped by the initial density in the lock (columns in the figure), and by pairs of tests with the same volume of the lock but for different slopes. The extension of head and body as identified by the previous methods are also reported with the vertical lines. Dashed lines refers to tests S_i (gravity currents produced by different initial density with the presence of a lock-slope) while continuous lines correspond to L_i tests (with varying initial density and lock-length).

In Figure 5.3 we can see that the head of the current does not show any relevant change. Instead the extension of the body is affected: it reduces with increasing inclination of the bed and the same goes for tests produced by reduced lock volume. A dependency on the initial density is noticed and in three out of the total five slopes lead to the formation of longer body with greater initial buoyancy. This can be verified in Figure 4.5 where extensions of the bodies are traced with the vertical orange lines. R1, R2 and R3 produces progressively longer bodies for tests S0, S1 and S4.

The largest deviation between the two contours of corresponding tests L_i - S_i is noticed for the configuration R_i.L4/R_i.S4, with L4 tests showing a shorter body and a more defined tail while for the correspondent tests with the inclined lock (S4), the body is more extended.

5.3.2 Mean velocity field

In Figure 5.4, the mean streamwise velocity field on the background and velocity vectors of the components ($\overline{u}$, $\overline{w}$) are shown for all the tests performed, with the zero streamwise velocity contours marked by the black lines. We can notice that the structures of the currents are quite similar in all configurations. An elevated head is followed by a zone of high mixing,

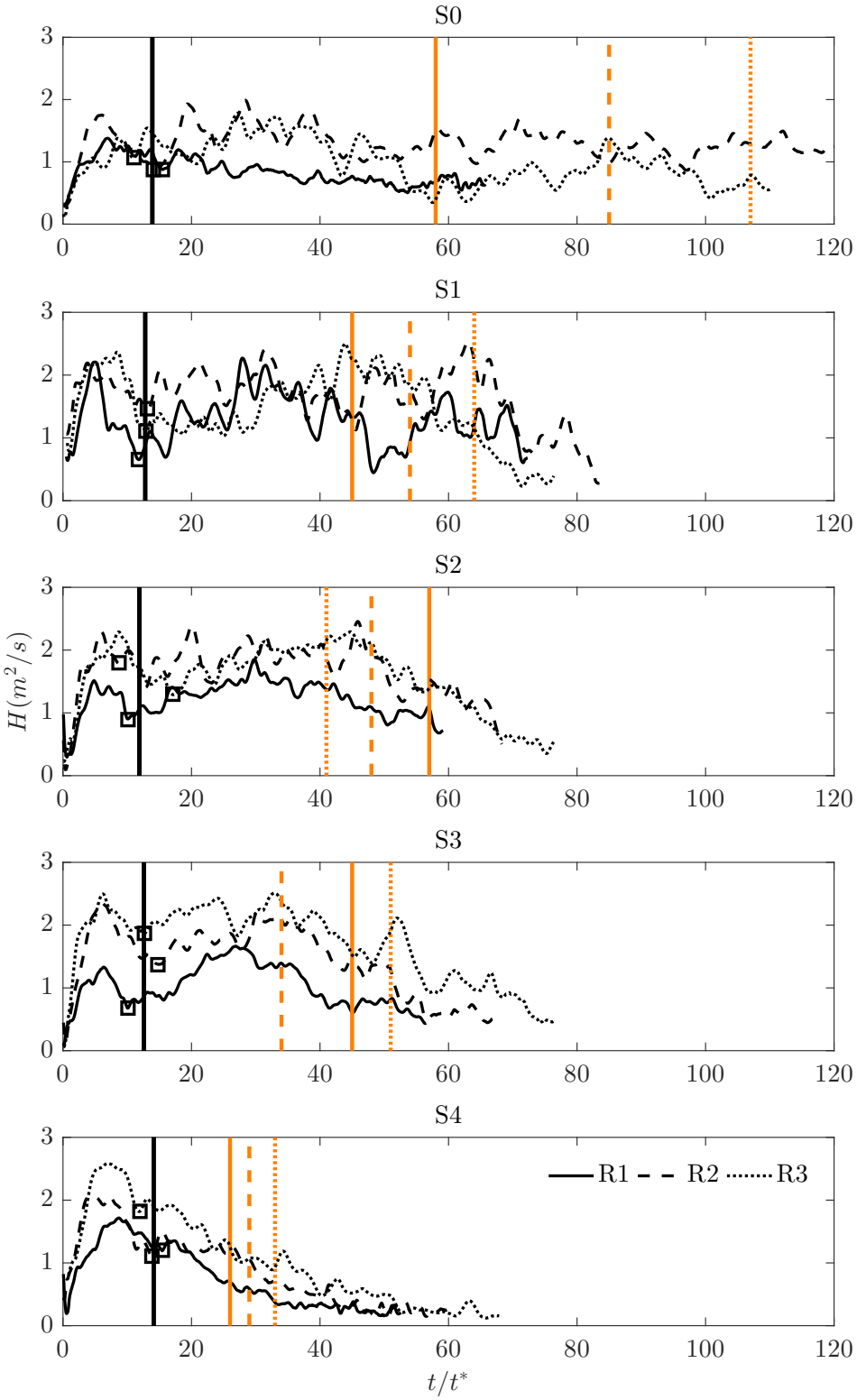

Figure 5.2: Determination of the gravity current head extension from the first prominent minimum of the function H (L_h). The extension of the body (L_b), as identified by the cumulative sum of the depth-averaged streamwise velocity, is also traced with the red vertical lines.

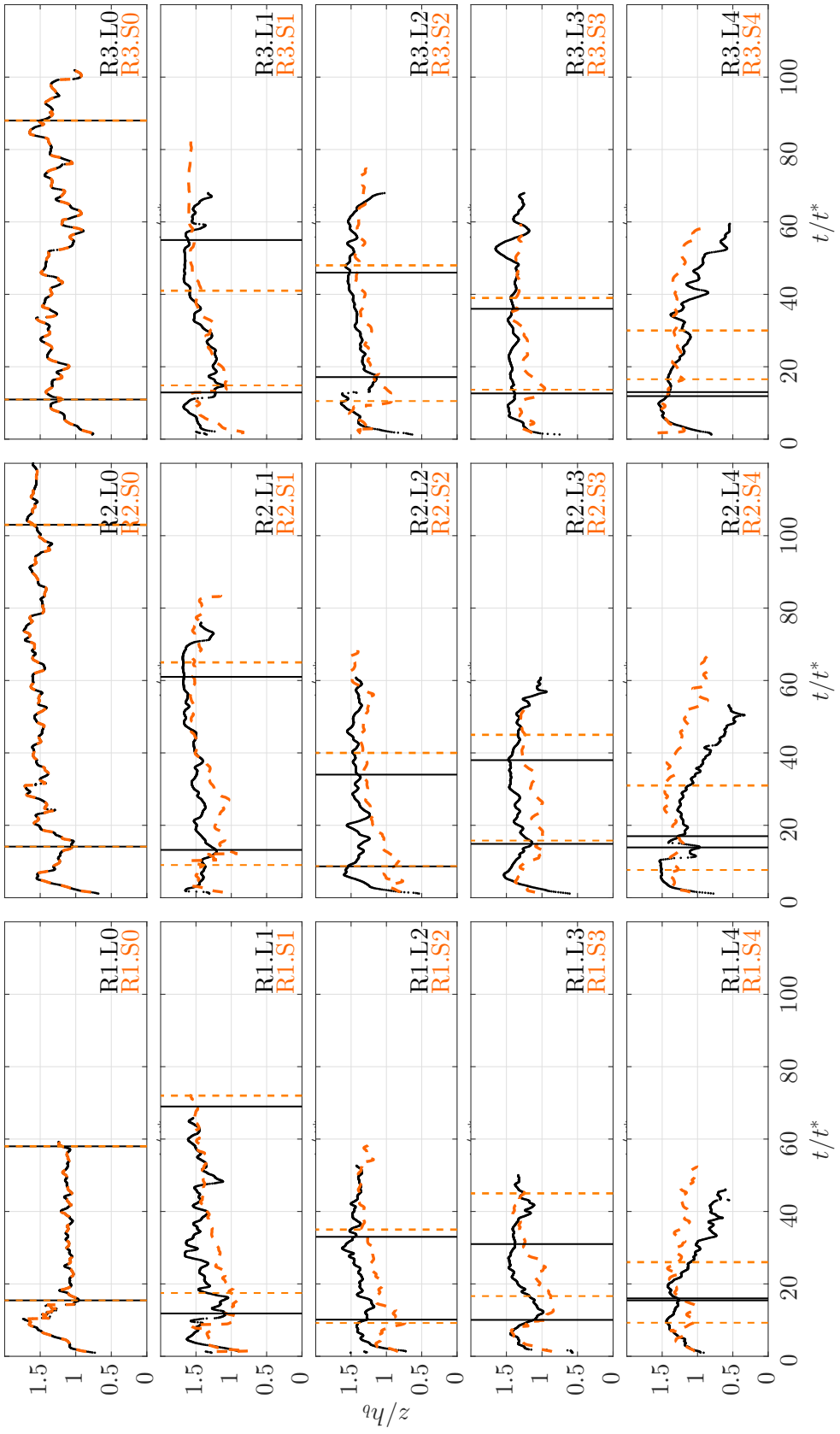

Figure 5.3: Gravity currents contours, as identified by the zero streamwise velocity contour, for tests with the lock-slope and correspondent tests with lock-length variation.

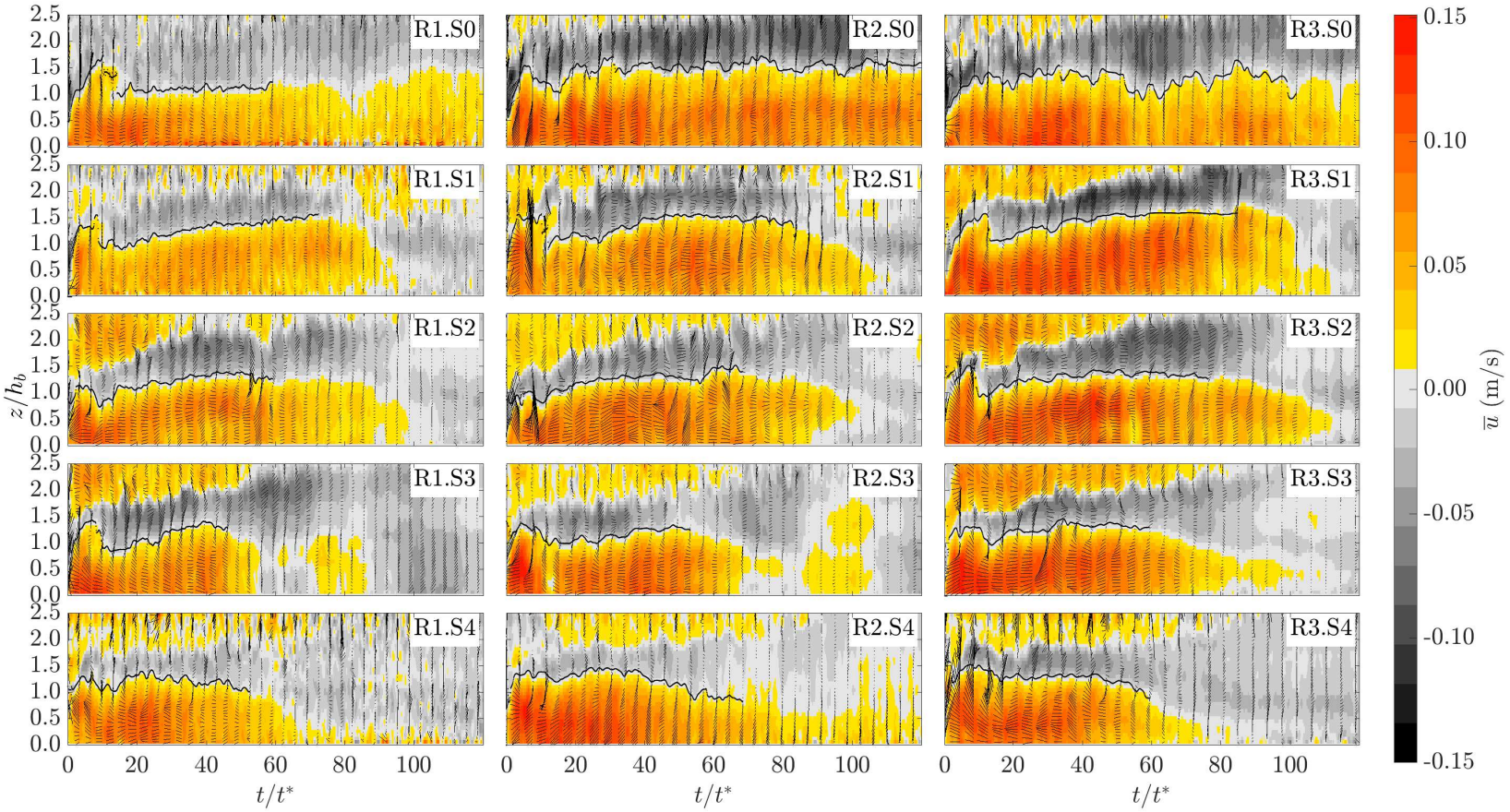

Figure 5.4: Streamwise velocity field on the background and velocity vectors of the components (u,w). The contour of the current is indicated in black.

characterized by the presence of billows (due to Kelvin-Helmholtz type of instabilities (Simpson, 1972)) that are due to shear at the rear part of the elevated head. Body and tail are not always well defined regions, mainly for the class of tests down an incline, and therefore the contour is not drawn. Tests S_i show slightly lower values of streamwise velocities with respect to correspondent L_i tests (Figure 4.3). Configuration S4 is the exception and an inversion of this tendency is noticed.

The fact that in general mean streamwise velocity is decreased for tests with a lock-slope can appear to some extent contradictory but this behaviour has already been mentioned in literature, in the study of Beghin et al. (1981). They were among of the first to investigate the role of the slope on the physics of a gravity current and showed that tests with flows on small slopes experience firstly an acceleration phase, followed by a deceleration phase. This is because of the fact that, although the gravitational energy increases as the lock-slope becomes more vertical, there is also increased entrainment, both into the head itself and into the flow behind. This produces an extra dilution of the current with a decrease in buoyancy.

5.3.3 Bed and interfacial shear stresses

Bed shear stress evolution is affected by the changing initial conditions of the current and this may explain how the entrainment capacity of a current is altered. Bed shear stress temporal evolution is therefore calculated by following the procedure in Appendix A. Thus, the fitting of the logarithmic law of the wall is used to calculate the friction velocity and bed shear stress is afterwards computed as $\tau_b = \rho_c u_*^2$ by considering a constant initial density that is here equal to the initial density in the lock (ρ_c). The bed shear stress time-evolution of gravity currents with lock-slope ($\tau_{b,S}$) are compared to the analogous results for tests with decreasing lock ($\tau_{b,L}$) in Figure 5.5. Tests performed on an inclined bottom show in general lower values of bed shear stress with the only exception of tests S4, which is the steepest slope condition, where, from normalized time $t/t^* \simeq 20$, i.e. in the body region, bed shear stress is slightly higher than in the correspondent L_i tests.

At the upper boundary of the gravity currents, i.e. the interface with the ambient water, using the same fitting procedure, as explained in Chapter 4.3.4, the estimation of an interface shear stress (τ_m) is made. The time evolution of interface shear stress is therefore computed and shown in Figure 5.6, following the same procedure as for the bottom shear stress. Again the main differences between tests with reduced lock and respective tests with lock-slope are for the fourth configuration: the steepest slopes present higher values of interface shear stress in the body region with respect to the correspondent tests with the same initial volume of release but flowing on a horizontal bed.

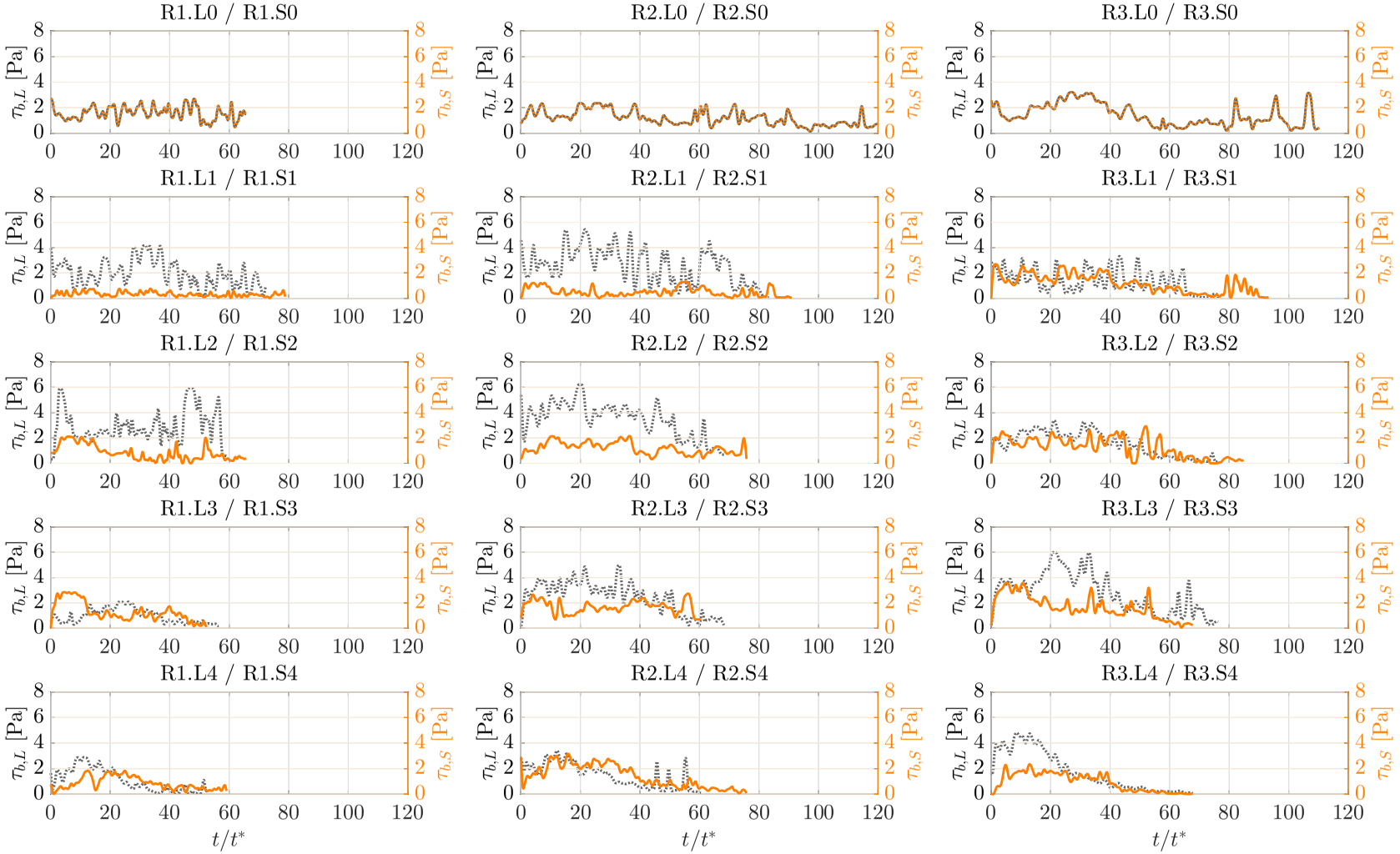

Figure 5.5: Temporal evolution of bed shear stresses calculated by log law fitting for tests with progressively reduced lock-length ($\tau_{b,L}$) and with the lock-slope ($\tau_{b,S}$).

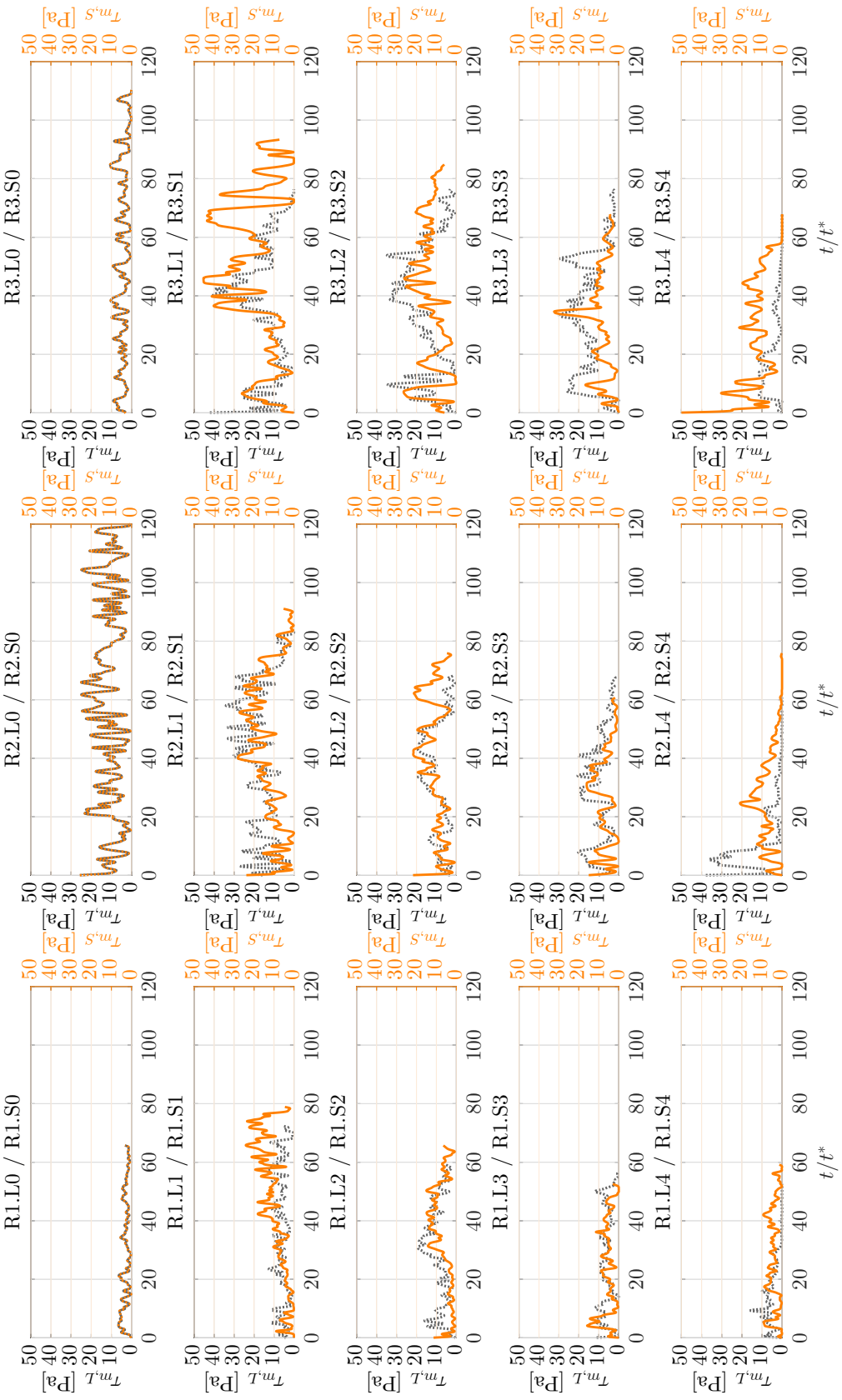

Figure 5.6: Temporal evolution of interfacial shear stresses calculated by log law fitting for tests with progressively reduced lock-length ($\tau_{m,L}$) and with the lock-slope ($\tau_{m,S}$).

5.4 Discussion

5.4.1 Shape variation of gravity current with the lock-slope

The extent of the body of correspondent tests performed with the lock-slope or on horizontal bed with varying lock-lengths are compared in Figure 5.7. For lower slopes the body extension is similar to the currents produced with the same lock-volume but with horizontal bottom. However, for slopes higher than 6%, the body region for tests S_i are longer than correspondent tests L_i. This behaviour agrees with the study of Britter and Linden (1980) and Dai (2013) where they indicated that a critical angle exists over which buoyancy force is large enough to counteract the bottom friction and produce a steady flow. At this point two mechanisms affect the evolution of the current: the current entrains water from the upper surface due to the increment of friction and the head is fed by the rear steady current. The flow of tests S4 show these characteristics: (i) an extended body is the result of water entrainment at the upper surface of the current that creates dilution and expansion of the fluid in the current; (ii) the fluid in the body become faster as a result of the gravitational energy as in Britter and Linden (1980) (Figure 5.4). Britter and Linden (1980) showed that, while with currents flowing along a horizontal boundary, the head is the controlling feature down a slope, the body becoming more determinant in the gravity current evolution since it is up to 30-40% faster than the head velocity, depending on the slope, being able therefore to move faster material into the head. In this study, this is verified only for lock-slopes of 16% (tests S4).

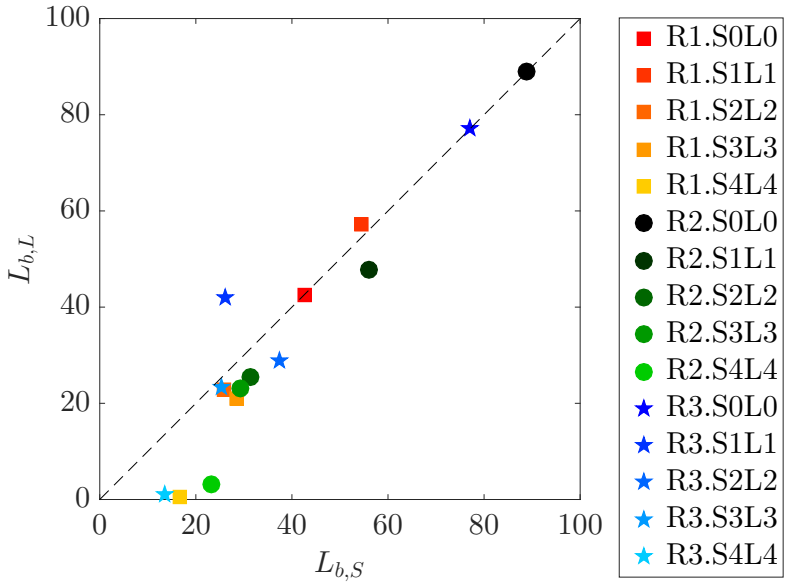

Figure 5.7: Comparison of the length of the body (L_b) between tests with progressively reduced lock-length and with lock-slope. The dashed line is the identity line.

5.4.2 Ambient entrainment and bottom erosion capacity

The validity of the use of Φ_m (as defined in Chapter 4.3.5) as an indicator of the entrainment capacity is supported by the analysis of its relation with the Richardson number Ri as shown in Chapter 4.4. The relation between water entrainment and bulk Richardson number is well known in literature and numerous empirical fits to the experimental data have been proposed since the early work of Parker et al. (1987) and supported by more recent contributions (Stagnaro and Pittaluga, 2014). Therefore, it is here proposed to use this quantity as a surrogate for water entrainment capacity since it benefits from the instantaneous measurements of shear stress and therefore account for the unsteady behaviour of the gravity currents. In Figure 5.8, the potential water entrainments for gravity currents performed on an inclined and correspondent tests with reduced initial volume of release are compared. The tests S4L4 deviate from the identity line, thus a greater water entrainment is expected for the case with the inclined bed with respect to the horizontal bottom.

The bottom erosion capacity is compared for gravity currents performed with the lock-slope and correspondent tests on a horizontal bottom and this is shown in Figure 5.9. Generally L_i tests show a higher erosion capacity with respect to their analogous S_i. The presence of extra gravitational energy is proved not to play a role in enhancing bottom erosion which is contrarily reduced. This is probably a consequence of the decrease in streamwise velocity which results from the dilution of the gravity current. But, on the other hand, ambient water entrainment causes the expansion of the body region. Longer bodies keep eroding material longer and the erosion potential attributed to this part is therefore increasing.

The potential bottom erosion, i.e. the quantity Φ_b in Figure 5.10, decreases with increasing slope. The potential energy ascribed to the gravity currents has been computed as

$$E_p = \rho_i V_i g h_b \tag{5.1}$$

and it is shown in Figure 5.11. It confirms that tests with increasing lock-slope have a reduced potential energy as a consequence of the volume reduction and this latter is the driving element. The initial density has in fact a smaller influence as shown in Figure 5.10, right side.

The role of the body in the total erosion capacity is computed as the ratio Φ_{b-body}/Φ_b (Figure 5.10) whose limits of integration of Φ_{b-body} are $T_1 = L_h$ and $T_2 = L_b$. The contribution that is ascribed to the body has a similar development as the total erosion capacity. This enforce the hypothesis that the body is determinant in the entrainment capacity of a gravity current. Figure 5.10 highlights that the importance of the body in the total erosion capacity becomes proportionally higher for tests S4 (the trend lines in Figure 5.10 deviates more in this configuration). Higher water entrainment was proved in Section 5.4.2 for this latter case, which was therefore subjected to an expansion of the body region. An influence of the upper surface on the dynamics of the lower bottom boundary is therefore hypothesized. The interaction between the upper layer and the bottom was already pointed out by the numerical investigation of Cantero et al. (2008) and experimental evidences are reported in Chapter 4.3.3 where the

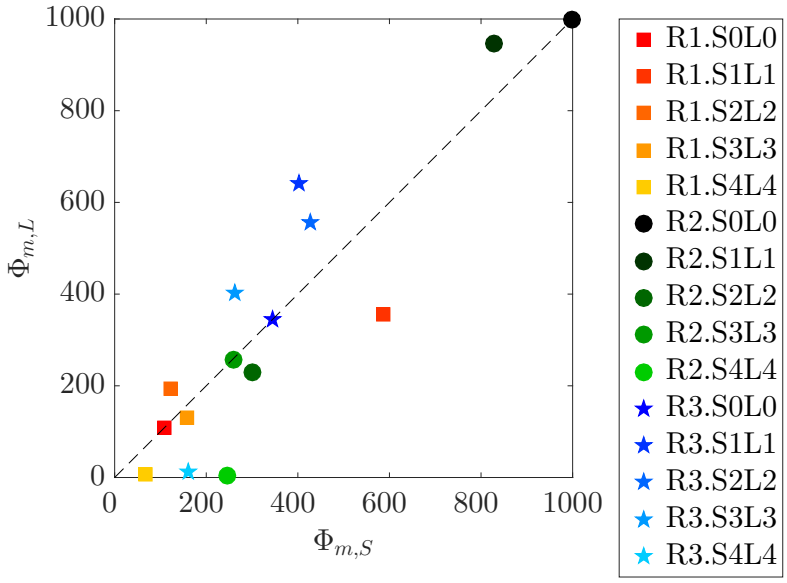

Figure 5.8: Comparison of Φ_m, a surrogate for the entrainment capacity of the mixing region, between tests with lock-slope (S_i) and correspondent tests on horizontal bottom (L_i). The dashed line is the identity line.

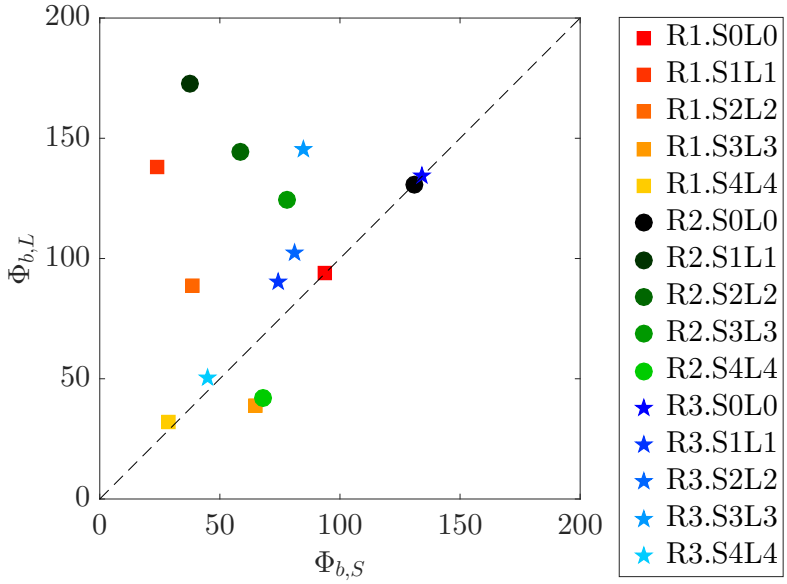

Figure 5.9: Comparison of the bottom erosion capacity Φ_b between tests with lock-slope (S_i) and correspondent tests on horizontal bottom (L_i). The dashed line is the identity line.

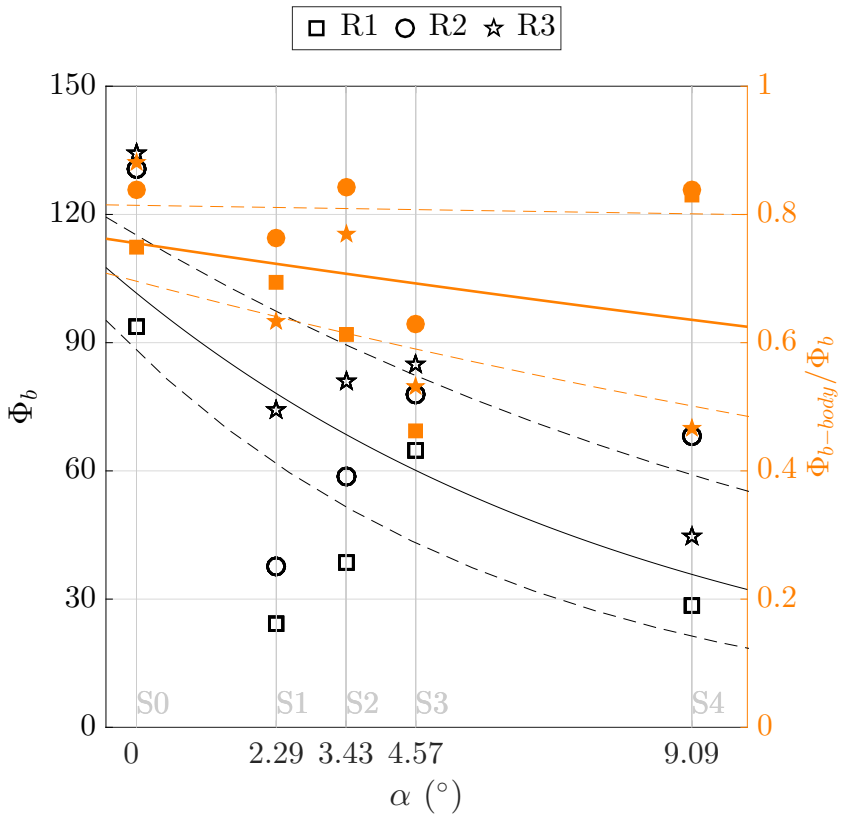

Figure 5.10: Potential erosion capacity for gravity currents (left axis) developed with different lock-inclinations (α) and rate of potential bottom erosion due to the body of the gravity current on the total bottom erosion capacity, Φ_{b-body}/Φ_b, (right axis). The exponential fitting lines are reported in order to give evidence of the general trend, together with the 65% confidence intervals (dashed lines).

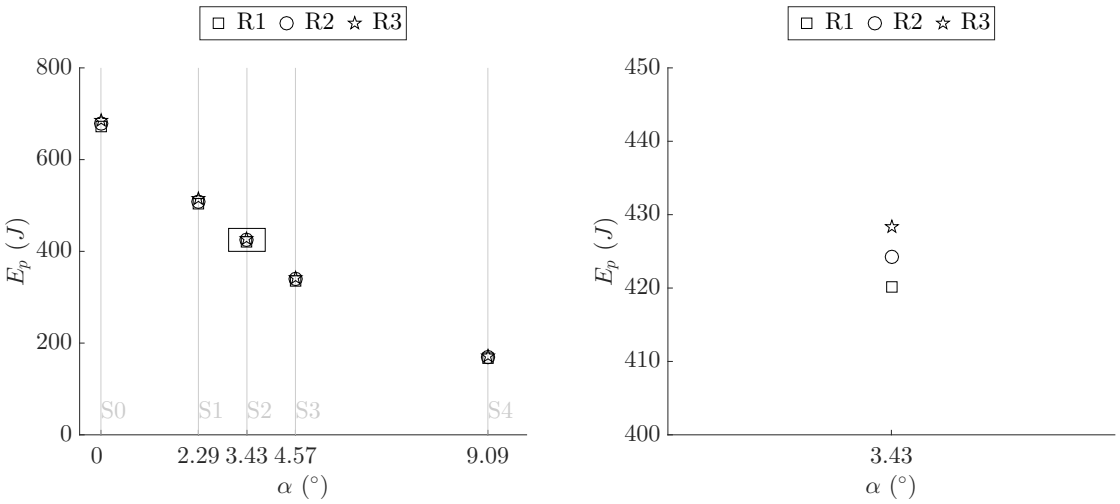

Figure 5.11: Left side, potential energy (E_p) of tests conducted under different lock inclinations (α). Right side, a zoom on S2 tests.

vorticity is analysed showing that residual negative vorticity expands from the upper layer through the bottom with progressively lower intensity.

5.5 Conclusions

In this Chapter the effect of incremental gravitational energy is tested by reproducing experimentally gravity currents of different initial densities with the presence of inclined locks. Corresponding tests with a horizontal bottom and reduced volumes are performed as well and it allows to have the reference cases showing the only effect of the volume constriction. The range of lock-slopes tested varies from horizontal bed to $S = 16\%$. Gravitational energy, which is an extra potential energy imparted to the fluid due to the raised position of the center of mass, is the main driving and directly depends on the slope (Khavasi et al., 2012). This competes with the entrainment that takes place due to the higher shear stress at the upper interface and tend to dilute the current. Thus if on one hand extra potential energy drives for a faster gravity current, on the other hand water entrainment at the upper interface dilute the fluid of the current which is consequently slowed down and it expands due to incorporation of the ambient fluid.

The configurations S4-L4, corresponding to the steepest lock-slope and the shortest lock-length, respectively, exhibit the highest deviations between tests with lock-slopes with respect to correspondent tests on the horizontal bed. S4 tests showed a longer body, owing to entrainment of the ambient fluid. The body is fast, likely accelerated due to gravitational effects. Bottom erosion capacity generally results reduced by the presence of extra gravitational energy most probably due to lower streamwise velocities which followed gravity currents dilution.

6 Gravity currents flowing over mobile bed

Chapter 6 is based on the scientific articles "Entrainment, transport and deposition of sediment by saline gravity currents" by J. Zordan, C. Juez, A.J. Schleiss and M.J. Franca submitted in Advances in Water Resources and "Experimental results on sediment entrainment by gravity currents" by J. Zordan, C. Juez, A.J. Schleiss and M.J. Franca published in Book of abstracts of IAHR 2017 conference, Kuala-Lumpur, Malaysia. The experimental work and the analysis presented hereafter is original and was performed by the author.

6.1 Introduction

The highly turbulent dynamics of density-driven flows are still not completely understood and their mechanism coupled with the presence of a mobile bed little investigated.

Therefore, in this group of tests different particle sizes and initial densities are tested, using the lock exchange experiments with a large volume of release. We focus on the description of the role of turbulent gravity flows on processes of sediment erosion, transport and deposition. The main goal is to characterize the major forces acting on the particles at the bed and to isolate and assess their role in the entrainment of sediments due to the passage of these currents. Instantaneous velocities collected over a vertical profile, video analysis and topography surveys are used for this purpose.

The objective is to determine the forces responsible for the picking up of sediments, i.e the mechanism responsible for the sediment removal from the mobile bed and displacement within the current flow. Then we consider the capacity of the current to move downstream the sediment entrained, i.e. the distal transport of the grains. The cross-analysis of the velocity data, video analysis and topography survey allow analysis of the influence of grain size and of the near-boundary mean flow-velocity distribution on the force acting for sediment distal transport. Furthermore, erosion and deposition patterns are analysed through the topography and photo surveys.

6.2 Methods

On the main channel as described in Section 3.2.1, at the bed, that is kept horizontal and smooth, an erodible bed reach is added 2.5 m downstream from the gate. A schematic representation of the installation is in Figure 6.1. A 1 cm deep depression on the flat bed, is filled with the polyurethane artificial fine sediments (details in Appendix C). This erodible section has the same width as the channel and a longitudinal extent of 0.6 m. The gravity current, while passing above the erodible reach, erodes and entrains the sediments that are then deposited downstream as it is shown in the sketch of Figure 6.3.

In Figure 6.1 the measurement instrumentation is also shown. The Acoustic Doppler Velocity Profiler (ADVP, see Appendix B) is placed directly upstream of the erodible bed and it records 3D instantaneous velocity profiles during the passage of the gravity current. The high-speed camera (see Chapter 3.3.5) records the evolution of the gravity current over the erodible bed laterally through the glass walls of the channel. The point laser (see Chapter 3.3.4) is used to measure the topography, after the passage of the gravity current, over the mobile bed reach and at the downstream part of channel, recording eight longitudinal sections, covering the mobile bed reach, and eight cross-sections in the downstream zone. Finally, pictures of the downstream reach, where deposition occurs, are taken from the top, after the passage of the gravity currents.

Three initial densities in the lock were tested combined with three sizes of sediment composing the erodible bed. The experiments were prepared by firstly filling the channel with ambient water reaching a water depth of h_0=0.2 m. The surface with the erodible bed was isolated up and downstream with two planks. The sediments were wetted and injected, the mixture was stirred. Once the fluid came to rest, the sediments settled into an homogeneous flat bed of one centimetre depth (Figure 6.2).

The material composing the erodible bed was chosen in order to have a settling velocity that follows the similarity criteria as described in Chapter 2.6. Field-scale gravity currents generally have velocities in the range of 1-10 m/s (Kneller and Buckee, 2000), whereas laboratory flows have velocities which are two order of magnitude smaller than in the field. The settling velocity should thus be reduced in the model by a factor of 10 to 100. Due to scale effects as discussed in Chapter 2.6, to maintain a velocity scale ratio of approximately 10 between the prototype and the model and to avoid sediment that is too fine, a reduced density for the sediments used in the model is required. Therefore, plastic sediments have been chosen. The material is a high-performance thermoplastic polyurethane (TPU) with a density of 1160 kg/m^3 (an application with this same material can be found in Chamoun et al. (2016b)). Three different grain sizes were used, and the D_{50} and D_{90} are shown in Table 6.1. The mean diameter of the particles is chosen to be within the range of non-cohesive fine sediment, 62-500 μm, according to Van Rijn (2007). The artificial nature of these sediments was preferred to natural clay–silty material to avoid algae and biofilm growth. More details on the material are given in Appendix C.

The main parameters of the conducted tests are summarized in Table 6.1.

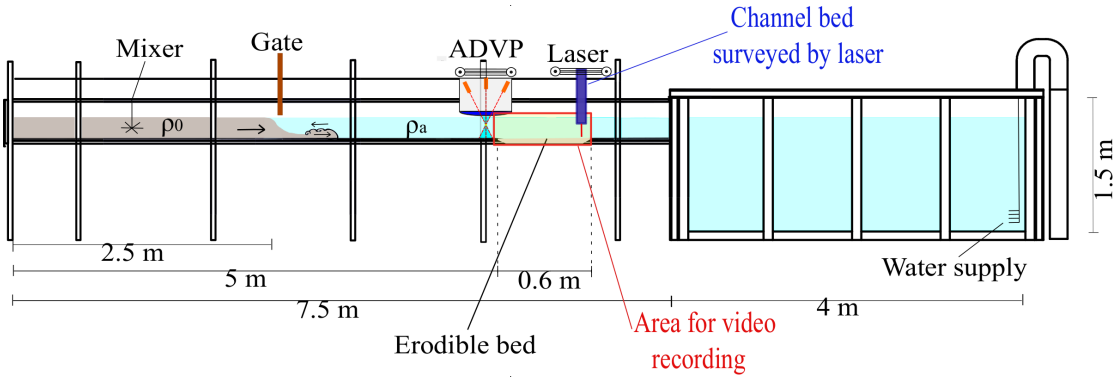

Figure 6.1: Side view and cross section of the experimental set-up.

Exp.	ρ_0 (kg/m^3)	g' (m^2/s)	u_f (m/s)	Re_0 $(-)$	Re_D $(-)$	Fr_D $(-)$	D_{50} (μm)	D_{90} (μm)	ΔT $(^\circ C)$
R1.fine	1028	0.29	0.101	48152	6727	0.726	81	145	
R1.medium	1028	0.29	0.106	48152	7080	0.764	145	217	≤ 1
R1.coarse	1028	0.29	0.126	48152	8420	0.909	191	268	
R2.fine	1038	0.39	0.117	55719	7820	0.729	81	145	
R2.medium	1038	0.39	0.134	55719	8907	0.831	145	217	≤ 1
R2.coarse	1038	0.39	0.127	55719	8480	0.791	191	268	
R3.fine	1048	0.49	0.131	62374	8747	0.729	81	145	
R3.medium	1048	0.49	0.142	62374	9433	0.786	145	217	≤ 1
R3.coarse	1048	0.49	0.155	62374	10347	0.862	191	268	

Table 6.1: Experimental parameters. ρ_0 is the initial density of the mixture in the upstream tank (measured with a densimeter), g' is the reduced gravity corresponding to ρ_0, u_f is the velocity of propagation of the front of the current calculated from video analysis, $Re_0 = u_0 h_0/\nu_c$ is the Reynolds number based on initial quantities with $u_0 = \sqrt{g' h_0}$ the initial buoyancy velocity, h_0 the total height of the water column and ν_c the kinematic viscosity of the denser fluid, $Re_D = u_f h_b/\nu_c$ is the densimetric Reynolds number based on bulk quantities with h_b is the bulk height of the current, here considered as one third of the total water depth, $Fr_D = u_f/\sqrt{g' h_b}$ is the densimetric Froude number, D_{50} and D_{90} are the characteristic grain sizes of the mobile bed and ΔT is the difference in temperature between the temperature of the mixture, T_0, and the temperature of the ambient water, T_a (measured with a thermometer before each experiment).

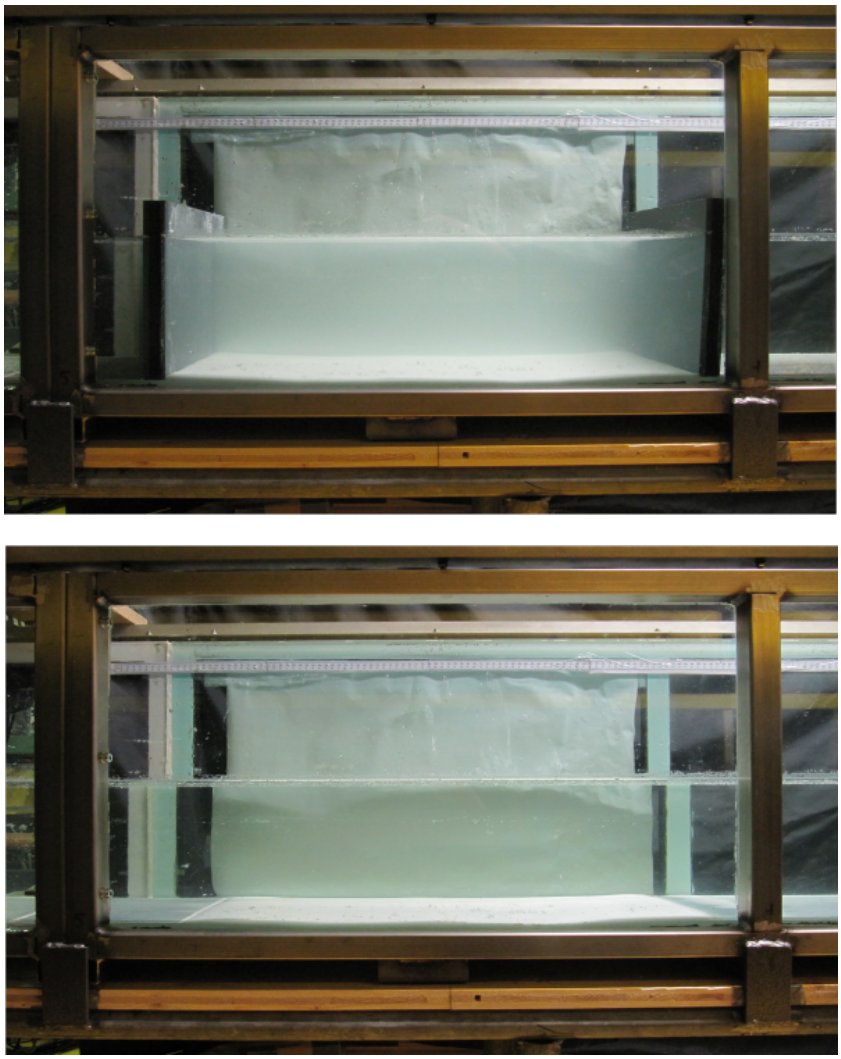

Figure 6.2: Mobile bed deposition.

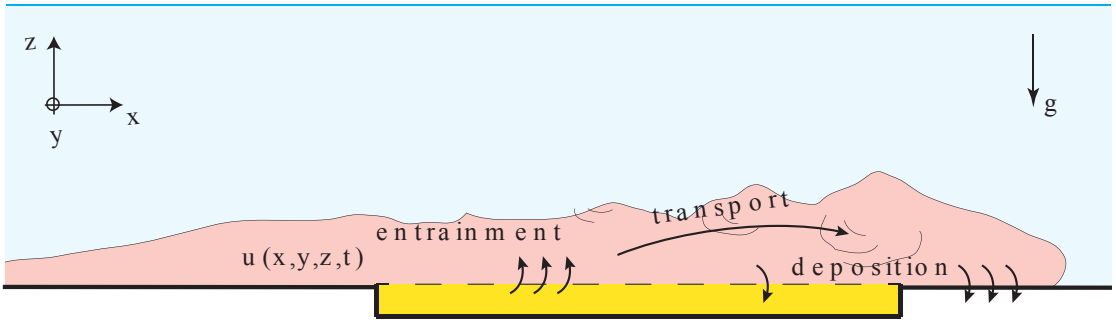

Figure 6.3: Sketch of a bottom gravity current flowing on the erodible reach. Entrainment of material from the bottom takes place. This is transported within the gravity current and deposited downstream (Franca, 2017).

6.3 Flow description

6.3.1 Head region

The kinematic function H, as defined in Chapter 4.3.2, is computed and shown in Figure 6.4. The square symbols identify the first meaningful local minimum of H, and the vertical lines represent the average positions of the head amplitude in time (L_h) considering the tests grouped by same initial density in the lock. As pointed out in Chapter 4.3.2, in Figure 6.4 it is confirmed that the initial density of the current does not have an influence on the length of the head L_h.

6.3.2 Mean flow

Time series of the mean streamwise velocity profiles are shown in Figure 6.5a, where the contour of the currents is marked with the black line. The maximum velocity in the head region is observed at one third of the current height, as was also observed in the literature for a smooth bed (Sequeiros et al., 2010b). From Figure 6.5, we observe the following: the head is a well-defined region, and it is characterized by a core of high streamwise velocity; the head is higher than the following body; a billow extends on the upper part of the head, at the interface with the ambient water, in a zone of high mixing; the length of the body is limited, and it fades into a final zone, the tail of the current, in which a weak streamwise velocity persists near the lower boundary. As expected, increasing the initial gravity current density results in larger streamwise velocities.

The highest streamwise velocity is at the core of the current in the head, not near the front but rather under the region of intense vortex generation. While the current advances, a return flow forms on the upper ambient fluid layer. This counter-current shows a jet-like configuration that is more defined for higher gravity current velocities. There is a time scale for the complete formation of the return flow which is dependent on the initial density in the lock and on the inertia of the physical system composed by the experimental channel and the large downstream reservoir. In fact, the counter current forms due to the displacement of mass caused by the density current whose front is travelling faster for higher initial densities and forces the ambient water, to move in the opposite direction.

Results for the mean vertical velocity are shown in Figure 6.5b. An upward flow at the front of the advancing current is present. This flow is then incorporated by the counter current flowing above the heavier current. From the bottom of the current to the water surface, the vertical velocity presents oscillations of positive and negative values.

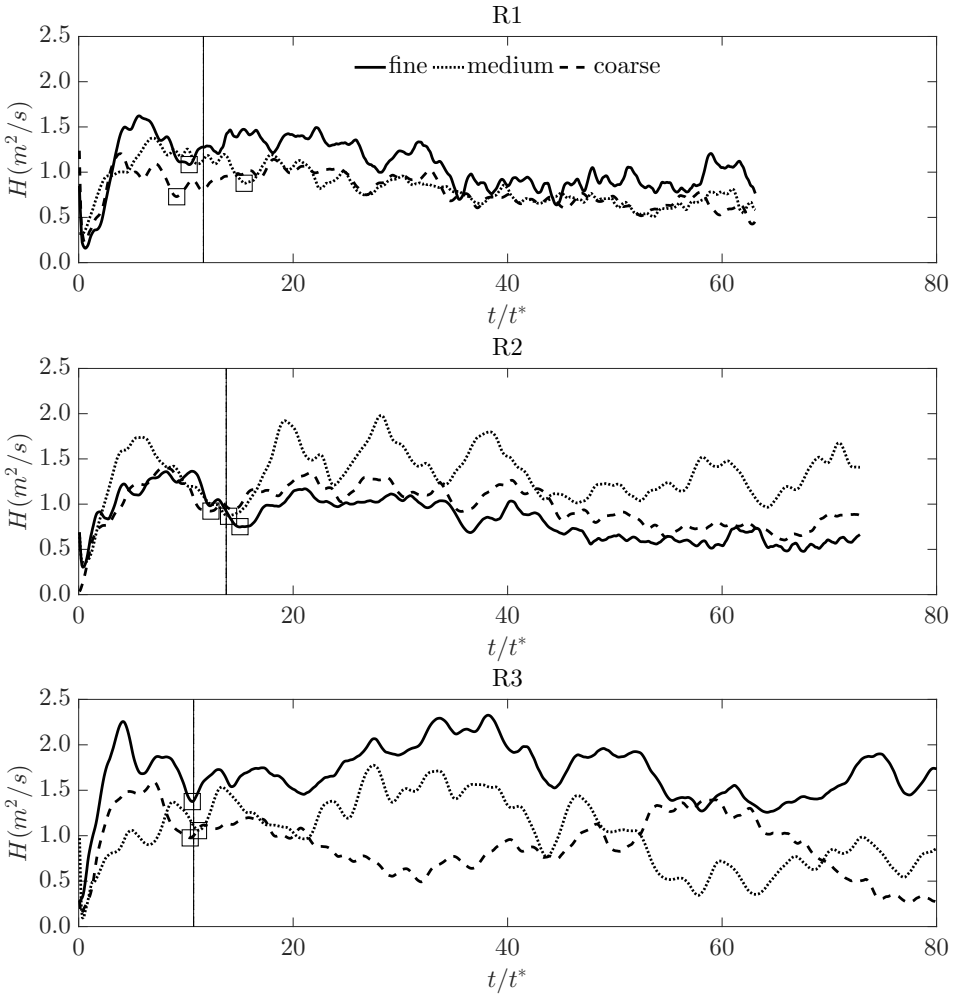

Figure 6.4: Evolution of kinematic function $H(t) = u_d(t)h(t)$ for the nine experiments performed grouped by same initial density in the lock (R1=1028 kg/m^3; R2=1038 kg/m^3; R3=1048 kg/m^3). The square symbols identify the first prominent minimum for each test. The vertical line is the average head length (L_h) considering the tests grouped by the same initial density. The results correspond to the tests with mobile bed made of fine, medium and coarse sediments, as identified in the legend.

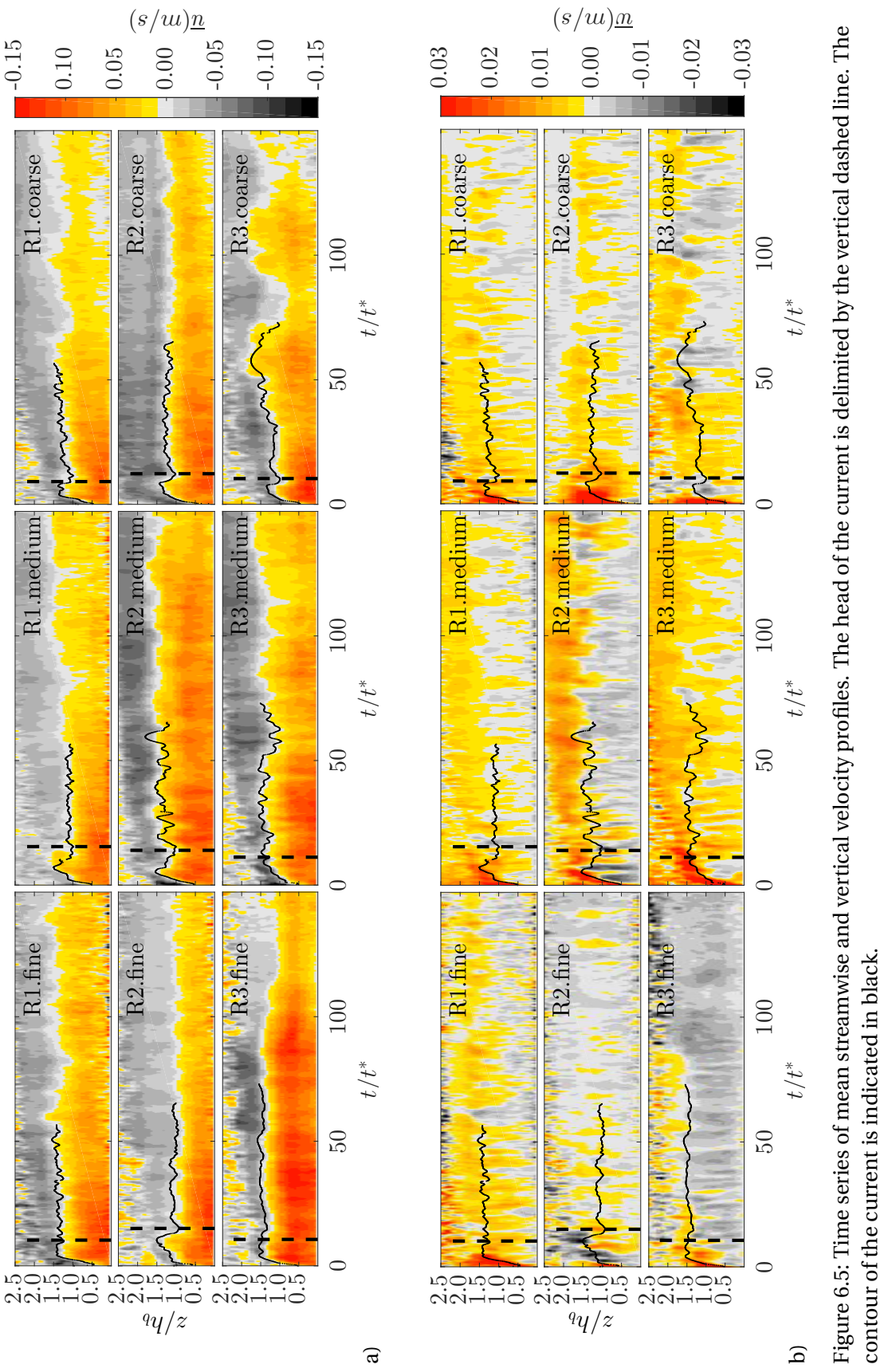

Figure 6.5: Time series of mean streamwise and vertical velocity profiles. The head of the current is delimited by the vertical dashed line. The contour of the current is indicated in black.

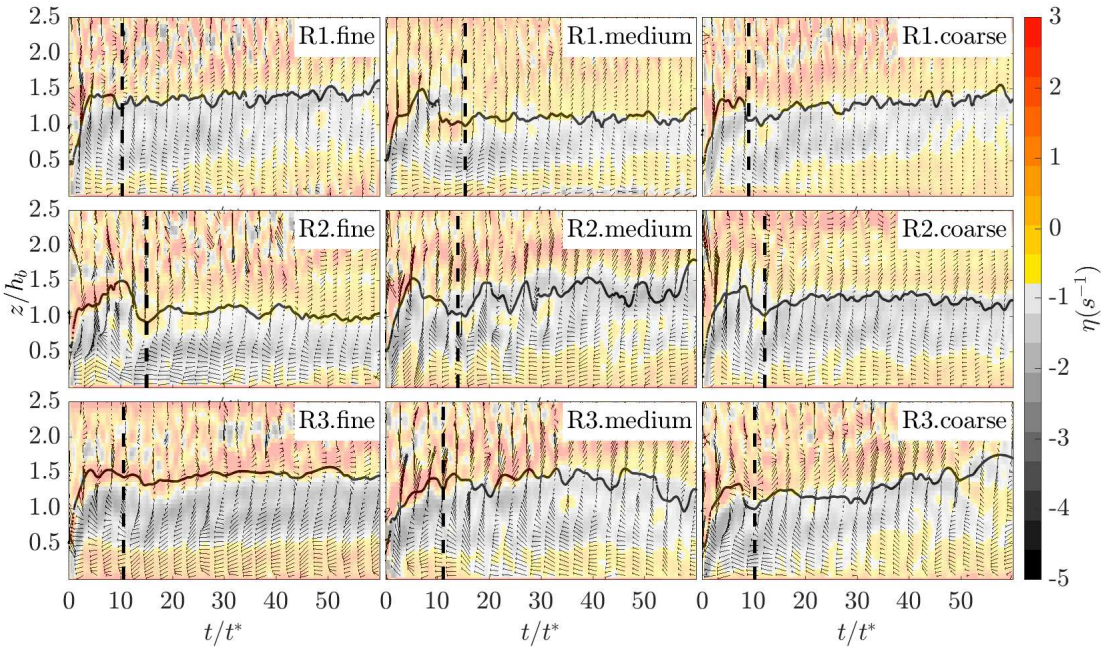

Figure 6.6: Spanwise vorticity field $\eta_y(s^{-1})$ on the background and velocity vectors of the components (u,w). The head of the current is delimited by the vertical dashed line. The contour of the current is indicated in black.

Figure 6.6 displays the spanwise vorticity field (computed using Equations 4.3, 4.4 and 4.5) as well as the velocity vectors. The outline of the currents and the head extent are also highlighted.

The vorticity field in Figure 6.6 follows the same structure that was defined in Chapter 4.3.3. A region of negative vorticity at the interface between current and ambient fluid, which is the result of the shear between the current and the counter-current, is present. Negative values of vorticity indicate clockwise rotation of the vortical structures that are also present in the mean flow as confirmed by looking at the recirculation cells reproduced by the velocity vectors in Figure 6.6. Vortical movements of eddies, identified as Kelvin-Helmholtz instabilities, are present at the interface between the dense and light fluids, and they are eventually dissipated towards the tail of the current. Furthermore, positive vorticity of comparable magnitude are observed near the bed as the result of the shear between gravity current flow and the bed.

The normalized time series of the streamwise and vertical depth-averaged velocities (w_d, computed in the same way as u_d, Equation 4.2) are shown in Figure 6.7. A normalization is performed dividing w_d by the buoyancy velocity (u_b). In this figure, the grey lines are the instantaneous depth-averaged velocities per each test performed for fine, medium and coarse material. The instantaneous depth-averaged velocities ($<u_d>$ and $<w_d>$), which are averaged among tests grouped by the same initial density are shown with the orange line. Tests that

present the same initial densities generally group well, and they exhibit a similar evolution.

The depth-averaged streamwise velocities show a peak in the head region, which is delimited by the dashed vertical black line. Moreover, a first local minimum of depth-averaged velocity is visible, indicating a zone behind the head, where the streamwise velocity is particularly low.

The body is characterized by a plateau, indicating the quasi-steady behaviour of this region, which is observed immediately after the head, followed by the tail with a decrease in the streamwise depth-averaged velocity.

The arrival of the head causes an upward surge of the ambient fluid, which is visible in the vertical velocity signal. Thereafter, smaller amplitude oscillations are observed.

The temporal series of the normalized mean streamwise and vertical velocities, corresponding to test R2.medium, are shown in Figure 6.8 for five vertical positions between z=8 and 106 mm. At z=106 mm, the streamwise velocity is negative because at this position, the counter current is dominant. The vertical velocity is higher at the front: the fluid in this region mainly moves upward, as previously observed in Figure 6.7. At z=72 mm, the streamwise and vertical velocities oscillated between negative and positive values. This location is roughly the interface between the gravity current and the ambient fluid, where most of the mixing processes occur and the exchange between current and ambient fluid is maximum.

The highest streamwise velocities are found near the channel bed, at z=20 and 8 mm. At these heights, the streamwise velocity is positive since the advancing gravity current is detected.

During the first instants of the experiments, at z=20 mm and z=44 mm, it is observed how the ambient fluid flows backward over the head of the current. While travelling, the current displaces ambient fluid upward at the front; thus, in Figure 6.8, the first instants show a peak in positive vertical velocity. Then, the vertical velocity becomes negative, and further in the body, coherent peaks along the entire vertical of the current are presented, and these upward and backward displacements of fluid continue.

Time series of mean vertical velocities are shown in Figure 6.9 for three different positions along the vertical for all tests in order to highlight his oscillating nature. These vertical oscillations are linked with coherent motions along the vertical of the flow, which may enhance vertical mixing. The presence of negative vertical velocities is also observed and alternatively. The two movements - upwards and downwards - result in a well-defined periodic sequence of events. The fluctuations are consistent along the entire vertical profile of the current.

6.3.3 Turbulent quantities and bed shear stress

Turbulent velocity scales are calculated as the root mean square of the fluctuating component of the velocities with respect to the mean velocity as explained in Chapter 3.3.3. In Figure 6.10, the temporal evolutions of $\overline{u}$, u'_{RMS} and w'_{RMS} are shown for test R1.fine at z=16 mm

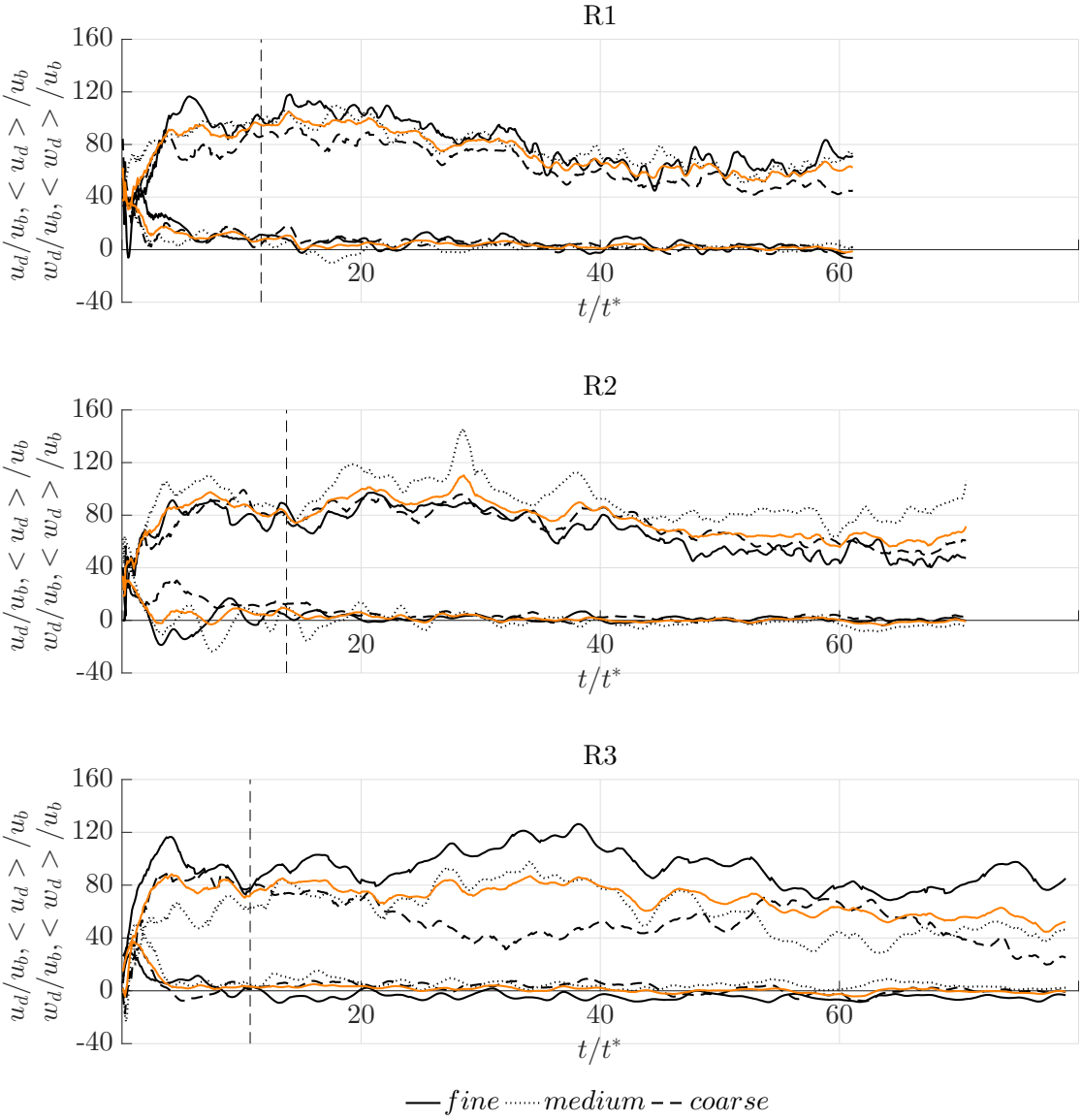

Figure 6.7: Time series of depth averaged streamwise and vertical velocities for tests grouped by same initial densities. The orange lines are the averaged time series of depth-averaged velocities. The vertical dashed line represents the average limit of the head L_h. The results correspond to the tests with mobile bed made of fine, medium and coarse sediments, as identified in the legend.

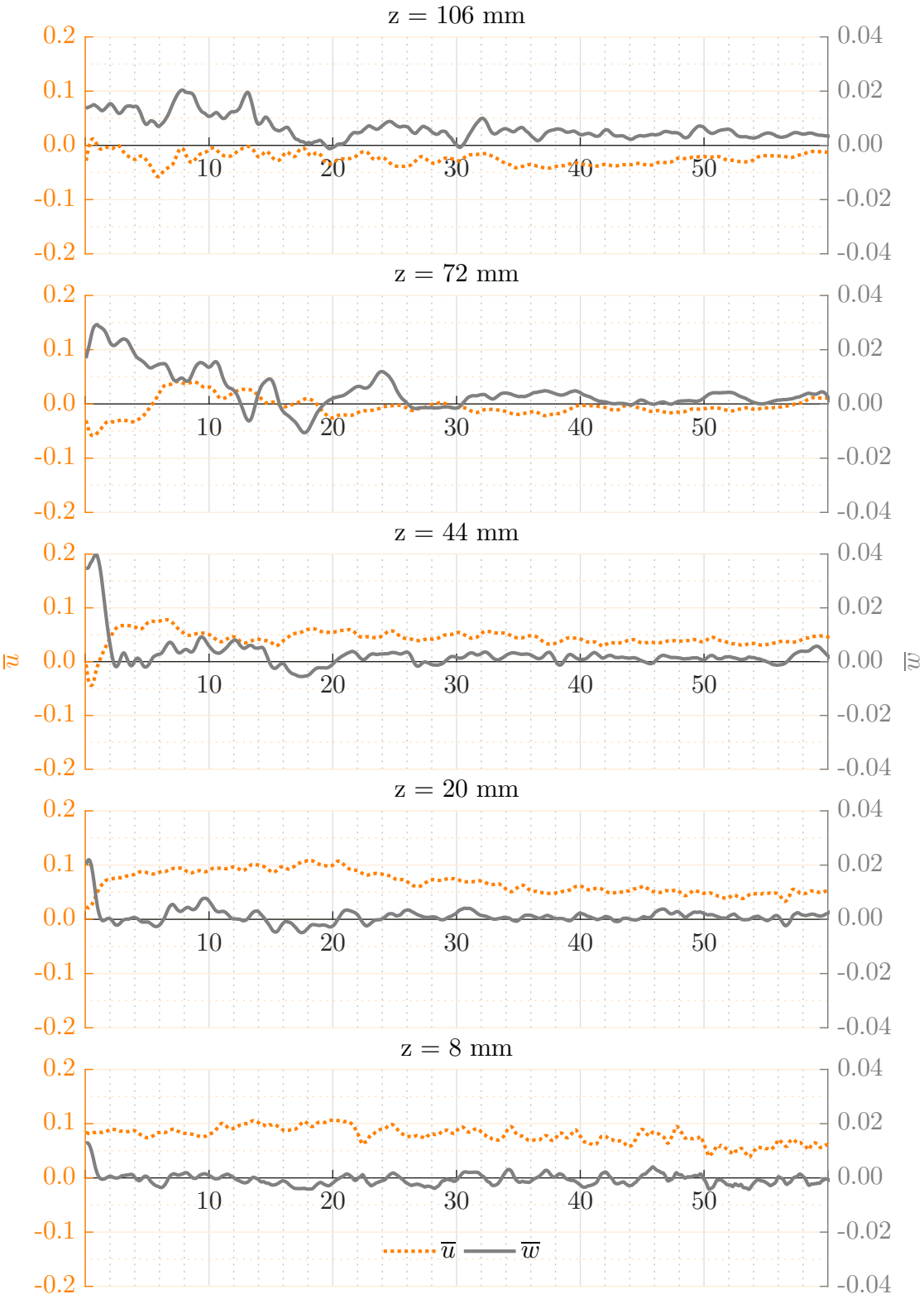

Figure 6.8: Mean streamwise ($\overline{u}$) and vertical ($\overline{w}$) velocities for test R2.medium observed at different heights.

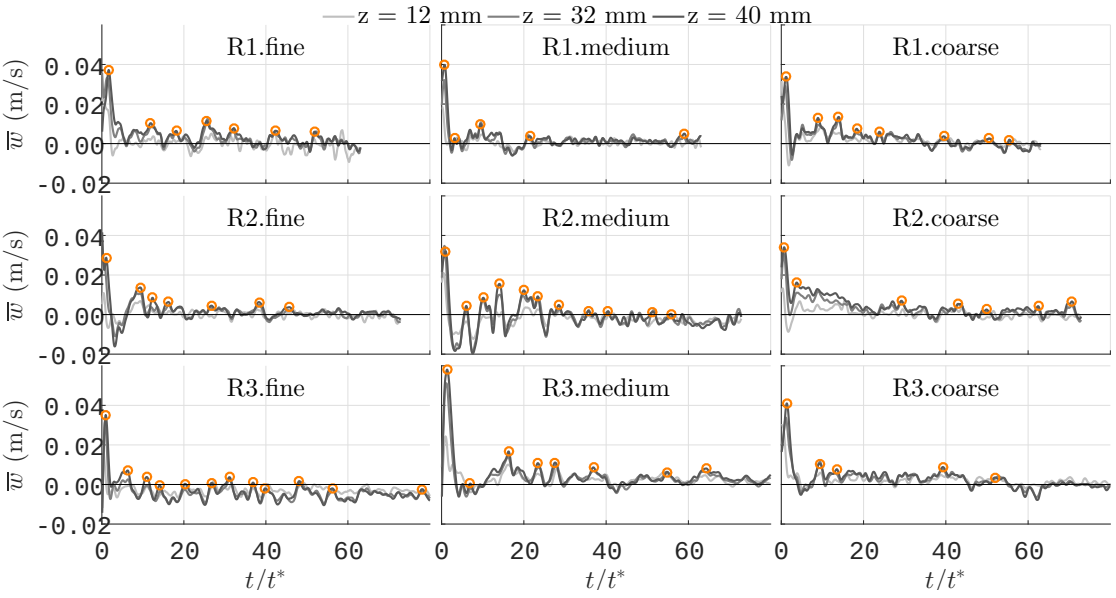

Figure 6.9: Time series of the mean vertical velocity measured at three different positions z = 12 mm, z = 32 mm and z = 40 mm. Orange circles indicate local maxima that corresponds to upward flow.

in the vicinity of the bed. The shaded areas draw attention to some of the troughs of the mean streamwise velocity and the corresponding peaks in RMS quantities. Periods of high turbulence, which correspond to events with clear enhancement of both streamwise and vertical fluctuations, correlate with relatively slow downstream velocities, which is a typical feature of the ejections, one of the most important phases in the so-called burst cycle (Kim et al. (1971), Baas et al. (2005)).

Bed shear stress can be calculated from instantaneous profiles of velocity using numerous techniques (Bagherimiyab and Lemmin, 2013). Here, bed shear stresses were computed using two methods: (1) applying the logarithmic law to the mean streamwise velocity distribution and (2) using the Reynolds shear stress measured close to the bed.

The ADVP instrument allows measurements of the fluctuations of the velocity in three directions and consequently Reynolds shear stresses can be estimated. In a fully turbulent flow, the total bed shear stress can be obtained as follows:

$$\tau_b = \left[\mu\left(\frac{\partial U}{\partial z} + \frac{\partial W}{\partial x}\right) - \rho\overline{u'w'} \right]\Bigg|_{z=z_0} \tag{6.1}$$

where the term $\partial W/\partial x$ can be neglected (Cossu and Wells, 2012) and $\partial U/\partial z$ and Reynolds stresses $-\rho\overline{u'w'}$ are estimated using the velocity measurements at the recorded gate the closest

to the bed.

By using the instantaneous velocity profiles, and through the fitting procedure presented in Appendix A, the time evolution of bed shear stresses calculated by the fit of the log law (τ_{LOG}) can also be calculated. For a representative test (R1.fine), τ_{LOG} and τ_{DEF} are compared and shown in Figure 6.11. The two signals seem related and of the same order of magnitude. In particular, the peaks of bed shear stress are well depicted by both methods.

Bed shear stress is normalized as the Shields parameter (Shields, 1936b) that is computed as:

$$\tau_b^* = \frac{\tau_b}{(\rho_s - \rho_i) g D_{50}} \tag{6.2}$$

Many widely used bed load sediment-transport models are based on the concept that sediment transport begins or it is scaled by, the constant critical Shields stress (Lamb et al., 2008), which is why this non dimensional shear stress value is chosen here. Furthermore, it was possible to veriify that the tests performed in this work fall in the suspended load transport area of the Shields diagram for density and turbidity currents provided in Sequeiros et al. (2010b).

The computed normalised bed shear stress is reported in Figure 6.19 where we can notice that higher values are localised in the frontal region of the current and at the core of the current, in correspondence of the zone of higher streamwise velocity which was previously identified. The body and tail of the current exhibit residual lower values of Shields parameter.

6.4 Sediment dynamics

6.4.1 Sediment entrainment

Video analysis allows tracking of the sediment entrainment from the mobile bed (Figure 3.11). The time evolution of the area occupied by the sediment was determined by identifying the pixels occupied by the sediments in each video frame. In Figure 6.12 the temporal evolution of the area of the image occupied by the current (orange) and the area occupied by the sediments (black), for the first ten seconds where the main sediment mobilization is observed, are shown.

As expected, it is observed that for the currents with lower density flowing over coarser grains, the particles tend to settle faster, which means that the area of sediments drops to zero in a shorter time frame. On the other hand, the tests with a larger initial density and with finer material correspond to larger areas occupied by the sediments, where the sediment is kept in suspension longer reaching higher levels within the current body. Finer sediment and larger initial densities in the lock imply that particles are brought into suspension faster and taken up far away from the bed as shown by the faster increment of the area of sediments curve (Figure 6.12) that is growing from R1 to R3 and decreases from fine to coarse).

In summary, two coherent tendencies can be highlighted: (i) the finer sediment composing the erodible bed is more prone to be mobilized by the current, it remains in suspension longer,

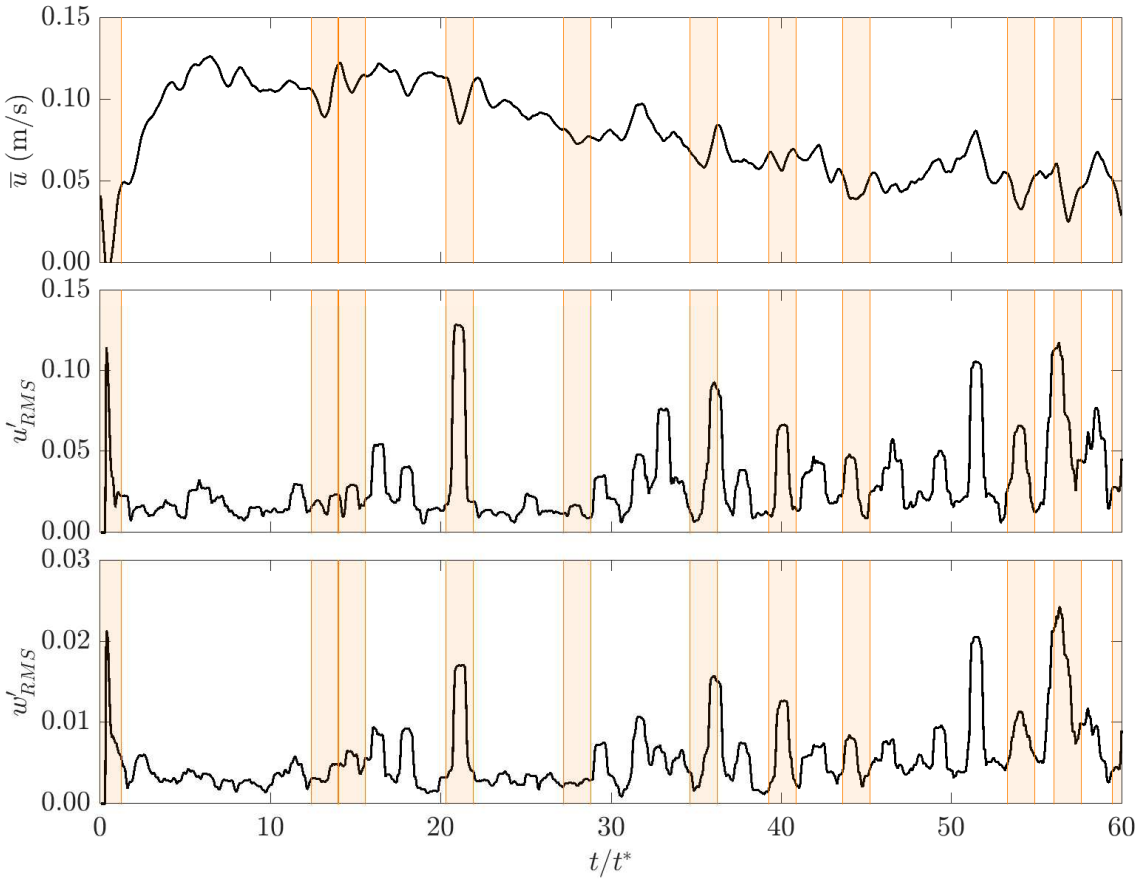

Figure 6.10: Time series of streamwise mean velocity ($\overline{u}$), streamwise and vertical RMS velocities (u'_{RMS} and w'_{RMS} respectively) at z=16 mm for test R1.fine. Shaded columns highlight the troughs of $\overline{u}$ and the associated peaks in RMS quantities.

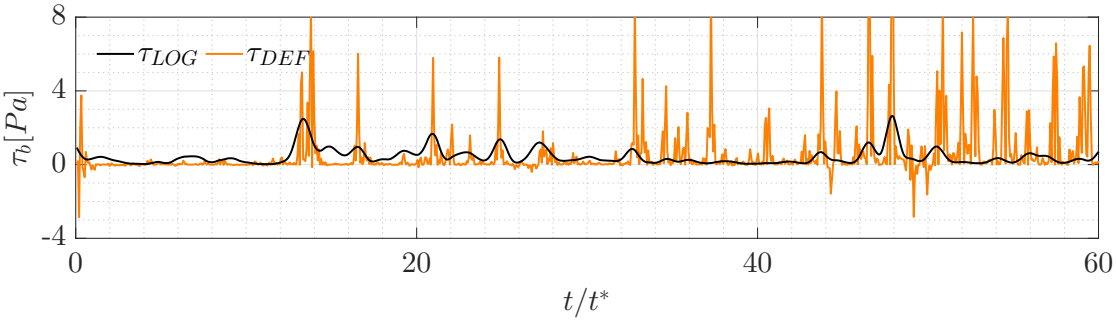

Figure 6.11: Temporal evolution of bed shear stresses calculated by fit of the log law (τ_{LOG}) and from the definition (τ_{DEF}, Eq. 6.1) for one exemplar test (R1.fine).

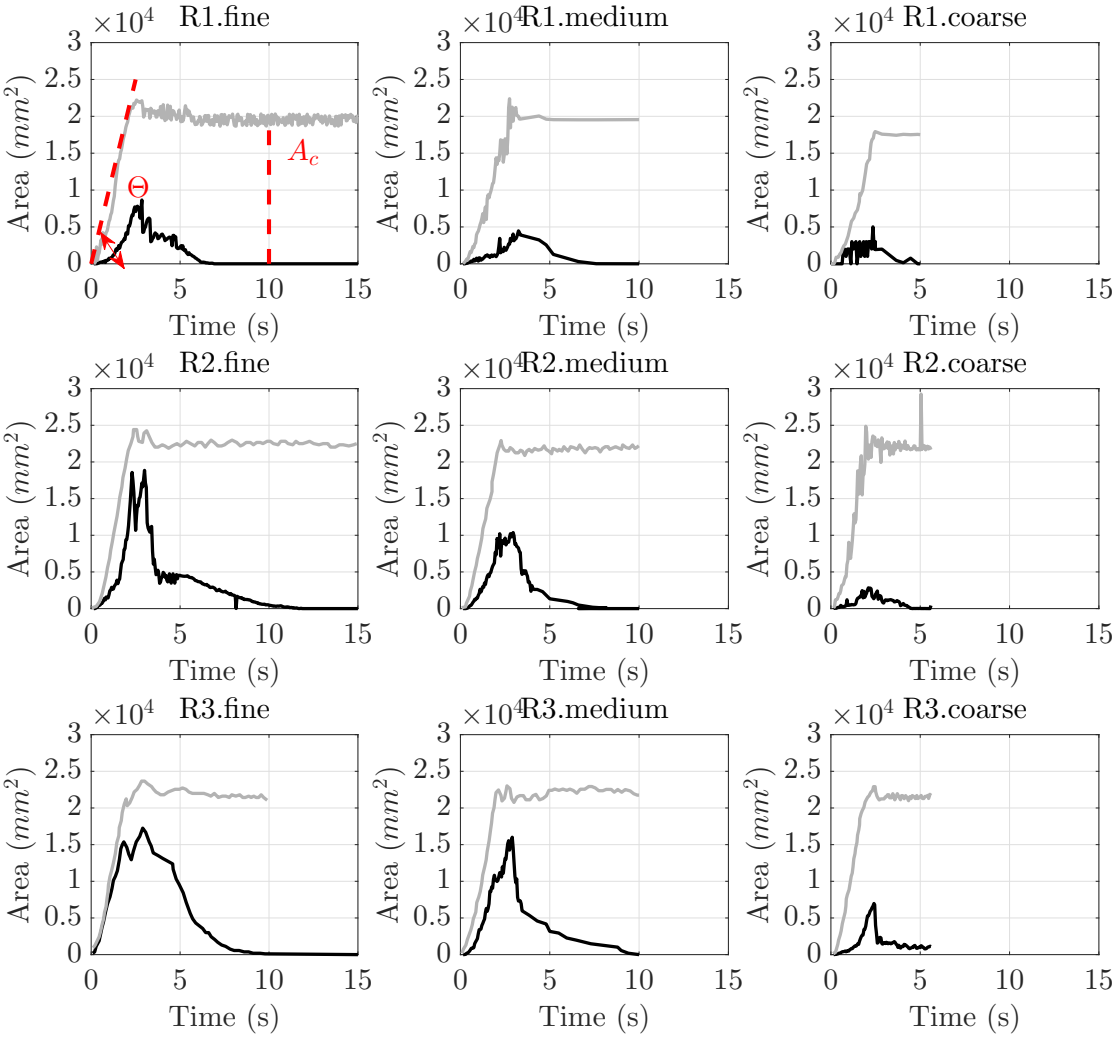

Figure 6.12: Temporal evolution of the portion of the image occupied by the current (gray) and the portion occupied by the sediment (black), for the first seconds, when the main sediment mobilization is observed. The angle formed by the line representing the evolution of the current with the horizontal (θ), and the area of the current (A_c) calculated as described in Section 6.5.3 are also reported. The height of the gravity current (h_c) is directly proportional to area of the current A_c by a factor of 0.245 m (see Figure 3.11).

and it goes higher, and (ii) the increase in excess density between the fresh water and the current enhances the erosion.

6.4.2 Morphology changes

The average (among the eight profiles collected), minimum and maximum longitudinal bed elevations in the mobile bed reach, measured after the passage of the gravity current as described in Section 3.3.4, are shown in Figure 6.13. The average has been calculated among the eight longitudinal profiles collected across this bed region as shown in Figure 3.9. Minimum and maximum values along the longitudinal are also shown in Figure 6.13. The maximum erosion is exhibited by test R3.fine, which is expected since it is the test with the finest grain and the largest excess of density. This tendency is also confirmed by the measurements performed with the video analysis (Section 6.4.1). The 1 cm deep erodible reach is never completely uncovered since the maximum measured erosion is 0.8 cm.

The eroded volume of sediment is calculated by integrating the difference among the topographies recorded before and after the erosion process caused by the passage of the current. Each difference in height ($Z_{BED,before}(x) - Z_{BED,after}(x)$) is integrated along the mobile bed that has a total length l=0.6 m, and then multiplied by the respective area of influence ($A_{ER,i} = A_{ER}/(n+1)$, with A_{ER}=0.275 x 0.6 m^2 as the total surface of the mobile bed and n=8, the number of longitudinal sections recorded, see Figure 3.9).

$$V_{eroded} = \sum_{i=1}^{n} A_{ER,i} * \int_0^l (Z_{BED,before}(x) - Z_{BED,after}(x))dx \tag{6.3}$$

In Figure 6.15 the values of the calculated eroded volumes are shown grouped by the sediment size and by the initial density in the lock. As expected, the eroded volumes of sediment decrease with the sediment size and increase with the initial density of fluid in the lock.

Similar to Figure 6.13, the average, minimum and maximum longitudinal bed elevations are shown in Figure 6.14 for the surveyed downstream area of deposition. It can be observed that higher deposition occurs in the vicinity of the erodible reach. Further downstream, the thickness of the deposited sediment layer decreases. Tests with a lower initial density show the maximum height of deposition, but no clear tendencies with respect to the grain size are detectable. Gravity currents with higher buoyancy have higher velocities and turbulence production which can keep in suspension material for longer distances. In these cases, the deposition rate is lower and the sediments are transported further downstream, outside the present area of investigation.

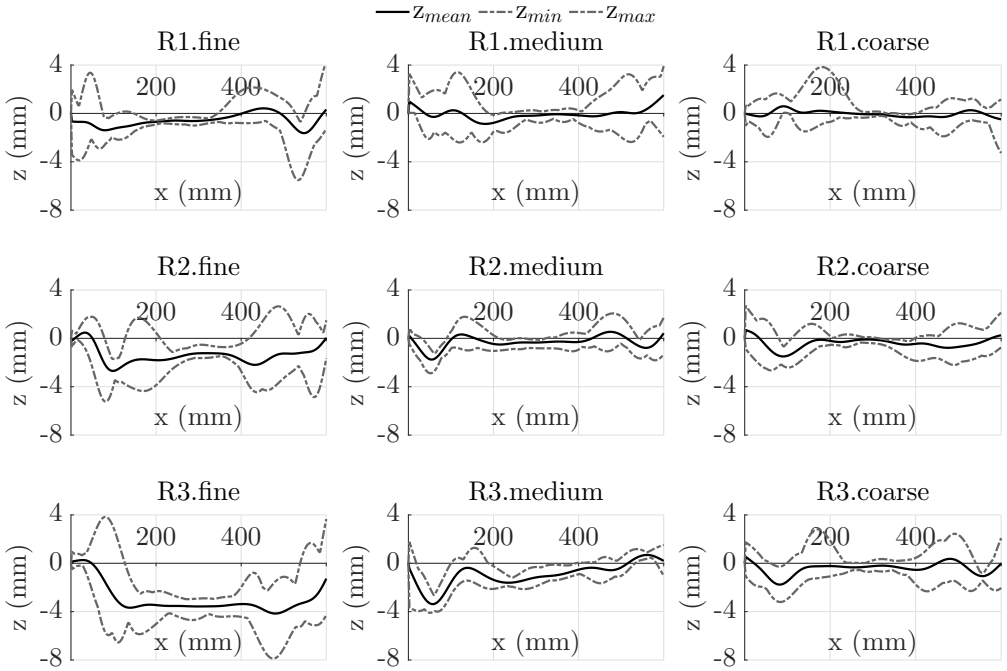

Figure 6.13: Longitudinal bed elevations in the erodible bed after: black the average longitudinal profile; dashed gray lines correspond to the minimum and maximum values across the section.

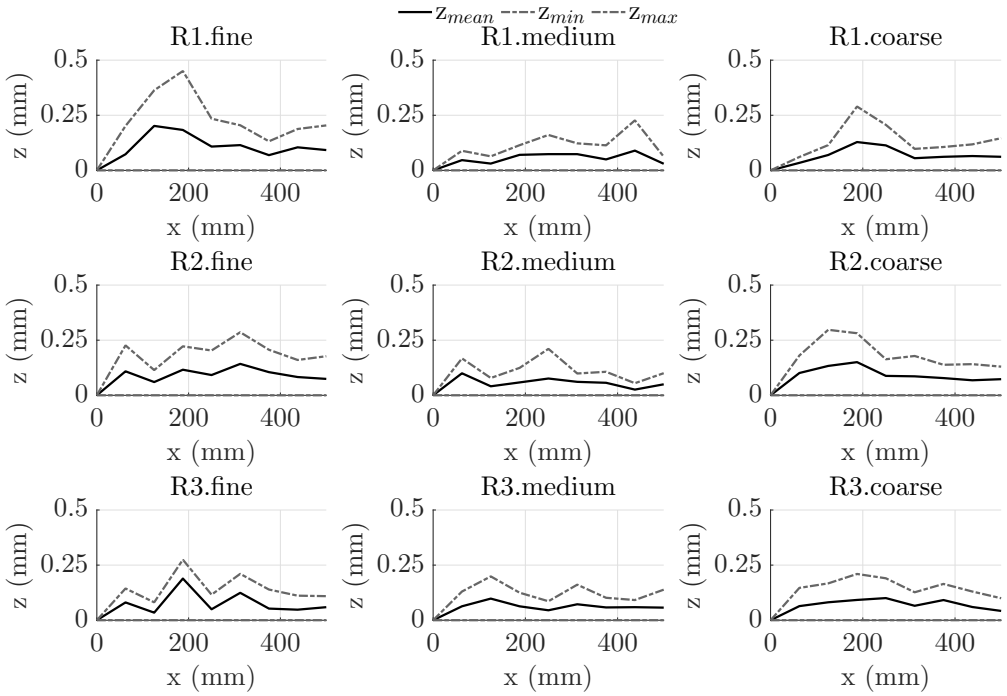

Figure 6.14: Longitudinal bed elevations in the downstream zone of deposition: black the average longitudinal profile; dashed gray lines correspond to the minimum and maximum values across the section.

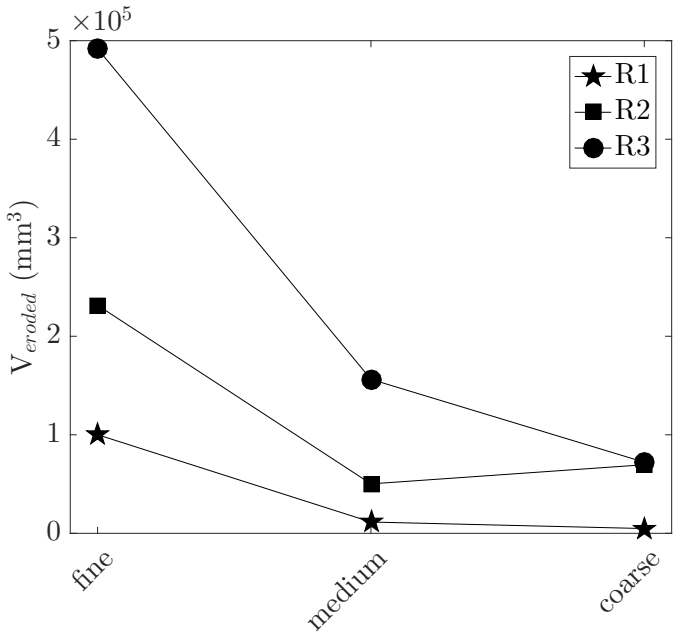

	fine	medium	coarse	
R1	1.0009	0.1145	0.0483	$(10^5 mm^3)$
R2	2.3150	0.5018	0.6961	$(10^5 mm^3)$
R3	4.9183	1.5629	0.7216	$(10^5 mm^3)$

Figure 6.15: Eroded volume of sediment grouped by sediment size and initial density in the lock (in $10^5 mm^3$).

6.4.3 Deposition patterns

In Figure 6.16 the processed images (see Chapter 3.3.6) of the deposition area taken with the camera are shown. The deposited material follows a typical pattern: longitudinal streaks are observed, as already noticed in some previous studies (Grass (1971), Colombini and Parker (1995)). These longitudinal streaks were explained by these authors as being the result of the rise of light ambient fluid trapped at the bed of the overrun front of the gravity current through the denser fluid into the gravity current (some references: Eames et al. (2001), who studied gravity currents experimentally, and Ooi et al. (2009), who studied them numerically). This movement of fluid creates streamwise-oriented vortices aligned with the primary flow, which are responsible for the imprinting of elongated streaks of deposited sediment (Weill et al. (1985), Cantero et al. (2008)).

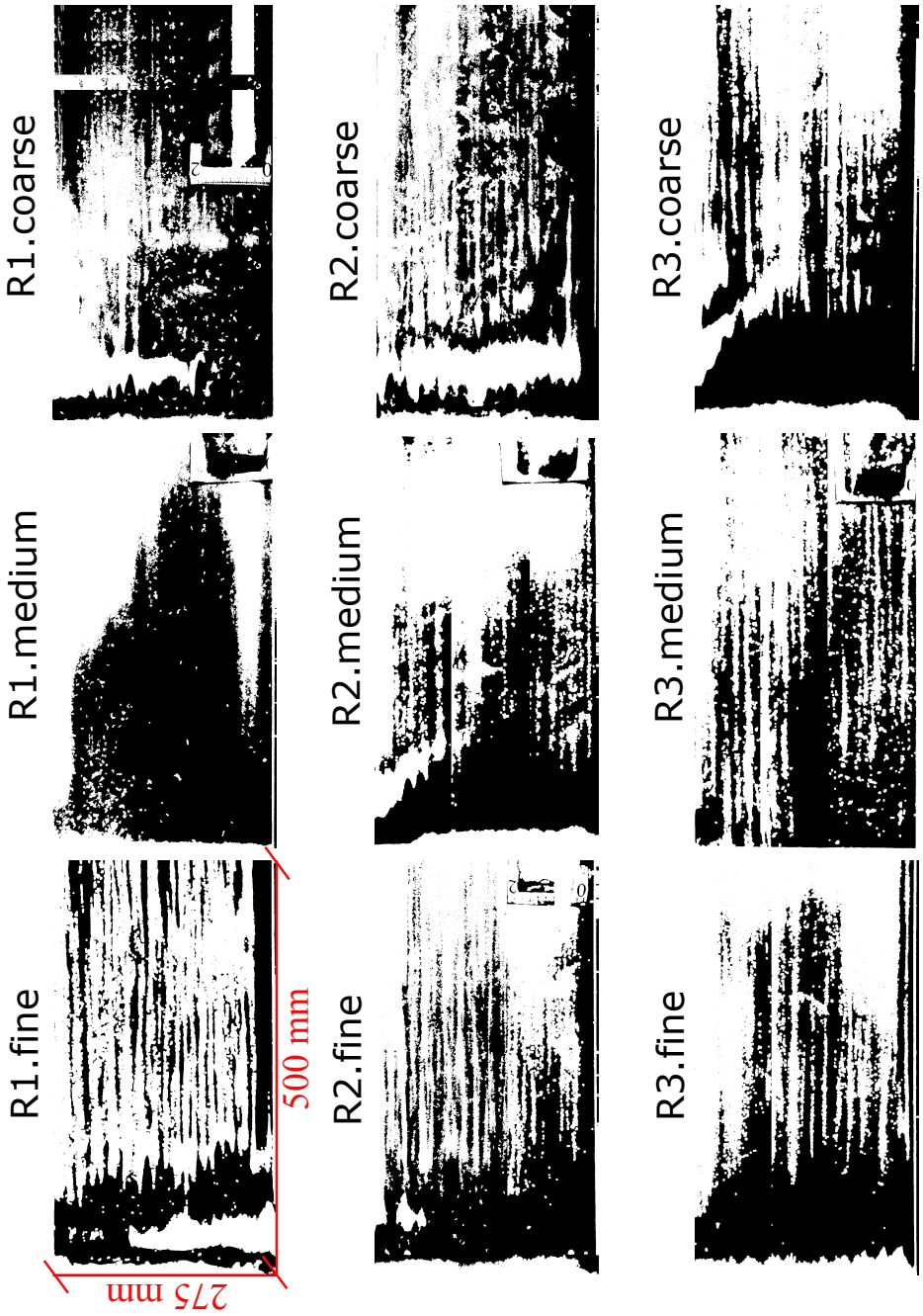

Figure 6.16: Binary images of the region downstream the mobile bed where deposition occurs.

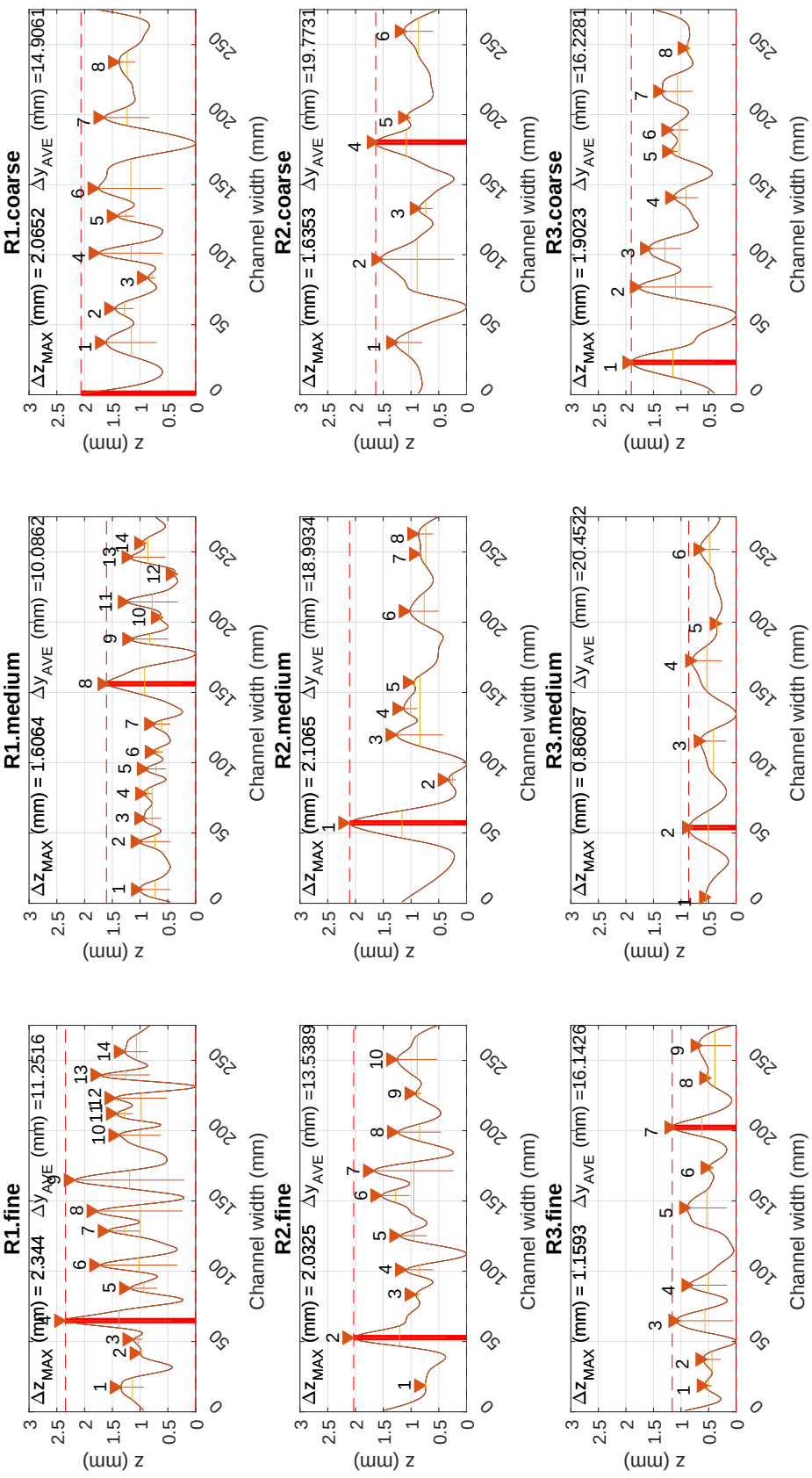

Figure 6.17: Topography measured at the cross section C4 located 0.27 m downstream the mobile bed. Maximum amplitude of deposition (Δz_{MAX}) and average thickness of the streaks (Δy_{AVE}) are also reported.

The cross sections recorded with the laser in the downstream reach can provide a measure of number of streaks ($N.streaks$), their maximum amplitude of deposition (Δz_{MAX}) and average thickness of the streaks (Δy_{AVE}). These measurement have been analyzed for the cross sections (as shown in Figure 6.17) for all the tests performed. Section C_4 was considered (0.27 m downstream of the mobile bed), since, taking advantage of the pictures, it is observed that at this distance from the erodible bed, the streaks are well developed for all the experiments. The information in Figure 6.17 suggests that generally the number of streaks decreases with increasing initial density and with coarser material and that the thickness of the streaks (Δy_{AVE}) is greater for higher initial density and it increases with coarser material. Instead no clear tendencies are detected for the maximum amplitudes of deposition Δz_{MAX}.

To determine the geometry of the streaks, a shape factor (Podczeck, 1997) is computed as:

$$f_{elong} = \frac{2 * \Delta z_{MAX} + \Delta y_{AVE}}{\Delta z_{MAX}} \tag{6.4}$$

f_{elong} measures how elongated is the section of the streak. Figure 6.18 shows the relation between gravity currents initial density, grain size composing the erodible bed, number of streaks and streak section shape. It is here proven that greater initial excess density and the presence of coarser material generate less streaks whose section is less elongated.

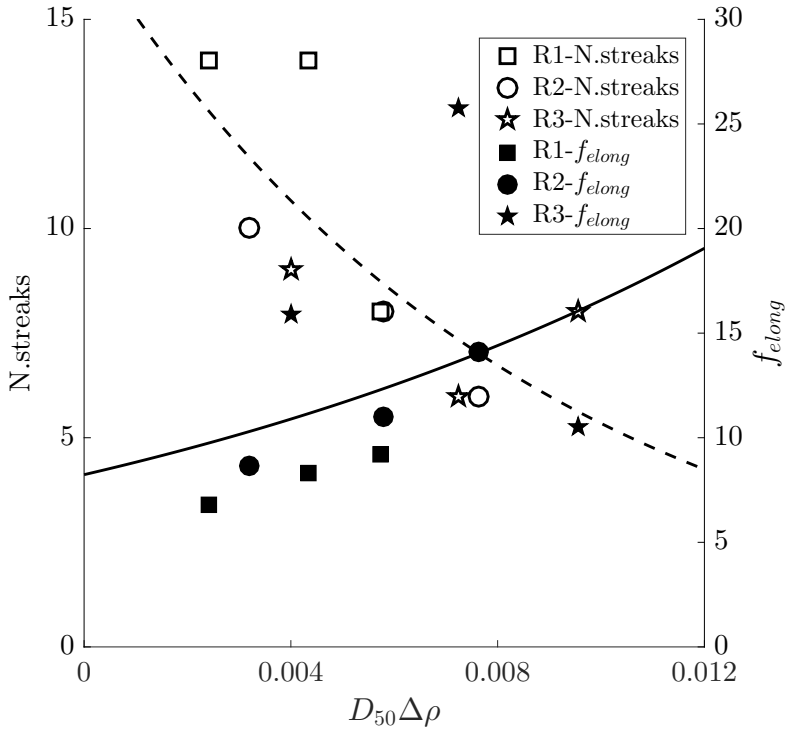

Figure 6.18: Relation between gravity currents initial density (here presented as the excess density $\Delta\rho$), grain size composing the erodible bed (D_{50}), number of streaks ($N.streaks$) and streak section shape (f_{elong}).

6.5 Discussion

6.5.1 Mechanisms governing sediment entrainment and distal transport

The relationship between sediment entrainment and bed shear stress in a gravity current is widely acknowledged in literature (Hirano et al. (1985), Parker et al. (1986), García and Parker (1993), Sequeiros et al. (2010a)). When the bed shear stress caused by the gravity current passing over the mobile bed exceeds a critical threshold of particle motion, erosion may occur. However, bed shear stress is not the only force acting at the bed boundary of a gravity current, and because this flow is highly turbulent, other forces play a role in sediment entrainment. In particular, vertical velocity is expected to enhance vertical mixing, and its contribution in the incipient motion of sediments was addressed here. The normalised bed shear stress τ_b^* calculated from the log law (as in Section 6.3.3)(1), the depth-averaged (over the height of gravity currents) vertical mean velocity $\overline{w}_d$ (2), the corresponding depth-averaged fluctuation w'_d (3), and the depth-averaged Reynolds stresses $u'w'_d$ (4) are subsequently compared to the area of entrained sediments. All these quantities are plotted together in Figure 6.19 with the same time reference.

Before sediment entrainment begins, a peak in the mean vertical depth-averaged velocity is observed, and alternating positive and negative oscillations follow. w'_d has the same evolution and contributes to intensifying the fluctuating behaviour of vertical flow movements inside the current. A decrease in vertical velocity is detected, corresponding to the initiation of sediment entrainment. Bed shear stress also has a minimum during the period in which sediment entrainment is important, which is during the passage of the head of the current (delimited with the vertical dashed line in Figure 6.19). The body is characterized by almost no sediments in suspension and important values of bed shear stress.

To understand the underlying mechanisms of sediment entrainment, the cross-correlation between the time-varying area of entrainment, displayed in Figure 6.12, and the other time-varying hydrodynamic variables, presented in Figure 6.19, is calculated and presented in Figure 6.20, together with the 0.05 statistical significance level.

Figure 6.20 shows that the mean and fluctuating components of the depth-averaged vertical velocity are highly correlated with the entrained area in the first instants of the passage of the current, and subsequently, this correlation rapidly decreases. Conversely, the bed shear stress and depth-averaged Reynolds shear stresses correlate with the entrainment area for a longer period. Mean and fluctuating components of depth-averaged vertical velocity are then indicated as major factors for sediment lifting, as their correlation with the area of sediments is at the maximum at the moment in which sediment entrainment initiates. The high correlation of the cloud of suspended sediments and bed shear stress indicates the importance of the latter in the distal transport of sediment. Once the sediment becomes mobile because it is dislocated from the bed, excess bed shear stress causes its downstream movement.

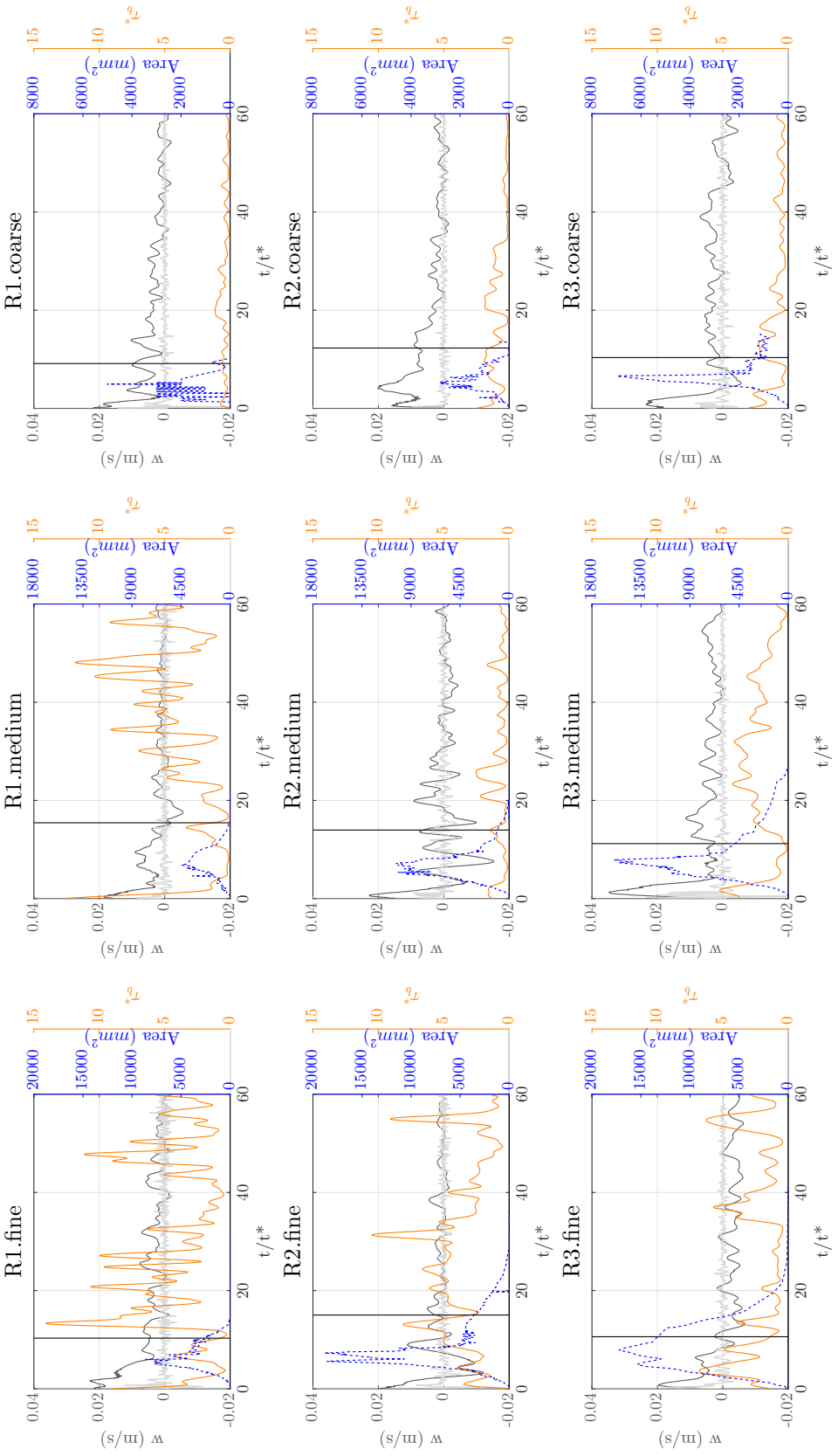

Figure 6.19: Temporal evolution of normalized bed shear stress τ_b^*, depth averaged vertical mean velocity $\overline{w_d}$ (black line), depth-averaged vertical velocities fluctuation w_d' (gray line) and area of sediment entrained (dotted line, see Figure 6.12). The vertical line is the limit of the head L_h as calculated previously.

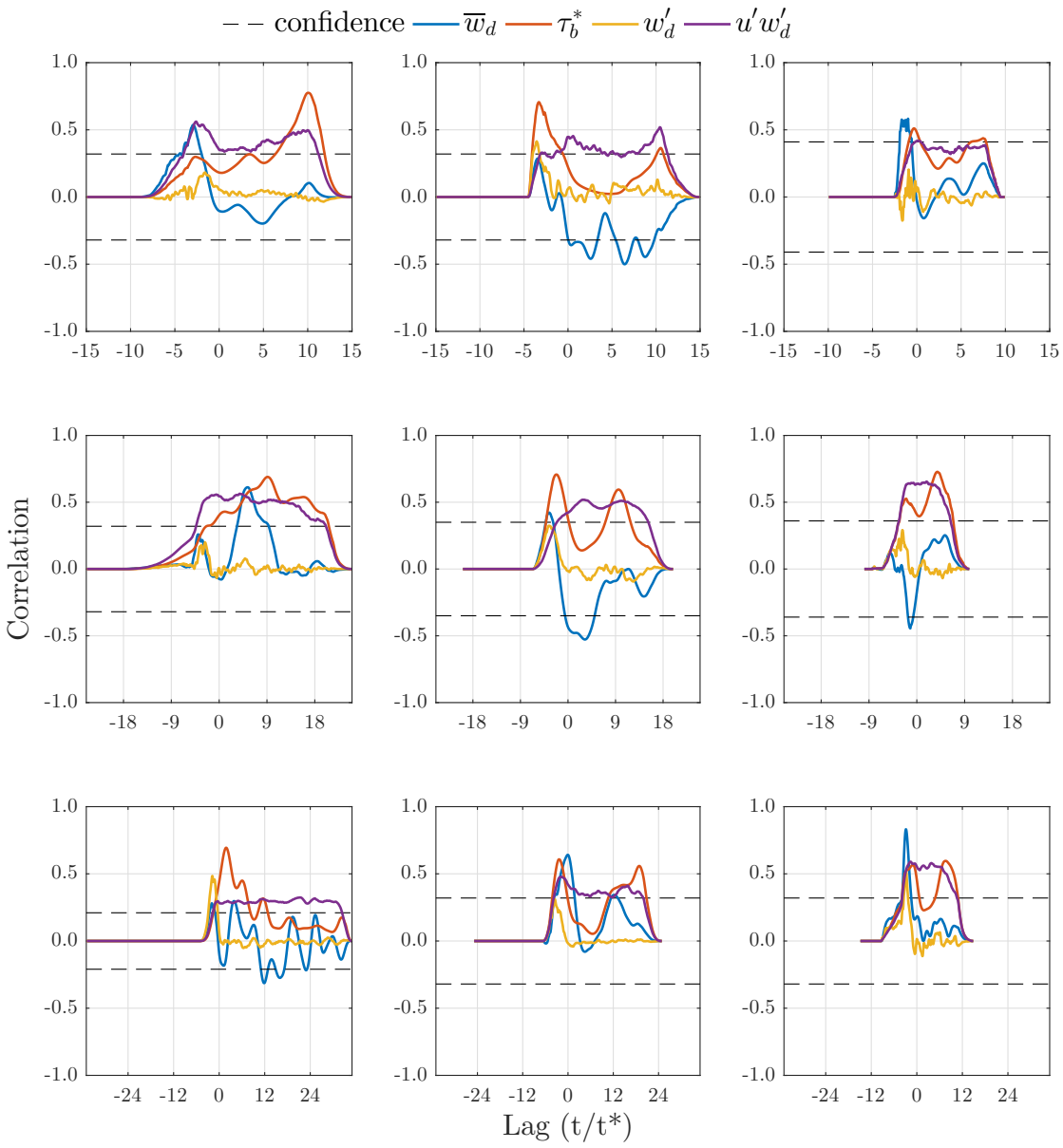

Figure 6.20: Cross-correlation between the entrainment area (as in Figure 6.12) and: (1) depth averaged vertical mean velocity; (2) bed shear-stress; (3) depth-averaged vertical velocity fluctuations and (4) depth averaged Reynolds-stresses. The two horizontal lines represent the statistical significance level of 0.05.

6.5.2 Dynamics of sediment transport and deposition

Gravity currents are turbulent flows which experience the presence of near wall turbulent coherent structures (Grass (1971), Kneller et al. (1999)) as those are common features of boundary layer turbulence (Defina, 1996). Turbulent bursting events characterize these type of flows which consist of the movement of low-speed fluid ejected away from the wall (Salim et al., 2017). Streamwise-oriented vortexes, called horseshoe vortexes (Salim et al., 2017), aligned with the primary flow, are formed and they are responsible for the imprinting of elongated streaks of deposited sediment. The development of a horseshoe vortex showing the lifts, stretches, ejection, and sweep associated with velocity profiles is shown in Figure 6.21.

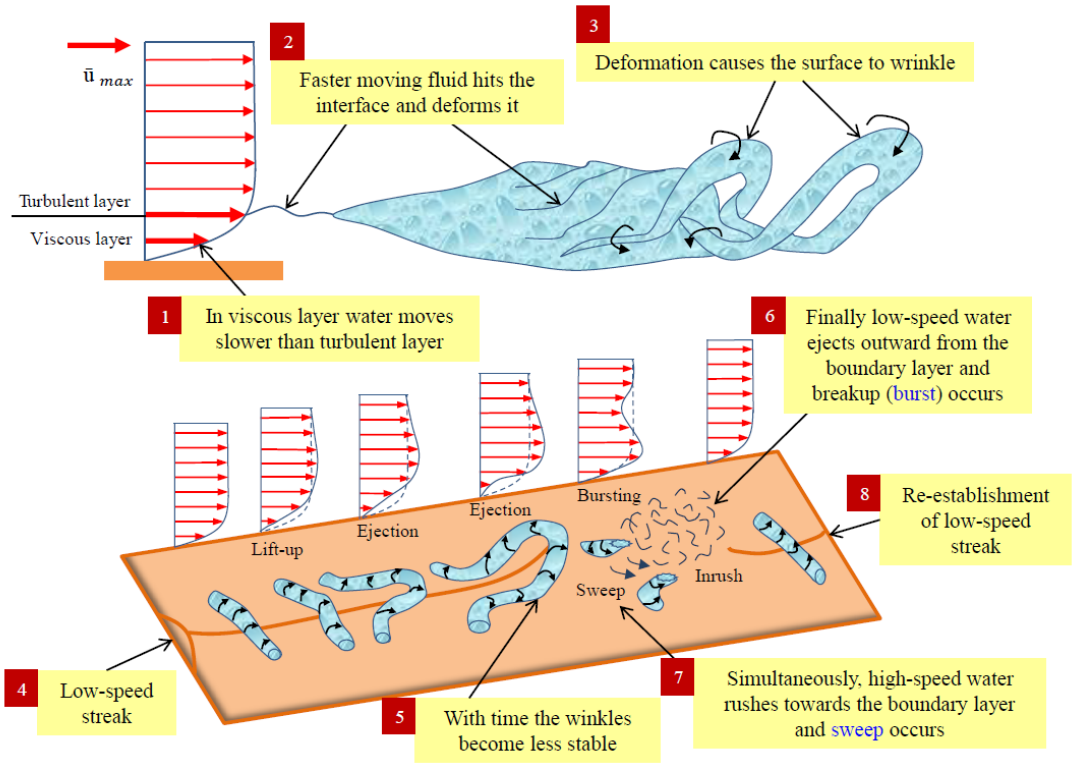

Figure 6.21: Schematic diagram of the typical sequence of turbulent bursting phenomena presented by Salim et al. (2017) (and modified from Allen (1984)) where the flow is directed from left to right and the arrow length represents the relative velocity in the velocity profiles.

Many studies have been conducted on the streaky structure in the wall region of many types of turbulent boundary layer flows (Grass (1971), Defina (1996), and Allen (1985), among others). The signature of these patterns in the deposition have been observed in the present tests

(see Section 6.4.2). Figure 6.16 shows the formation of elongated accumulation of sediment bands on the streamwise direction. Since the only forces acting on the sediment originate in the flowing fluid, the fact that they are arranged in streamwise oriented bands can only be due to a transverse component of fluid force (Allen, 1985). The fluid motion of the gravity current has been thoroughly analysed, and Figure 6.10 provides evidence of the simultaneous presence of mean streamwise velocity troughs with peaks of RMS velocities. Periods of high turbulence that correlate with slow mean streamwise velocity are typical for coherent flow-turbulent structures such as ejections (Kline et al. (1967), Baas et al. (2005)). In the ejection phase, low-speed fluid is ejected upward, and simultaneously, a local and adjacent convection streamwise recirculation cell will quickly form.

The formation of longitudinal streaks in the bed is the result of the convergence of downwelling flow associated with these flow streamwise cells. The size and shape of streaks are flow dependent, and the average streak spanwise spacing was confirmed to be influenced by the initial density (Figure 6.17). Kaftori et al. (1995) shows that with an increment in the bottom shear stress, for a given fluid-particle combination, more particles are entrained and the streaks begin to shrink in size. This tendency is continuing until a point in which there are not enough particles at the wall and the streaks disappear. Here we found that gravity currents generated by higher excess densities produce more spaced streaks. This can therefore be linked to the presence of more energetic counter-rotating streamwise vortices (Niño and Garcia, 1996).

For what concern the influence of the grain size, previous literature reports that particle sorting along low-speed streaks occurs only if the particles are of sizes about equal or smaller than the thickness of the viscous sublayer (Kaftori et al., 1995). Moreover, larger particles have more inertia than smaller ones and therefore they are less responsive to flow velocity fluctuations, as it was already pointed out by Niño and Garcia (1996). Here, the influence of the grain size of sediments composing the erodible reach is translated into a tendency to have streaks sections which are less elongated with coarser grains, as confirmed by Figure 6.18. Coarser particles are more easily settled out from the flow and they are pushed aside to form streaks which are characterized by higher average thickness. This indicates that a feedback exists between the turbulence-caused coherent motion which is at the origin of the flow streaks and the mobile bed which conditions the spacing scale of these.

6.5.3 Quantitative analysis of sediment erosion

The sedimentological impact of a gravity current is the result of the complex hydrodynamics of this flow. Sediment entrainment is a complex mechanism mainly due to the difficulty in defining the fluctuating nature of turbulent flow (Salim et al., 2017). Bed shear stress, is considered a "surrogate" measure of the entrainment capacity of the gravity current (Hickin, 1995).

Thus, to characterize the relation between sediment entrainment and bed shear stress caused

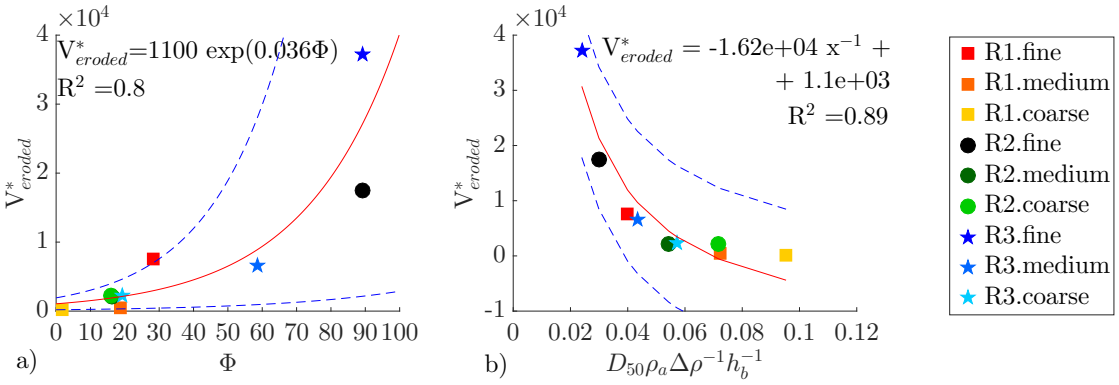

Figure 6.22: (a) Relationship between specific dimensionless eroded volume and the work done by the shear stress produced by the passage of the gravity currents have been analysed through the non dimensional quantities Φ and V^*_{eroded}. The 50% confidence intervals are also reported with the dashed blue lines. (b) Dependence of the ratio between grain size and gravity current initial density (with the adimensional parameter $D_{50}\rho_a\Delta\rho^{-1}h_b^{-1}$) on specific dimensionless eroded volume (V^*_{eroded}). The 95% confidence intervals are indicated with the dashed blue lines.

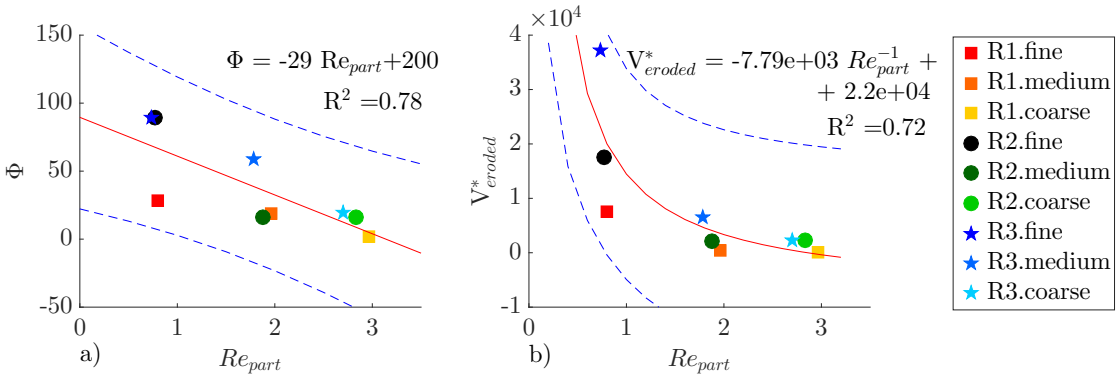

Figure 6.23: (a) Particle Reynolds number (Re_{part}) versus work done by the shear stress (Φ) produced by the passage of the gravity currents. The 95% confidence intervals are indicated with the dashed blue lines. (b) Re_{part} versus specific dimensionless eroded volume V^*_{eroded}.

by the passage of a gravity current, the quantities defined in Chapter 4.3.5 have been used. Here an adimensional version is adopted in order to consider the normalized bed shear stress. Shields normalization allows to compare the driving forces that induce particle motion (the bed shear stress, τ_b) to the resisting forces that depend on the sediment characteristics (ρ_s and D_{50}). Therefore the quantity Φ is rewritten in non dimensional form and it is defined as:

$$\Phi = \int_0^T \tau_b^*(t)\,dt/t^* \tag{6.5}$$

where the limit T defines the end of sediment entrainment, obtained by the area of sediment entrained in Figs.6.12 and 6.19. A specific dimensionless eroded volume has been defined as:

$$V^*_{eroded} = \frac{V_{eroded}}{D_{50} * A_{tot}} \tag{6.6}$$

where V_{eroded} is calculated as in Chapter 6.4.2 and is the volume of eroded sediment, A_{tot} as indicated in Figure 3.9. In Figure 6.22a the quantities calculated per each test are presented one against the other and they show a coherent tendency: an increase in the non-dimensional work is related to an increase in the erosion. The relationship between the eroded volume and a variable which takes into considerations the initial density of the gravity current (surrogate of the erosion force) and the grain size (surrogate of the resistance to erosion) is shown in Figure 6.22b. The eroded volumes decrease with increasing $D_{50}\rho_a\Delta\rho^{-1}h_b^{-1}$ (adimensional parameter that accounts for the grain size and excess buoyancy), confirming that in the case of low initial density and with coarser sediments, the material on the erodible reach is less mobile and the erosion is consequently weaker. The particle Reynolds number, which takes into account both the sediment representative diameter and the density by means of the reduced gravity, was computed as follows (García and Parker, 1993):

$$Re_{part} = \frac{\sqrt{g' D_{50}} D_{50}}{\nu} \tag{6.7}$$

Figure 6.23a shows Φ as a function of Re_{part}. According to the well known Shields diagram (Shields, 1936a), and the modified version as in Sequeiros et al. (2010a), low particle Reynolds numbers correspond to sediment that may be transported as suspended material. Figure 6.23a is the adapted left hand side of the Shields diagram, which fall in the suspended load area. Video observations confirmed the presence of suspended particles all over the flow even close to the bottom surface.

In Figure 6.23b, the dependence of the dimensionless specific eroded volume (V_{eroded}) on the particle Reynolds number (Re_{part}) is shown. Particles characterized by a lower Re_{part} exhibit an easiness to be entrained, and consequently, the measured eroded volume is greater.

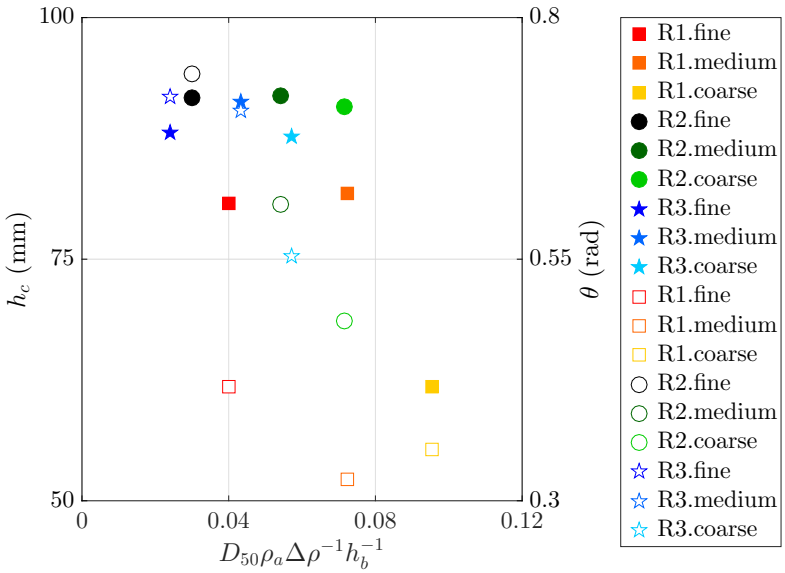

Figure 6.24: The angle (θ, (rad) and the height of the current (h_c, (mm)) calculated from video analysis (empty symbols are for right side y-axis θ, filled are h_c, y-axis on the left side).

6.5.4 Effect of sediment entrainment on the gravity current

As hypothesized earlier, the hydrodynamics of the current are influenced by the incorporation of the sediment present at the bed, and this interaction is conditioned by the sediment diameter. Changes in the geometry of the front that are related to the flow resistance are observed in the time evolution of the area of the current, as reported in Figure 6.12. From Figure 6.12, two quantities have been calculated: θ, the angle formed by the line representing the evolution of the current (in gray) with the horizontal (by means of merely geometrical considerations using the lines as presented in Figure 6.12), and h_c, calculated as the average area of the portion of the image occupied by the current, divided by the horizontal dimension of the frame captured with the high speed camera. These two have been compared to $D_{50}\rho_a\Delta\rho^{-1}h_b^{-1}$ (Figure 6.24).

Figure 6.24 shows that the current height h_c increases at a higher rate (θ) in presence of finer sediments. This is an evidence of how the incorporation of sediment changes the hydrodynamics of the current: the tests where larger quantity of sediment is incorporated (cf. Figure 6.12) are the ones where the angle θ is higher. The results suggest that the incorporation of sediment within the current induces internal energy losses which induce the higher velocity of increase of h_c. However, the influence of the incorporation of sediment in the current geometry is not so evident when regarding the current depth. In fact, only for the case of the lower initial densities in the lock the incorporation seems to produce an effect.

6.6 Conclusions

Erosion, transport and deposition of fine sediment caused by the passage of a saline gravity current were investigated experimentally. For this purpose the cross-analysis of data from several measuring techniques was done: instantaneous velocity profiles measured with an acoustic Doppler velocity profiler, video analysis, laser based topography and pictures of deposition patterns compose the available data-set. The tests, carried out with a lock-exchange channel with high volume of release flowing over a mobile-bed reach, included three initial densities of the fluid on the lock and three different sizes of sediment composing the mobile bed reach. Mean flow and fluctuating quantities were estimated and discussed taking into account the different triggering densities in the lock. Different size classes of suspended sediment react differently to the changes in flow dynamics determined by the initial density in the lock.

Among the computed hydrodynamic quantities such as turbulent and mean upward velocity, bed shear stress and turbulent stresses, we show that bed shear stress and Reynolds stresses are correlated with sediment entrainment for longer periods, thus it can be inferred they are associated with the distal transport of sediment. The main factor responsible for sediment dislodging is found to be the vertical component of the fluid movement, which presents a high peak of vertical mean velocity at the front of the currents. Upward motion, characterized by the mean vertical velocity and aided by the vertical component of turbulence, promotes vertical mixing of the sediment from the channel bed, whereas in the periods between these flow structures the particles have sufficient settling velocities to deposit, with the coarser particles depositing sooner than finer ones.

The combined analysis of the hydrodynamics and the geomorphic imprint of the passage of the gravity current on the mobile bed, shows a clear relationship between erosion and current shape. Furthermore, our results indicate that the deposition downstream of the mobile bed presents the signature of counter rotating vortices aligned with the primary flow in the streamwise direction. Therefore, the presence of feedback mechanisms is assumed, with the hydrodynamics of the current imprinting the streaks, and entrainment of sediment modifying the current hydrodynamics, thus resulting in different streak geometries.

7 Conclusions and future research

7.1 Conclusions

To meet the aims of the present research study, three groups of tests were performed by changing initial conditions and set-up configurations reproducing gravity currents that are commonly observed in nature.

The first set of experiments allowed testing of the influence of the initial released volume of dense fluid and the initial excess density on the anatomy of the gravity current. Making use of instantaneous velocity measurements along the whole vertical section, the hydrodynamic properties of the highly turbulent flow could be determined. It was possible to characterize both horizontal and vertical structures of the gravity currents which were found to vary with the amount of released saline water.

The second group of tests allowed determination of the effect of extra gravitational forces here produced by introducing a slope on the lock reach of the channel. The behaviour of the current was analysed, focusing on the water entrainment at the upper interface and the potential erosion capacity at the bottom. This analysis revealed that the presence of extra gravitational force, for the range of small slopes analysed herein (S=0-16%), do not play a role in enhancing bottom erosion.

Finally, the third set of tests were performed with the presence of a mobile bed reach. A complex set of instruments was used in order to record the sediment transport process operated by the passage of a gravity current. The forces responsible for the picking up of sediment are identified. The interaction between gravity current and entrained material has been discussed. It could be highlighted that the shape of the front changes due to sediment entrainment and that the deposition of sediment downstream creates characteristic patterns whose geometry reflects the coherent turbulent structure of the current.

The main scientific findings are summarized in the following by answering the research questions initially raised:

Q1 *How can the head and body regions of a gravity current generated by lock-exchange method be defined and which are their characteristic features?*

In order to systematically define the extension of head and body regions, a kinematic function has been defined as the product of depth averaged streamwise velocity and current height (which is identified by the zero-streamwise velocity contour). This is particularly important since a universal criterion was not established yet, even if the distinction of these two regions is widely accepted in literature. Head and body are known to have different hydrodynamic behaviours and consequently a different role in sediment entrainment and transport of mass and momentum. It was therefore of paramount concern to circumscribe those zones. The

function $H(t) = h_d(t)h(t)$ was used. The head was identified by the first meaningful local minimum and the body by the extension of the linear portion of the cumulative sum of the function H.

The variation in the shape of the current is mainly consequence of the entrainment of water at the upper interface. The current evolves along its path, depending on the initial volume of dense fluid released and on the volume available for the propagation of the release until the observation point. These are taken into account by the normalization L_i/L_p used here which makes it possible to observe that the initial excess density does not influence the shape of the gravity current.

Q2 *Which is a common structure of the inherent vortical movements of lock-released gravity currents and how does this affect the mass and momentum exchange?*

It could be shown in this research project that a structure composed of three main zones characterizes the vorticity field of gravity currents. The first zone is located at the core of the head and in vicinity of the bottom (the inner layer), where positive vorticity with inner movements rotating in the direction of the principal motion take place.

A second zone is at the rear part of the heightened head and along the upper interface of the flow. The flow in this mixing zone is characterized by movements which go inversely with respect to the direction of the main flow (Kelvin-Helmholtz vortices are here present). Their strength decreases with time (and thus along the flow) and becomes negligible in the tail of the current. At the mixing layer, ambient water is entrained into the gravity current and due to its character it cannot be delimited by clear boundaries. It could be shown that the Ellison and Turner (1959) height and the zero-streamwise velocity contour provide a valid indicator of the approximate limits of this second zone of high vorticity.

Finally, the third zone is located between the two previously defined. Residual negative vorticity expands from the upper layer towards the bottom, showing progressively lower intensity.

The elaborated definition of the vertical structure is of special interest when a numerical simulation of these flows is attempted. In fact, the most commonly used theoretical models are based on depth averaged quantities assuming that there are no significant variations of the properties of the current along the vertical. The use of depth-averaged models is adapted for modelling the evolution of the current. Nevertheless, when the description of the vertical structure is attempted, a proper parametrization should be used. The analysis provided here gives the base for the formulation of a model that can relate the shape of the current with its hydrodynamics, including mass and momentum exchange, without the need of resolving the vertical current properties.

Q3 *Which parametrization can be adopted to quantify entrainment from the upper and lower layers that takes into account the spatio-temporal variability of the gravity currents?*

New quantities to account for the upper water entrainment ($\Phi_m = \int_{T_1}^{T_2} \tau_m(t) dt/t^*$) and the bottom erosion capacity ($\Phi_b = \int_{T_3}^{T_4} \tau_b(t) dt/t^*$) could be defined. These quantities are calculated as the time integral of the shear stress. By dimensional analysis, they represent the work done by the gravity current, for a certain advection velocity, per unit surface. The relation between the upper resistance of the flow so computed and the Richardson number could be verified, giving strength to this new definition. At the bottom, the erosion capacity is proved to be related with the volume of sediment entrained. Both quantities are highly dependent on the initial release conditions. On horizontal bed conditions, it has been demonstrated by the experimental tests that the extent of the body region, that changes in relation to the initial volume of release, has a prior role in the bottom entrainment capacity. At the interface, the mixing zone thickness increases exponentially with the time integral of the shear stress as a consequence of the dilution due to water entrainment and this is enhanced with bigger initial released volumes.

Q4 *How does gravitational force, increased by the presence of a slope in the lock, affect ambient water entrainment and potential erosion capacity? How is the current shape modified?*

Gravity currents reproduced with increased gravitational forces are subjected to two main mechanisms: (i) the increment of shear stress at the upper interfaces which causes a higher water entrainment and (ii) the acceleration of the fluid, mainly at the rear steady part of the current, which therefore feeds the forerun head. The range of tested slopes allowed identification of the transient conditions where the mentioned mechanisms become relevant. For S<16%, the dilution caused by the enhanced water entrainment reduces the mean streamwise velocity. At S=16% an inversion of this tendency is noticed, most probably due to the effect of the extra gravitational forces that accelerate the fluid. Under this configuration an extended body formed as the result of water entrainment at the upper surface of the current that creates dilution and the expansion of its body. Thus, the resulting bottom erosion capacity is reduced by the presence of the extra gravitational forces due to lower streamwise velocities which followed gravity currents dilution.

Q5 *Which are the mechanisms governing the entrainment, transport and deposition of sediment and how the hydrodynamic of the gravity currents act to induce geomorphic changes on a mobile bed? Which is the feedback process on the gravity current generated by the incorporation of entrained sediment?*

Gravity currents flowing on a mobile bed entrain sediment following its hydrodynamics and the characteristics of the material present at the bottom. Both mean and turbulent vertical flow field revealed the presence of peak values on the foremost part of the current followed by alternating positive and negative oscillations. Their primary role in sediment dislodging is proved by a correlation analysis. Moreover, it could be demonstrated that bed shear stress is mainly linked to the distal transport of sediment.

To estimate the entrainment capacity of a gravity current, ideally all impelling forces should be taken into account. However, the fluctuating nature of the turbulent flow makes impossible a formulation based on all these complex hydrodynamics. Bed shear stress is recognised as the most important of the impelling forces. Since it is correlated with all the other involved forces, it provides a "surrogate measure" of them. In this research project, it could be shown that the bed shear stress gives a good estimation of the entrainment capacity.

The entrainment of sediment in the current may change its momentum by introducing extra internal stresses, thus resulting in a feedback process. The geometry of the front of the gravity current changes with the entrainment of the sediment. This indicates that, with the presence of sediment, extra energy losses occur in the front of the current.

Q6 *How is the downstream deposition of sediment affected by the turbulent structure of the gravity current?*

The presence of near wall turbulent coherent structures inherent to the turbulent flow of the gravity currents imprints the formation of particular deposition patterns. Longitudinal streaks form as the result of the convergence of downwelling flow associated to horseshoe vortexes which consist of a sequence of lifts, stretches, ejection and sweep of fluid. These are characteristic movements of the so-called turbulent bursting events that consists of movements of low-speed fluid ejected away from the wall. The number of streaks and the shape of the streak is related to the type of sediments and the gravity current excess density. It was here proven that greater initial excess density and the presence of coarser material generate less streaks whose section is less elongated indicating that a feedback mechanisms between the coherent

structures generation and the morphology changes of the channel bed may exist.

7.2 Consequences for practical applications

Sediments are brought in huge quantities into the reservoirs by means of turbidity currents. Reservoir sedimentation is therefore intensified, affecting the sustainability of reservoirs by decreasing their storage capacity. Moreover the dam blocks the flux of sediments leading to downstream sediment impoverishment. Thus, proper sediment management techniques have to be adopted in order to find a way for sediment evacuation. This research project has demonstrated that gravity currents are modified by the interaction with sediment composing the bed. The feedback process issues of the interaction with a mobile bed has therefore to be considered for a precise determination of the evolution of the current. Knowing the timing of approach of the turbidity current is fundamental since the flow charged in sediment can be evacuate through the opening of the bottom outlet of the dam (Figure 7.1a) and the lowest possible loss of clear water is suitable.

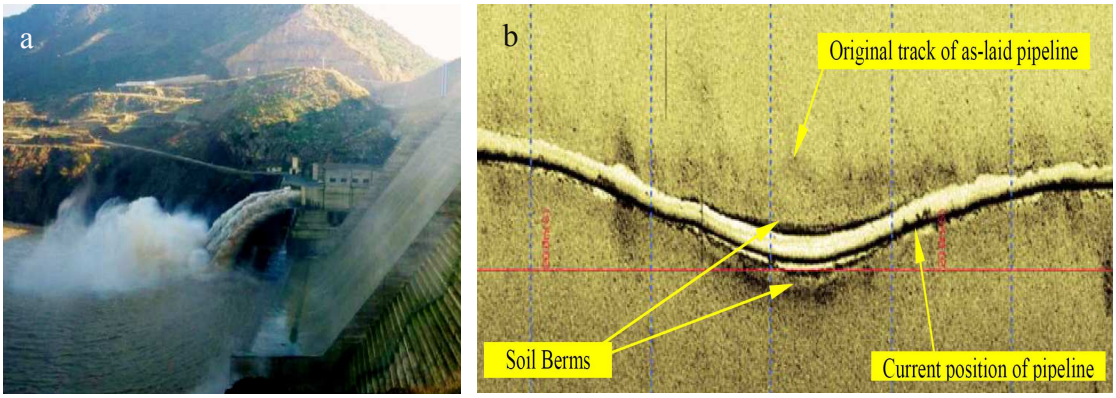

Figure 7.1: a) Venting of turbidity current at Beni Haroun reservoir (Algeria) (Remini and Touimi, 2017); b) Side-scan Sonar Image of a Lateral Buckle (Bruton et al., 2006).

The present research studied the erosion capacity of gravity currents focusing on the forces associated with sediment entrainment. Scour processes, i.e. the removal of sediment operated by the flow, may occur in the vicinity of structures, such as the submarine pipelines situated on the bottom of oceans, and this represents a threat to their stability. Shedding light in the mechanisms which involve sediment erosion operated by gravity currents is therefore of great interest in predicting potential hazard of failure.

Gravity currents can also impact on pipelines. This research has shown that the dynamics of the gravity current are highly dependent on the initial conditions of release which have therefore to be considered when we analyse the effect that an obstacle has on the flow, a

subject that few studies have addressed (Rottman et al. (1985), Oehy and Schleiss (2007), Tokyay et al. (2012), Yaghoubi et al. (2016)).

7.3 Perspectives on future work

Several research challenges could be addressed in forthcoming studies.

First the estimation of bed shear stress could be attempted through detailed velocity measurements in the vicinity of the bed. The experiences made during this research project showed however that these measurements are still a concern even for the most sophisticated instruments. The higher the resolution of the velocity measurements in the logarithmic layer is, the better are the results of the fit of the "law of the wall". High precision of the shear velocity estimation will improve the quantitative estimation of the shear stress and this could be reached by advancements on the technologies for velocity measurement.

The numerical simulation of gravity currents in presence of a mobile bed has been frequently performed by using scalar transport equations. The increased computational power makes nowadays feasible the use of Direct Numerical Simulations (Nasr-Azadani et al., 2016). The use of Lagrangian markers to track the motion of the particles could better reproduce the interaction between gravity current hydrodynamic and sediment, whose mutual feedback has been proved in this research project.

More geometries could be taken into account in the future, such as a wider range of slopes (that were here limited to S≤16%, due to set-up constrains). The steepest slope here reproduced is the transient case for which the effect of extra gravitational forces become evident i.e. the acceleration of the fluid composing the body of the current. The exploration of steeper slopes would confirm the development and enhancement of the mechanisms induced beyond this critical slope.

The investigation of the interaction between gravity currents and subaqueous structures has motivated several recent experimental (Ermanyuk and Gavrilov, 2005) and numerical (Gonzalez-Juez and Meiburg, 2009) investigations. The collision of gravity currents on structures may cause damages. The impacting force is related to the flow hydrodynamics which could possibly be measured experimentally by using a dynamometer force plate. This instrument has the advantage of directly estimate the forces generated due to the impact instead of deriving them from the hydrodynamic measures, as was done in this research.

Venting of turbidity currents is a very efficient mitigation measure against reservoir sedimentation that consists of opening bottom or low-level outlets as soon as the turbidity current reaches the dam in order to pass it downstream (Figure 7.1a). The key factor for this technique is to time correctly the operations of opening and closing the outlet (Chamoun et al., 2017a). Future research on this domain should take into account that the turbidity current, while travelling along the thalweg of the reservoir, interacts with sediments at the bottom. This

research project has shown that the evolution of the gravity currents is modified by the interaction with the sediment composing the bed. Thus future simulations of these phenomena and evaluation of the mitigation measures efficiency should be assessed also in presence of a mobile bed.

Acknowledgements

This research was performed at the Laboratory of Hydraulic Constructions (LCH) of École Polytechnique Fédérale de Lausanne (EPFL). It was funded by the European project SEDITRANS, part of the Marie Curie Actions, FP7-PEOPLE-2013-ITN-607394 (Multi partner - Initial Training Networks).

I would like to acknowledge people who contributed to this research or supported me in any form during these years.

First of all, I would like to thank my thesis director Prof. Dr. Anton J. Schleiss for giving me the opportunity to conduct this research and to join the amazing team he guides. He was source of precious advices and encouragements.

Secondly, I would like to thank my thesis co-director Prof. Dr. Mário J. Franca for the scientific support. With his wealth of ideas he gave me many hints for my research.

I would like to thank Prof. Benjamin Kneller, Dr. Benoit Spinewine, Dr. Damien Bouffard for being part of the jury and Prof. Alfred Johny Wüest for being the president of the jury.

My gratitude goes to Cédric, PanPam, Michel and his team at the workshop, who made from the scratch the channel that is at the 'basement' of this work.

I would like to thank all the amazing LCH team. Scientists and associates, generations of PhDs, host PhDs, secretaries, master students...the family is huge! Everybody enriches this group and let me discover so many interesting new things, on both professional and personal point of views.

Particular thanks to Giovanni, Pedro and Azin, with whom I worked especially due to the teaching assistance task. The care and passion they invest in their job is a reference to me.

I would like to mention some colleagues that, during these years spent shoulder to shoulder, became much more than 'coworkers', they are my friends. Sabine and Mona, my lovely office mates, I loved our office hugs! Sara, Davide, Aldo, Elena and Crispino, the Italian community of the lab, lots of fun and support came from you, grazie! Irene and Pali, third floor (and me) miss you two, let's organise a trip to Lisbon! Zé (and family, I love you very much), Carmelo and Sebastián super post-docs. Herr Sebastian, Nicolas and Pierre, lunch with you was always

better! Ivan and Sev and their endless energy, Stéphane the photo-reporter, Mat, PhD ad honorem, and Alex, Special Envoy of the Académie française.

A big thank to all the friends I've met during these almost four years in Lausanne, with whom I was dancing swing, playing tennis, running, hiking, skiing...EPFL is a broad net of motivated people that offers plenty of opportunities to meet passionate persons.

E ganz grousse Merci to the Lëtzebuerger Frënn both in Lausanne or those who went back to Luxembourg. And Merci to the famiglia Lussemburghese with Viviane, Ger, Paule, les Bomien...who adopted me. I really feel at home when I visit you.

Grazie alla mia bella Tecchia. Jessica ne abbiamo combinate talmente tante insieme! La nostra amicizia resiste inalterata al tempo e alla distanza. Gioia, Lisa, Elena, le mie amiche di sempre, non sapete quanto piacere mi fa rivedervi ogni volta che torno a Valdagno.

Immensa gratitudine va alla mia famiglia. Innanzitutto i nonni: Maria e Francesco che mi hanno cresciuta, nonno Elio e nonna Pina, spero di avere preso un po' del tuo spirito. Sonia, Giorgia, zii e cugini...impossibile fare la lista di tutti, da buona famiglia all'italiana siamo numerosi e...rumorosi! W 'i Zordan!

Un grazie di cuore a mamma Lella, papi Nico e Nicola. Siete la migliore famiglia del mondo, grazie del vostro incondizionato amore e sostegno. Mi mancate davvero tanto!

Dulcis in fundo, merci à mon amore Fränz. Tu es la plus belle surprise que Lausanne m'a réservée, t'avoir rencontré a changé ma vie. Merci pour me pousser toujour à donner mon mieux. Ech hun dech gäer!

Lausanne, 5 janvier 2018 J. Z.

Appendix

A Logarithmic velocity profile method for shear velocity estimation

Newton found by experiment that for a laminar flow, a tangential force (i.e. the force in the direction of the flow) per unit area acting at an arbitrary level within a fluid contained between two rigid horizontal plates, one of which is motionless and the other which is in steady motion, is proportional to the shear of the fluid motion at that level. Mathematically, the law is given by

$$\tau_{xz} = \mu \frac{\partial u}{\partial z} \tag{A.1}$$

where τ_{xz} is the tangential force per unit area, usually called the shear stress; μ a constant of proportionality called the dynamic viscosity; and $\partial u/\partial z$ the shear of the fluid flow normal to the resting plate.

For a turbulent flow, mixing between adjacent layers in the flow involves transfer of momentum via large scale eddies, which impart an extra "eddy viscosity" term that can be considered analogous to momentum transfer by conventional viscosity:

$$\tau = \rho(\nu + K)\frac{\partial u(z)}{\partial z} \approx \rho K \frac{\partial u(z)}{\partial z} \tag{A.2}$$

where $u(z)$ is the mean velocity at elevation z and K is the eddy viscosity which typically is $K >> \nu$.

From Prandtl's mixing length theory:

$$K = l^2 \left| \frac{\partial u(z)}{\partial z} \right| \tag{A.3}$$

where l is a mixing length scaled against elevation by the von Kármán constant: $l = kz$.

Appendix A is based on the scientific article "Bed shear stress estimation for gravity currents performed in laboratory" by J. Zordan, A.J. Schleiss and M.J. Franca published in Proc. of River Flow 2016, St. Louis, USA. The experimental work and the analysis presented hereafter is original and was performed by the author.

Prandtl introduced the concept of "friction velocity" (u_*), which has the dimension of a velocity and it is assumed to be constant near the bed:

$$u_* = \sqrt{\tau_b/\rho} \tag{A.4}$$

with τ_b is the shear stress in the vicinity of the bed.

By combining equations A.2, A.3 and A.4, the shear velocity results:

$$u_* = kz\frac{\partial u(z)}{\partial z} \tag{A.5}$$

Considering the only changing variable z, partial derivative can be substituted by the total one and rearranging Eq.A.5 yields:

$$du = \frac{u_*}{k}\frac{dz}{z} \tag{A.6}$$

Integrating an rearranging terms yields:

$$u(z) = \frac{u_*}{k}lnz + C \tag{A.7}$$

with the boundary condition that $u(z_0) = 0$ then the constant resulting from integration is:

$$C = -\frac{u_*}{k}ln(z_0) \tag{A.8}$$

Hence Eq.A.7 becomes:

$$u(z) = \frac{u_*}{k}ln(z) - \frac{u_*}{k}ln(z_0) = \frac{u_*}{k}ln\frac{z}{z_0} \tag{A.9}$$

This is the "Law of the Wall" that predicts a logarithmic velocity profile at a roughness length scale that defines the height above the bed of z_0. It has the advantage that no independent estimate of z_0 is needed, because u_* only depends on the slope of the profile, not the intercept.

The friction velocity u_* is calculated with the following procedure: (i) the equation of the law of the wall is rewritten as:

$$u(z) = A\ln(z) - B \tag{A.10}$$

where the two coefficients, A and B, are:

$$A = \frac{u_*}{k} \qquad B = \frac{u_*}{k}\ln z_0 \tag{A.11}$$

(ii) the coefficients A and B are determined through a fitting procedure to obtain an estimation of u_*. The identification and fitting procedure for the logarithmic layer was determined stepwise, extending a linear least square fitting range (in a semi-logarithmic scale) from the lowest measured point until the vertical position corresponding to the maximum velocity. The

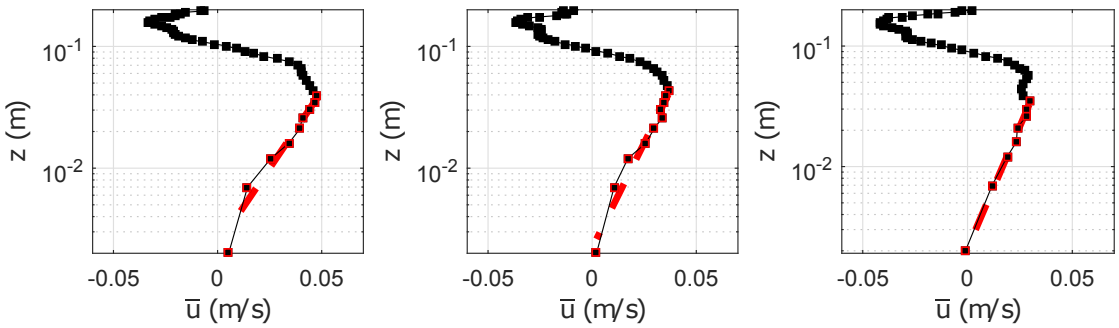

Figure A.1: Logarithmic profile method for some velocity profiles. Data are plotted in a semi-logarithmic graph, u(m/s) streamwise velocity in the x-axis and z(m) on the y-axis. The red dashed line linearly fits the velocity measurements within the determined logarithmic layer.

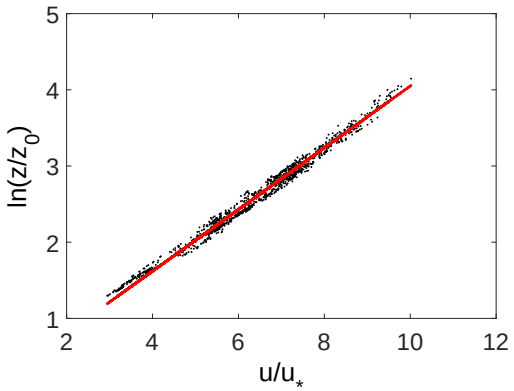

Figure A.2: Collapsed near-bed profiles for one representative test showing the consistency of linear interpolation with slope $1/k$=2.5.

layer providing the best regression coefficient was chosen and considered for the estimation of u_*, corresponding to the extent of the logarithmic layer.

In Figure A.1 the fitting procedure for some velocity profiles is illustrated. The fitting procedure is adopted for each instantaneous profile collected with the ADVP instrumentation zone-averaged over a window long enough to correspond to a quasi-steady region. Thus, an estimation of the bed shear stress is made for each measuring instant.

Figure A.2 shows all the mean velocities as a function of the flow depth within the overlapping layer for the profiles for one representative test. The data collapse linearly when plotting the distance from the bed in the logarithmic scale and it indicates the consistency of the application of the method to the measurements (Sequeiros et al., 2010b).

Some assumptions for the fitting of the logarithmic law of the wall require to be validated after the estimation of the friction velocity. The assumptions checked are: (i) the smooth-wall assumption and (ii) the thickness admitted for the overlapping (logarithmic) layer. The

assumption (i) is verified if the shear Reynolds number (or skin roughness, k_s, normalized by the viscous layer) is in the limit:

$$\frac{k_s u_*}{\nu} \leqslant 5 \tag{A.12}$$

with a considered skin roughness of the channel bottom of k_s=0.2 mm, which corresponds to PVC. The upper limit of the overlapping layer (z_u), within which the data lie on the logarithmic fit, is limit by (Chassaing, 2000):

$$\frac{z_u u_*}{\nu} \leqslant 500 \tag{A.13}$$

so to verify statement (ii).

The value of the von Kármán constant, it's universal nature, Re-independent but wall-dependent or, in general, flow dependent, has been subjected to considerable investigation (Ferreira, 2015). Under clear-water turbulent flow conditions the universal value of 0.405 (Nezu and Rodi, 1986) is accepted being k different in flows with either low submergence or with bed and suspended load transport (Castro-Orgaz et al., 2012) which is not our case as verified in the previous assumptions.

B Acoustic Doppler Velocity Profiler

The 3D Acoustic Doppler Velocity Profiler (ADVP) (Lemmin and Rolland (1997), Franca and Lemmin (2006)) is a non-intrusive sonar instrument that measures the instantaneous velocity profiles using the Doppler effect without the need of calibration. It collects 3D instantaneous velocity measurements during the passage of the density current over a vertical, including the upper counter flow. The instrument consists of a central emitter surrounded by four receivers (Figure B.1). The geometric configuration is the result of an optimization of the instrument that allows noise reduction by creating redundancy information for the velocity components (Blanckaert and Lemmin, 2006). This, together with the despiking procedure proposed by Goring and Nikora (2002), leads to a considerable reduction in the noise level of the data set.

To avoid any interference of the transducer with the flow, measurements are carried out with the transducers mounted above the channel bed in a separate chamber and looking down into the flow. A plastic box was conceived in order to install the instrument immersed in water (in order to avoid a discontinuum on the mean where the sound waves travel). The bottom of the box is sealed with a Mylar film transparent to acoustic waves (Figure B.2). Due to wavelet formation on the water surface, there remains a thin layer near the water surface where no reliable measurements can be taken.

If we consider a simpler ADV configurations with one vertically pointing emitter and receivers inclined at an angle α with respect to the vertical, positioned in a vertical plane placed at an angle β with respect to the (x,z)-plane the following consideration can be done:

- The emitter generates an acoustic wave of frequency f_e and wavelength $\lambda_e = c/f_e$, with c the speed of sound, that propagates through the fluid.

- The wave is scattered by acoustic targets (particles that follow the fluid motion with negligible inertial lag and thus their velocity is assumed to be identical to the fluid velocity) moving with the fluid velocity v, and finally is detected by the receiver. Due to the target velocity v, the wavelength λ_r and the corresponding frequency $f_r = c/\lambda_r$ of the scattered acoustic wave differ from those of the emitted one.

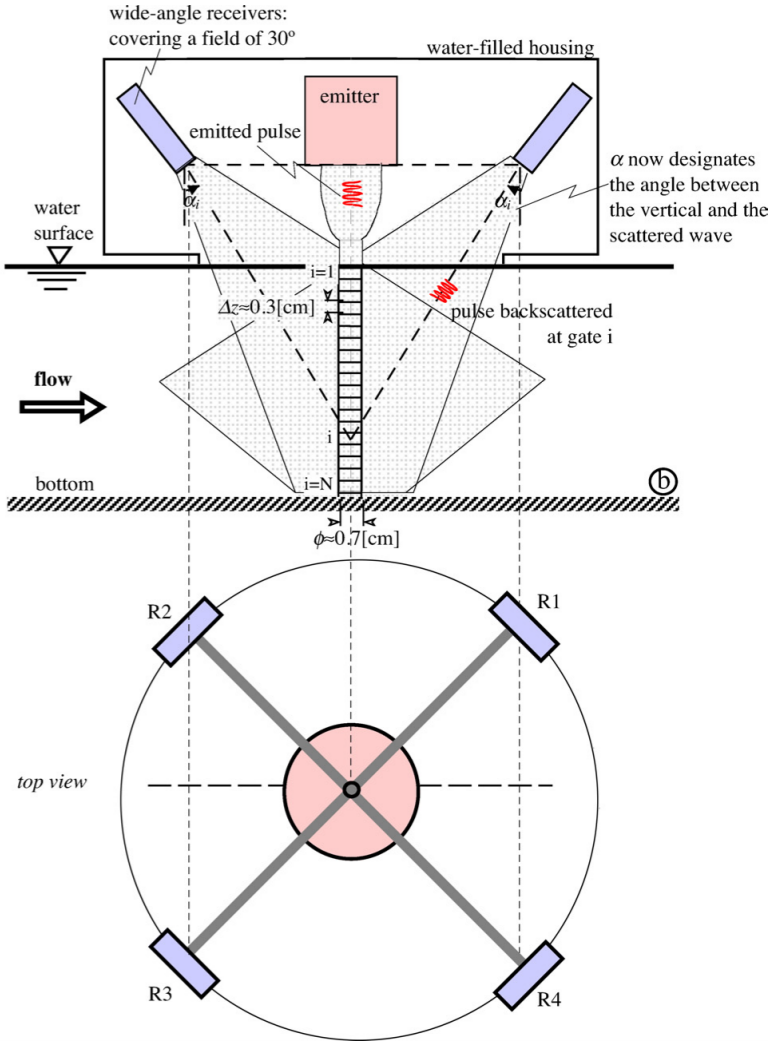

Figure B.1: Schema of the optimized four-receivers symmetrical configuration developed at EPF Lausanne (image by Blanckaert and Lemmin (2006)).

- The Doppler frequency is defined as the frequency shift of the acoustic wave, induced by the moving target, i.e. $f_D = f_r - f_e$. Considering the projections of the target velocity v along the emitter and receiver axes:

$$f_D = \frac{f_e}{c}\left[v_x \cos\beta \sin\alpha + v_y \sin\beta \sin\alpha + v_z(\cos\alpha + 1)\right[\tag{B.1}$$

  where $v = (v_x, v_y, v_z)$ is the target velocity along the axis. This system measures one quasi-instantaneous velocity component, $(c/f_e)f_D$, which is oriented along the bisector of the emitted and the backscattered wavepaths.

For the optimized configuration, as shown in Figure B.2, where $\beta = 45°$ and α depends on the position along the vertical, the system to solve in order to have the estimation of the three

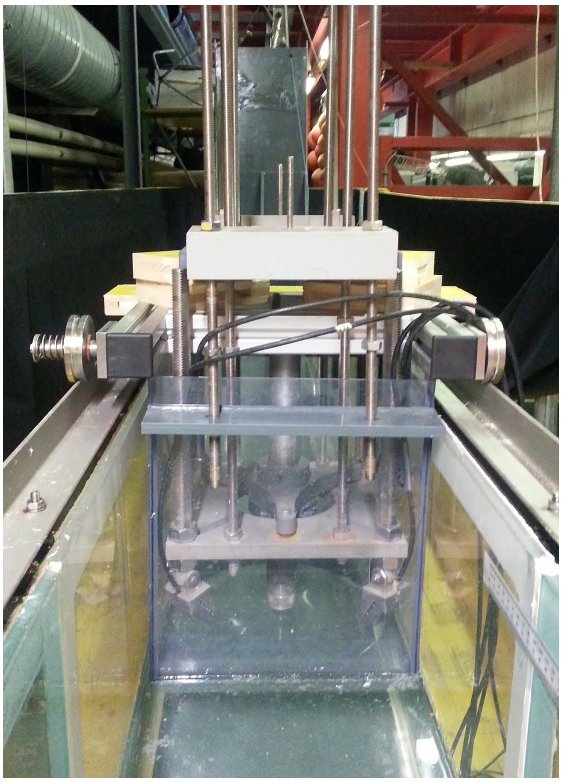

Figure B.2: The ADVP installed in the channel into the transparent plastic box which bottom side in contact with the water surface is covered by Mylar membrane.

components of the velocity is:

$$\begin{bmatrix} \sin\alpha/\sqrt{2} & \sin\alpha/\sqrt{2} & \cos\alpha+1 \\ -\sin\alpha/\sqrt{2} & \sin\alpha/\sqrt{2} & \cos\alpha+1 \\ -\sin\alpha/\sqrt{2} & -\sin\alpha/\sqrt{2} & \cos\alpha+1 \\ \sin\alpha/\sqrt{2} & -\sin\alpha/\sqrt{2} & \cos\alpha+1 \end{bmatrix} \begin{bmatrix} v_x \\ v_y \\ v_z \end{bmatrix} = \frac{c}{f_e} \begin{bmatrix} f_{D1} \\ f_{D2} \\ f_{D3} \\ f_{D4} \end{bmatrix} \tag{B.2}$$

where f_{Di} is the Doppler frequency for the $i-th$ emitter. The solution of the system for the velocities $v = (v_x, v_y, v_z)$ gives therefore three redundancies velocity estimations (Blanckaert and Lemmin, 2006).

A complete profile of the velocity distribution can be obtained by gating the received signals to correspond to the pulse's time of flight to a certain depth. In fact the signal received contains contributions from all density interfaces scattered along the acoustic beam (Figure B.1) that is composed of small sampling volumes, the "gates," which are sampled in sequence forming a profile that is almost instantaneous. The time interval between the emitted pulse and the sample gate increases in proportion to the depth range for which velocity information is sought. To prevent ambiguous range information the echo from the maximum depth of

interest must be allowed to return before the next pulse is emitted.

For studies of turbulent flow, a high sampling frequency is desirable but due to the fact that the maximum measurable Doppler frequency is limited by the pulse repetition frequency at which sound pulses are emitted (Lemmin and Rolland, 1997), a compromise has to be found. Thus the minimum number of pulse-pairs was here fixed at 32, in reason of our working conditions, which corresponds to a frequency of acquisition of 31.25 Hz (Lemmin and Rolland, 1997) being the ADVP operating frequency 1MHz.

C Sediments characterization

The choice of the material is determined in function of many parameters such as the settlement velocity, the total duration of a test, the phenomenon to detect and moreover the availability. The sediment particles chosen fulfil the following requisites: (i) particles small enough to follow the movements of the flow; (ii) particles size compatible with the wavelenght of the emitted ultrasonic waves of the ADVP. The Stokes number is a dimensionless parameter that describes a particle flow in a particular fluid. It is defined as the ratio of the particle response time to the characteristic fluid time scale and is calculated as:

$$Sk = \frac{\rho_s D^2 U}{18 H \nu} \tag{C.1}$$

where ρ_s is the particle density, D is the particle diameter, U the characteristic velocity of the flow, H the characteristic height of the flow and ν the cinematic viscosity of the fluid. In order to assure that particles follow fluid streamlines closely and to have a measure of the interplay between the particles and the fluid, a low value of Stokes number is expected so that the motion of particles and fluid is strongly linked and the suspension behaves as a single phase. In this case it's found to be of the order of 10^{-4}, in agreement with values proposed in Fernando (2012).

The material is a high performance thermoplastic polyurethane (TPU) with a density of $\rho_s = 1160 kg/m^3$.

The first samples received in order to test the suitability of the material was analyzed in collaboration with the Laboratoire de technologie des poudres (LTP) of the EPFL. The laser diffractometer and the optical microscope were used in order to obtain the characteristic granulometric curve of the sample and a view of the particles shape. Two tests with water as mixing liquid and two with isobutanol were made with a Malvern Master sizer laser diffraction particle size analyser (Figure C.1) and the resulted curves are shown in Figure C.2. The distribution widths of the three granulometric curves $((D_{90} - D_{10})/D_{50})$ were checked, and it is < 1.4 for all the grain sizes used, indicating a narrow particle size distribution. The observation of sediment particles under an optical microscope has shown that the grains are irregular

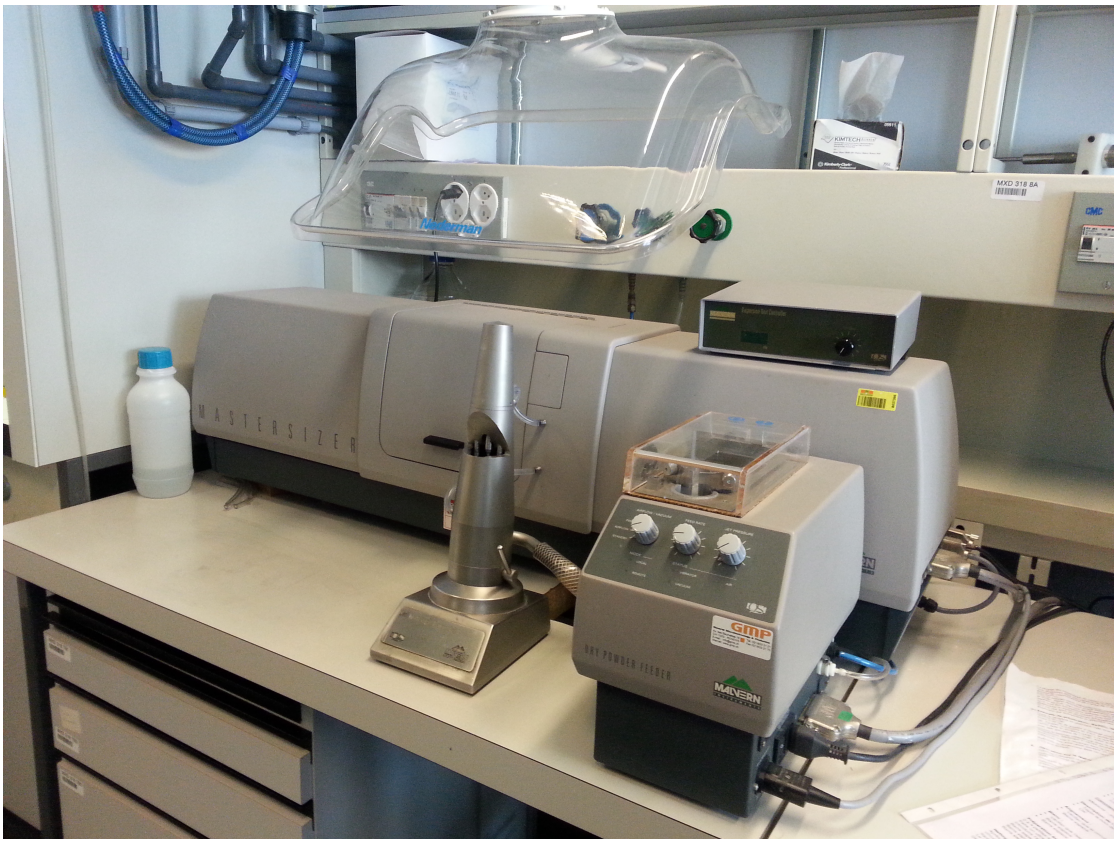

Figure C.1: The Malvern Master sizer laser diffraction particle size analyser at Laboratoire de technologie des poudres (LTP) of the EPF Lausanne.

flakes with squared sides (Figure C.3).

The settling velocity of the particles have been calculated using the Stokes law:

$$v_s = \frac{g D_{50}^2 (\rho_s - \rho_a)}{18\nu} \tag{C.2}$$

giving the following results:

D_{50}	81 μm	145 μm	191 μm
v_s	0.56 mm/s	1.85 mm/s	3.21 mm/s

Table C.1: Settling velocity of the three types of sediments used calculated with Stokes law.

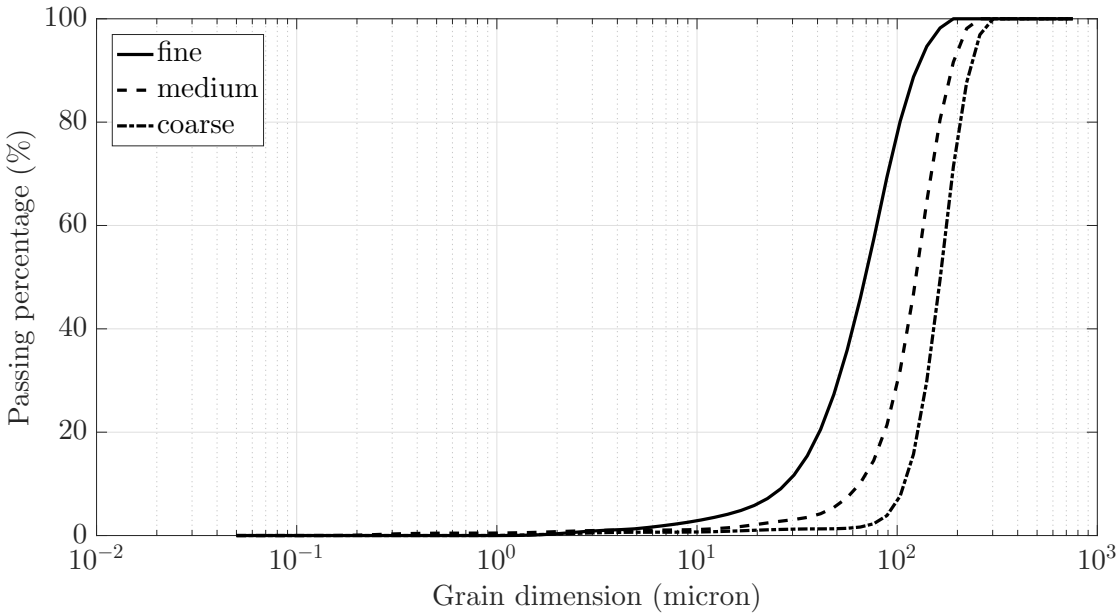

Figure C.2: Granulometric curves of the sediments used to form the erodible reach of the channel bed.

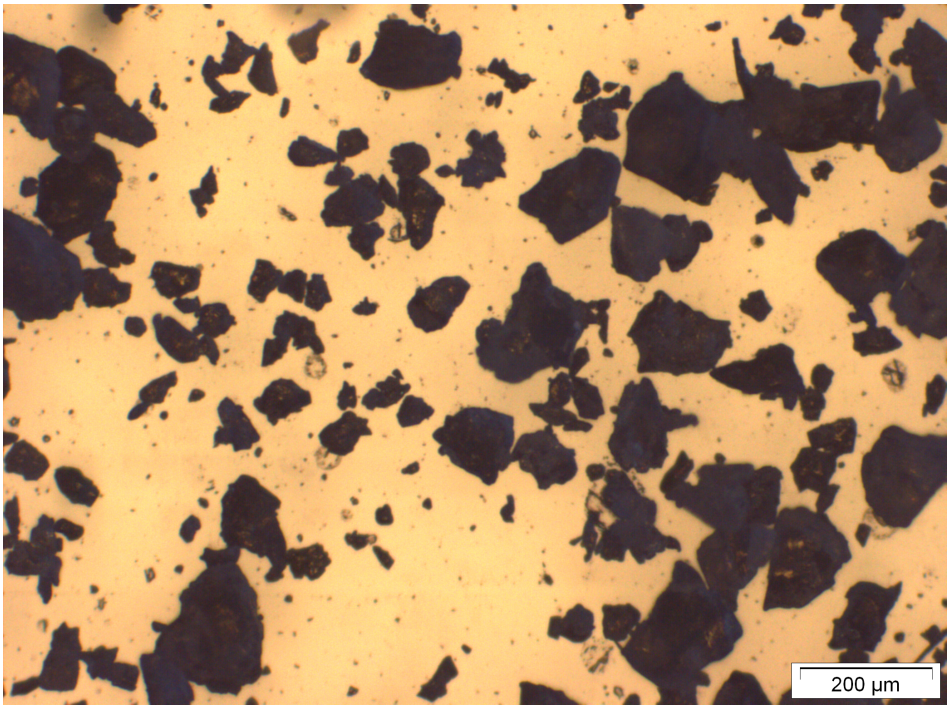

Figure C.3: Photo of the sediments grains taken with an optical microscope.

D Instantaneous velocity measurements

This Appendix contains the instantaneous velocity measurements recorded with the ADVP at some points along the vertical. Both streamwise and vertical components of the velocity are reported for the third group of tests performed (see Chapter 3.2.2 and Table D.1 for details). The measurements here reported are recorded in time at a certain distance from the bottom as defined in Table D.1.

Exp.	ρ_0 (kg/m^3)	g' (m^2/s)
R1.fine	1028	0.29
R1.medium	1028	0.29
R1.coarse	1028	0.29
R2.fine	1038	0.39
R2.medium	1038	0.39
R2.coarse	1038	0.39
R3.fine	1048	0.49
R3.medium	1048	0.49
R3.coarse	1048	0.49

z (m)
0.110
0.101
0.093
0.085
0.076
0.068
0.060
0.052
0.044
0.036
0.028
0.020
0.012
0.004

Table D.1: Experimental parameters of the tests whose raw data are reported in this Appendix (ρ_0 is the initial density of the mixture in the upstream tank (measured with a densimeter) and g' is the reduced gravity corresponding to ρ_0) and distance from the bottom of the records.

One example is presented hereafter for test R1.fine, records at a distance $z = 0.110$ m from the bottom.

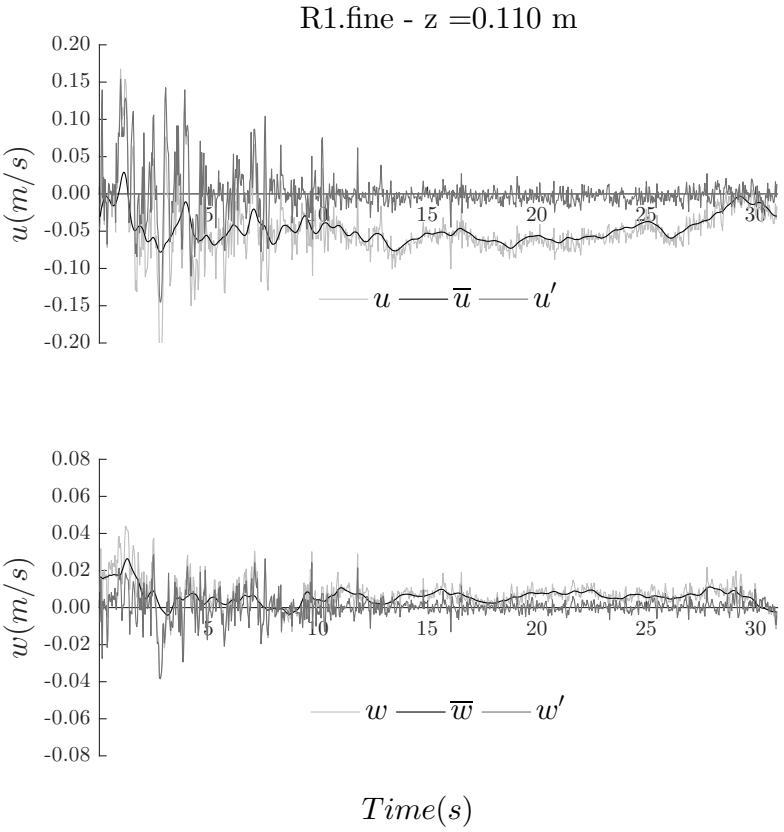

The records for all tests are available on-line (DOI: 10.5075/epfl-thesis-8322) on:

https://infoscience.epfl.ch/

Bibliography

Adduce, C. and Franca, M. J. (2018). Preface. *Environmental Fluid Mechanics*, 18(1):1–2.

Adduce, C., Sciortino, G., and Proietti, S. (2011). Gravity currents produced by lock exchanges: experiments and simulations with a two-layer shallow-water model with entrainment. *Journal of Hydraulic Engineering*, 138(2):111–121.

Ainslie, B. and Jackson, P. (2009). The use of an atmospheric dispersion model to determine influence regions in the Prince George, B.C. airshed from the burning of open wood waste piles. *Journal of Environmental Management*, 90(8):2393–2401.

Akiyama, J. and Stefan, H. (1985). Turbidity current with erosion and deposition. *Journal of Hydraulic Engineering*, 111(12):1473–1496.

Al-Majed, A. A., Adebayo, A. R., and Hossain, M. E. (2012). A sustainable approach to controlling oil spills. *Journal of Environmental Management*, 113:213–227.

Allen, J. (1971). Mixing at turbidity current heads, and its geological implications. *Journal of Sedimentary Research*, 41(1):97–113.

Allen, J. (1984). *Sedimentary Structures: Their Character and Physical Basis*. Number v. 2 in Developments in sedimentology. Elsevier.

Allen, J. (1985). *Principles of physical sedimentology*. Springer Science & Business Media.

Altinakar, M. S., Graf, W. H., and Hopfinger, E. J. (1996). Flow structure in turbidity currents. *Journal of Hydraulic Research*, 34(5):713–718.

Altinakar, S., Graf, W. H., and Hopfinger, E. (1990). Weakly depositing turbidity current on a small slope. *Journal of Hydraulic Research*, 28(1):55–80.

Ancey, C. (2012). Gravity flow on steep slope. pages 372–432. Cambridge University Press New York.

Baas, J. H., McCaffrey, W. D., Haughton, P. D., and Choux, C. (2005). Coupling between suspended sediment distribution and turbulence structure in a laboratory turbidity current. *Journal of Geophysical Research: Oceans*, 110(C11):14095–14111.

Bagherimiyab, F. and Lemmin, U. (2013). Shear velocity estimates in rough-bed open-channel flow. *Earth Surface Processes and Landforms*, 38(14):1714–1724.

Bagnold, R. (1962). Auto-suspension of transported sediment; turbidity currents. *Proceedings of the Royal Society of London. Series A, Mathematical and Physical Sciences*, 265(1322):315–319.

Bates, B., Ancey, C., and Busson, J. (2014). Visualization of the internal flow properties and the material exchange interface in an entraining viscous newtonian gravity current. *Environmental Fluid Mechanics*, 14(2):501–518.

Baumer (2015). Operation and design of photoelectric sensors. *Baumer Catalog*.

Beghin, P., Hopfinger, E., and Britter, R. (1981). Gravitational convection from instantaneous sources on inclined boundaries. *Journal of Fluid Mechanics*, 107:407–422.

Blanckaert, K. (2010). Topographic steering, flow recirculation, velocity redistribution, and bed topography in sharp meander bends. *Water Resources Research*, 46(9).

Blanckaert, K. and Lemmin, U. (2006). Means of noise reduction in acoustic turbulence measurements. *Journal of Hydraulic Research*, 44(1):3–17.

Britter, R. and Linden, P. (1980). The motion of the front of a gravity current travelling down an incline. *Journal of Fluid Mechanics*, 99(03):531–543.

Britter, R. and Simpson, J. (1978). Experiments on the dynamics of a gravity current head. *Journal of Fluid Mechanics*, 88(02):223–240.

Bruton, D., White, D., Cheuk, C., Bolton, M., Carr, M., et al. (2006). Pipe/soil interaction behavior during lateral buckling, including large-amplitude cyclic displacement tests by the safebuck jip. In *Offshore Technology Conference*. Offshore Technology Conference.

Cantero, M. I., Balachandar, S., García, M. H., and Bock, D. (2008). Turbulent structures in planar gravity currents and their influence on the flow dynamics. *Journal of Geophysical Research: Oceans*, 113(C8).

Castro-Orgaz, O., Giráldez, J. V., Mateos, L., and Dey, S. (2012). Is the von Kármán constant affected by sediment suspension? *Journal of Geophysical Research: Earth Surface*, 117(F4).

Chamoun, S., De Cesare, G., and Schleiss, A. J. (2016a). Managing reservoir sedimentation by venting turbidity currents: a review. *International Journal of Sediment Research*, 31(3):195–204.

Chamoun, S., De Cesare, G., and Schleiss, A. J. (2017a). Management of turbidity current venting in reservoirs under different bed slopes. *Journal of Environmental Management*, 204:519–530.

Chamoun, S., De Cesare, G., and Schleiss, A. J. (2017b). Venting of turbidity currents approaching a rectangular opening on a horizontal bed. *Journal of Hydraulic Research*, pages 1–15.

Chamoun, S., Zordan, J., De Cesare, G., and Franca, M. J. (2016b). Measurement of the deposition of fine sediments in a channel bed. *Flow Measurement and Instrumentation*, 50:49–56.

Chassaing, P. (2000). *Turbulence en mécanique des fluides*. Cépaduès éditions.

Chassaing, P. (2010). *Mécanique des fluides*. Cepadues éditions.

Chikita, K. (1990). Sedimentation by river-induced turbidity currents: field measurements and interpretation. *Sedimentology*, 37(5):891–905.

Chikita, K. A., Smith, N. D., Yonemitsu, N., and PEREZ-ARLUCEA, M. (1996). Dynamics of sediment-laden underflows passing over a subaqueous sill: glacier-fed peyto lake, alberta, canada. *Sedimentology*, 43(5):865–875.

Colombini, M. and Parker, G. (1995). Longitudinal streaks. *Journal of Fluid Mechanics*, 304:161–183.

Cossu, R. and Wells, M. G. (2012). A comparison of the shear stress distribution in the bottom boundary layer of experimental density and turbidity currents. *European Journal of Mechanics, B/Fluids*, 32(1):70–79.

Csanady, G. T. (1978). Turbulent interface layers. *Journal of Geophysical Research: Oceans*, 83(C5):2329–2342.

Dai, A. (2013). Experiments on gravity currents propagating on different bottom slopes. *Journal of Fluid Mechanics*, 731:117–141.

De Cesare, G. and Schleiss, A. (1998). *Alluvionnement des retenues par courants de turbidité*. Communication LCH N°7: Laboratoire de constructions hydrauliques, Ecole Polytechnique Fédérale de Lausanne. Editeur: Prof. Dr A. Schleiss.

De Cesare, G.and Beyer Portner, N. A., Boillat, J.-L., and Schleiss, A. (1998). Modelling of erosion and sedimentation based on field investigation in Alpine hydropower schemes. *Journal of Proceedings of Abstracts and Papers , 3rd International Conference on Hydroscience and Engineering, Cottbus/Berlin Mechanics*, 3.

Defina, A. (1996). Transverse spacing of low-speed streaks in a channel flow over a rough bed. *Coherent flow structures in open channels*, 4:87–99.

Dey, S. (2014). *Fluvial Hydrodynamics*. Springer.

Dietrich, W. E. (1982). Settling velocity of natural particles. *Water resources research*, 18(6):1615–1626.

Eames, I., Hogg, A. J., Gething, S., and Dalziel, S. B. (2001). Resuspension by saline and particle-driven gravity currents. *Journal of Geophysical Research: Oceans*, 106(C7):14095–14111.

Ellison, T. and Turner, J. (1959). Turbulent entrainment in stratified flows. *Journal of Fluid Mechanics*, 6(03):423–448.

Ermanyuk, E. and Gavrilov, N. (2005). Interaction of internal gravity current with an obstacle on the channel bottom. *Journal of Applied Mechanics and Technical Physics*, 46(4):489–495.

Fer, I., Lemmin, U., and Thorpe, S. (2002). Winter cascading of cold water in lake geneva. *Journal of Geophysical Research: Oceans*, 107(C6).

Fernández-Torquemada, Y., Gónzalez-Correa, J. M., Loya, A., Ferrero, L. M., Díaz-Valdés, M., and Sánchez-Lizaso, J. L. (2009). Dispersion of brine discharge from seawater reverse osmosis desalination plants. *Desalination and Water Treatment*, 5(1-3):137–145.

Fernando, H. (2012). *Handbook of Environmental Fluid Dynamics, Volume One: Overview and Fundamentals*. Environmental science and engineering / [CRC press]. Taylor & Francis.

Ferreira, R. M. (2015). The von Kármán constant for flows over rough mobile beds. lessons learned from dimensional analysis and similarity. *Advances in Water Resources*, 81:19–32.

Ferreira, R. M., Franca, M. J., Leal, J. G., and Cardoso, A. H. (2012). Flow over rough mobile beds: Friction factor and vertical distribution of the longitudinal mean velocity. *Water Resources Research*, 48(5).

Fragoso, A., Patterson, M., and Wettlaufer, J. (2013). Mixing in gravity currents. *Journal of Fluid Mechanics*, 734.

Franca, M. and Lemmin, U. (2006). Eliminating velocity aliasing in acoustic doppler velocity profiler data. *Measurement Science and Technology*, 17(2):313.

Franca, M. J. (23-26 May 2017). Density currents: theory and experimental results. XXXVI International School of Hydraulics, Jachranka, Poland.

Franca, M. J. and Brocchini, M. (2015). Turbulence in rivers. In *Rivers–Physical, Fluvial and Environmental Processes*, pages 51–78. Springer.

García, M. and Parker, G. (1993). Experiments on the entrainment of sediment into suspension by a dense bottom current. *Journal of Geophysical Research: Oceans*, 98:4793–4807.

Gladstone, C., Phillips, J., and Sparks, R. (1998). Experiments on bidisperse, constant-volume gravity currents: propagation and sediment deposition. *Sedimentology*, 45(5):833–843.

Gonzalez, R. C. and Woods, R. E. (2007). Image processing. *Digital Image Processing*, 2.

Gonzalez-Juez, E. and Meiburg, E. (2009). Shallow-water analysis of gravity-current flows past isolated obstacles. *Journal of Fluid Mechanics*, 635:415–438.

Goring, D. G. and Nikora, V. I. (2002). Despiking acoustic doppler velocimeter data. *Journal of Hydraulic Engineering*, 128(1):117–126.

Graf, W. H. A. et al. (1998). *Fluvial hydraulics: Flow and transport processes in channels of simple geometry*. Number 551.483 G7.

Grass, A. J. (1971). Structural features of turbulent flow over smooth and rough boundaries. *Journal of Fluid Mechanics*, 50(02):233–255.

Hacker, J. and Linden, P. (2002). Gravity currents in rotating channels. Part 1. Steady-state theory. *Journal of Fluid Mechanics*, 457:295–324.

Hacker, J., Linden, P., and Dalziel, S. (1996). Mixing in lock-release gravity currents. *Dynamics of Atmospheres and Oceans*, 24(1-4):183–195.

Hallworth, M. A., Huppert, H. E., Phillips, J. C., and Sparks, R. S. J. (1996). Entrainment into two-dimensional and axisymmetric turbulent gravity currents. *Journal of Fluid Mechanics*, 308:289–311.

Hallworth, M. A., Phillips, J. C., Huppert, H. E., and Sparks, R. S. J. (1993). Entrainment in turbulent gravity currents. *Nature*, 362(6423):829–831.

Heezen, B. C., Ericson, D., and Ewing, M. (1954). Further evidence for a turbidity current following the 1929 Grand Banks earthquake. *Deep Sea Research (1953)*, 1(4):193–202.

Herzog, H., Caldeira, K., and Adams, E. (2001). Carbon sequestration via direct injection. *Encyclopedia of Ocean Sciences-*, 1:408–414.

Hickin, E. J. (1995). *River Geomorphology*. John Wiley & Sons.

Hirano, M., Hadano, K., and Matsuo, T. (1985). Motion of the head of a gravity current with pick up and deposition of particles. *Journal of the Sedimentological Society of Japan*, 22(22-23):8–15.

Hodges, B. R., Furnans, J. E., and Kulis, P. S. (2010). Thin-layer gravity current with implications for desalination brine disposal. *Journal of Hydraulic Engineering*, 137(3):356–371.

Hogg, A. J. (2006). Lock-release gravity currents and dam-break flows. *Journal of Fluid Mechanics*, 569:61–87.

Huppert, H. E. (2006). Gravity currents: a personal perspective. *Journal of Fluid Mechanics*, 554:299–322.

Huppert, H. E. and Simpson, J. E. (1980). The slumping of gravity currents. *Journal of Fluid Mechanics*, 99(04):785–799.

Huppert, H. E. and Woods, A. W. (1995). Gravity-driven flows in porous layers. *Journal of Fluid Mechanics*, 292(1):55.

Hurther, D. and Lemmin, U. (2000). Shear stress statistics and wall similarity analysis in turbulent boundary layers using a high-resolution 3-d advp. *IEEE Journal of Oceanic Engineering*, 25(4):446–457.

Hurther, D. and Lemmin, U. (2001). A correction method for turbulence measurements with a 3d acoustic doppler velocity profiler. *Journal of Atmospheric and Oceanic Technology*, 18(3):446–458.

Imran, J., Khan, S. M., Pirmez, C., and Parker, G. (2017). Froude scaling limitations in modeling of turbidity currents. *Environmental Fluid Mechanics*, 17:159–186.

Jiménez, J. A. and Madsen, O. S. (2003). A simple formula to estimate settling velocity of natural sediments. *Journal of waterway, port, coastal, and ocean engineering*, 129(2):70–78.

Johnson, C. G. and Hogg, A. J. (2013). Entraining gravity currents. *Journal of Fluid Mechanics*, 731:477–508.

Kaftori, D., Hetsroni, G., and Banerjee, S. (1995). Particle behavior in the turbulent boundary layer. I. Motion, deposition, and entrainment. *Physics of Fluids*, 7(5):1095–1106.

Keulegan, G. (1957). An experimental study of the motion of saline water from locks into fresh water channels. *Nat. Bur. Stand. Rept. Technical Report*, 5168.

Khavasi, E., Afshin, H., and Firoozabadi, B. (2012). Effect of selected parameters on the depositional behaviour of turbidity currents. *Journal of Hydraulic Research*, 50(1):60–69.

Kim, H., Kline, S., and Reynolds, W. (1971). The production of turbulence near a smooth wall in a turbulent boundary layer. *Journal of Fluid Mechanics*, 50(1):133–160.

Kline, S., Reynolds, W., Schraub, F., and Runstadler, P. (1967). The structure of turbulent boundary layers. *Journal of Fluid Mechanics*, 30(04):741–773.

Kneller, B., Bennett, S., and McCaffrey, W. (1997). Velocity and turbulence structure of density currents and internal solitary waves: potential sediment transport and the formation of wave ripples in deep water. *Sedimentary Geology*, 112(3):235–250.

Kneller, B. and Buckee, C. (2000). The structure and fluid mechanics of turbidity currents: a review of some recent studies and their geological implications. *Sedimentology*, 47:62–94.

Kneller, B. C., Bennett, S. J., and McCaffrey, W. D. (1999). Velocity structure, turbulence and fluid stresses in experimental gravity currents. *Journal of Geophysical Research: Oceans*, 104(C3):5381–5391.

Knoblauch, H. (1999). Overview of density flows and turbidity currents. Water Resources Research Laboratory, United States Bureau of Reclamation.

Kyrousi, F., Leonardi, A., Juez, C., Zordan, J., Zanello, F., F, R., Armenio, V., and Franca, M. J. (2017a). Numerical simulations of sediment entrainment by lock-exchange gravity currents. IAHR 2017, Book of abstracts, Kuala-Lumpur, Malaysia.

Kyrousi, F., Leonardi, A., Roman, F., Armenio, V., Zanello, F. V., Zordan, J., Juez, C., and Falcomer, L. (2017b). Large eddy simulations of sediment entrainment induced by a lock-exchange gravity current. *Journal of Water Resources*, accepted for publication.

Kyrousi, F., Zordan, J., Leonardi, A., Juez, C., Zanello, F., Armenio, V., and Franca, M. J. (2017c). Large eddy simulations of compositional density currents flowing over a mobile bed. EGU 2017, Book of abstracts, Vienna, Austria.

Lamb, M. P., Dietrich, W. E., and Venditti, J. G. (2008). Is the critical Shields stress for incipient sediment motion dependent on channel-bed slope? *Journal of Geophysical Research: Earth Surface*, 113(F2).

Lemmin, U. and Rolland, T. (1997). Acoustic velocity profiler for laboratory and field studies. *Journal of Hydraulic Engineering*, 123(12):1089–1098.

Lofquist, K. (1960). Flow and stress near an interface between stratified liquids. *The Physics of Fluids*, 3(2):158–175.

Lombardi, V., Adduce, C., Sciortino, G., and La Rocca, M. (2015). Gravity currents flowing upslope: laboratory experiments and shallow-water simulations. *Physics of Fluids*, 27(1):016602.

Lyn, D., Stamou, A., and Rodi, W. (1992). Density currents and shear-induced flocculation in sedimentation tanks. *Journal of Hydraulic Engineering*, 118(6):849–867.

Maini, R. and Aggarwal, H. (2010). A comprehensive review of image enhancement techniques. *Journal of Computing*, 2(3):8–13.

Manica, R. (2012). Sediment gravity flows: study based on experimental simulations. In *Hydrodynamics-Natural Water Bodies*. InTech.

Maxworthy, T. (2010). Experiments on gravity currents propagating down slopes. Part 2. The evolution of a fixed volume of fluid released from closed locks into a long, open channel. *Journal of Fluid Mechanics*, 647:27–51.

Maxworthy, T. and Nokes, R. (2007). Experiments on gravity currents propagating down slopes. Part 1. The release of a fixed volume of heavy fluid from an enclosed lock into an open channel. *Journal of Fluid Mechanics*, 584:433–453.

Meiburg, E. and Kneller, B. (2010). Turbidity currents and their deposits. *Annual Review of Fluid Mechanics*, 42:135–156.

Middleton, G. (1993). Sediment Deposition from Turbidity Currents. *Annual Review of Earth and Planetary Sciences*, 21(1):89–114.

Nasr-Azadani, M. M., Meiburg, E., and Kneller, B. (2016). Mixing dynamics of turbidity currents interacting with complex seafloor topography. *Environmental Fluid Mechanics*, pages 1–23.

Nezu, I. and Rodi, W. (1986). Open-channel flow measurements with a laser doppler anemometer. *Journal of Hydraulic Engineering*, 112(5):335–355.

Niño, Y. and Garcia, M. (1996). Experiments on particle-turbulence interactions in the near-wall region of an open channel flow: implications for sediment transport. *Journal of Fluid Mechanics*, 326:285–319.

Nogueira, H. I. S., Adduce, C., Alves, E., and Franca, M. J. (2013). Analysis of lock-exchange gravity currents over smooth and rough beds. *Journal of Hydraulic Research*, 51(4):417–431.

Nogueira, H. I. S., Adduce, C., Alves, E., and Franca, M. J. (2014a). Dynamics of the head of gravity currents. *Environmental Fluid Mechanics*, 14(2):519–540.

Nogueira, H. I. S., Adduce, C., Alves, E., and Franca, M. J. (2014b). Dynamics of the head of gravity currents. *Environmental Fluid Mechanics*, 14(2):519–540.

Oehy, C. D. and Schleiss, A. J. (2007). Control of turbidity currents in reservoirs by solid and permeable obstacles. *Journal of Hydraulic Engineering*, 133(6):637–648.

Ooi, S. K., Constantinescu, G., and Weber, L. (2009). Numerical simulations of lock-exchange compositional gravity current. *Journal of Fluid Mechanics*, 635:361–388.

Ottolenghi, L., Adduce, C., Inghilesi, R., Armenio, V., and Roman, F. (2016a). Entrainment and mixing in unsteady gravity currents. *Journal of Hydraulic Research*, 54(5):541–557.

Ottolenghi, L., Adduce, C., Inghilesi, R., Roman, F., and Armenio, V. (2016b). Mixing in lock-release gravity currents propagating up a slope. *Physics of Fluids*, 28(5):056604.

Palmieri, A., Shah, F., and Dinar, A. (2001). Economics of reservoir sedimentation and sustainable management of dams. *Journal of Environmental Management*, 61(2):149–163.

Parker, G. (1982). Conditions for the ignition of catastrophically erosive turbidity currents. *Marine Geology*, 46(3-4):307–327.

Parker, G., Fukushima, Y., and Pantin, H. M. (1986). Self-accelerating turbidity currents. *Journal of Fluid Mechanics*, 171:145–181.

Parker, G., Garcia, M., Fukushima, Y., and Yu, W. (1987). Experiments on turbidity currents over an erodible bed. *Journal of Hydraulic Research*, 25(1):123–147.

Paull, C., Ussler, W., Greene, H., Keaten, R., Mitts, P., and Barry, J. (2002). Caught in the act: the 20 December 2001 gravity flow event in Monterey Canyon. *Geo-Marine Letters*, 22(4):227–232.

Pennekamp, F. and Schtickzelle, N. (2013). Implementing image analysis in laboratory-based experimental systems for ecology and evolution: a hands-on guide. *Methods in Ecology and Evolution*, 4(5):483–492.

Piper, D. J., Shor, A. N., Farre, J. A., O'Connell, S., and Jacobi, R. (1985). Sediment slides and turbidity currents on the Laurentian Fan: sidescan sonar investigations near the epicenter of the 1929 Grand Banks earthquake. *Geology*, 13(8):538–541.

Podczeck, F. (1997). A shape factor to assess the shape of particles using image analysis. *Powder Technology*, 93(1):47–53.

Raffel, M., Willert, C. E., Wereley, S., and Kompenhans, J. (2013). *Particle image velocimetry: a practical guide*. Springer.

Ramšak, V., Malačič, V., Ličer, M., Kotnik, J., Horvat, M., and Žagar, D. (2013). High-resolution pollutant dispersion modelling in contaminated coastal sites. *Environmental Research*, 125:103–112.

Rastello, M. and Hopfinger, E. (2004). Sediment-entraining suspension clouds: a model of powder-snow avalanches. *Journal of Fluid Mechanics*, 509:181–206.

Remini, B. and Touimi, A. (2017). The Beni Haroun reservoir (Algeria) is it threatened by siltation? *LARHYSS Journal ISSN 1112-3680*, (29):249–263.

Roman, F., Stipcich, G., Armenio, V., Inghilesi, R., and Corsini, S. (2010). Large eddy simulation of mixing in coastal areas. *International Journal of Heat and Fluid Flow*, 31(3):327–341.

Ross, A. N., Linden, P., and Dalziel, S. B. (2002). A study of three-dimensional gravity currents on a uniform slope. *Journal of Fluid Mechanics*, 453:239–261.

Rottman, J. W., Simpson, J. E., Hunt, J., and Britter, R. (1985). Unsteady gravity current flows over obstacles: some observations and analysis related to the phase II trials. *Journal of Hazardous Materials*, 11:325–340.

Salim, S., Pattiaratchi, C., Tinoco, R., Coco, G., Hetzel, Y., Wijeratne, S., and Jayaratne, R. (2017). The influence of turbulent bursting on sediment resuspension under unidirectional currents. *Earth Surface Dynamics*, 5(3):399.

Schleiss, A. J., Franca, M. J., Juez, C., and De Cesare, G. (2016). Reservoir sedimentation. *Journal of Hydraulic Research*, 54(6):595–614.

Sequeiros, O. E., Spinewine, B., Beaubouef, R. T., Sun, T., Garcia, M. H., and Parker, G. (2010a). Bedload transport and bed resistance associated with density and turbidity currents. *Sedimentology*, 57(6):1463–1490.

Sequeiros, O. E., Spinewine, B., Beaubouef, R. T., Sun, T., García, M. H., and Parker, G. (2010b). Characteristics of velocity and excess density profiles of saline underflows and turbidity currents flowing over a mobile bed. *Journal of Hydraulic Engineering*, 136(7):412–433.

Serra, T., Ros, A., Vergés, C., and Casamitjana, X. (2017). Influence of a flooding event discharge on accretion in wetlands. *Environmental Fluid Mechanics*, pages 1–19.

Shields, A. (1936a). Anwendung der Aehnlichkeitsmechanik und der Turbulenzforschung auf die Geschiebebewegung, Heft:26. *PhD Thesis, Technical University Berlin*.

Shields, A. (1936b). Application of similarity principles and turbulence research to bed-load movement. Technical report, Soil Conservation Service.

Shin, J., Dalziel, S., and Linden, P. (2004). Gravity currents produced by lock exchange. *Journal of Fluid Mechanics*, 521:1–34.

Simpson, J. and Britter, R. (1979). The dynamics of the head of a gravity current advancing over a horizontal surface. *Journal of Fluid Mechanics*, 94(03):477–495.

Simpson, J. E. (1972). Effects of the lower boundary on the head of a gravity current. *Journal of Fluid Mechanics*, 53(04):759–768.

Simpson, J. E. (1997). *Gravity currents: in the environment and the laboratory*. Cambridge University Press.

Simpson, J. E. and Linden, P. F. (1989). Frontogenesis in a fluid with horizontal density gradients. *Journal of Fluid Mechanics*, 202:1–16.

Stagnaro, M. and Pittaluga, M. B. (2014). Velocity and concentration profiles of saline and turbidity currents flowing in a straight channel under quasi-uniform conditions. *Earth Surface Dynamics*, 2(1):167.

Sveen, J. K. (2004). An introduction to MatPIV v. 1.6. 1. *Preprint series. Mechanics and Applied Mathematics*.

Theiler, Q. and Franca, M. J. (2016). Contained density currents with high volume of release. *Sedimentology*, 63(6):1820–1842.

Tokyay, T., Constantinescu, G., and Meiburg, E. (2011). Lock-exchange gravity currents with a high volume of release propagating over a periodic array of obstacles. *Journal of Fluid Mechanics*, 672:570–605.

Tokyay, T., Constantinescu, G., and Meiburg, E. (2012). Tail structure and bed friction velocity distribution of gravity currents propagating over an array of obstacles. *Journal of Fluid Mechanics*, 694:252–291.

Turner, J. S. (1973a). *Buoyancy effects in fluids*. Cambridge University Press.

Turner, J. S. (1973b). Turbulent shear flows in a stratified fluid. In *Buoyancy Effects in Fluids*, Cambridge Monographs on Mechanics, pages 127–164. Cambridge University Press.

Ungarish, M. (2012). Gravity currents and intrusions. In *Handbook of Environmental Fluid Dynamics,Volume One.*, pages 361–375.

Valle-Levinson, A. (2010). *Contemporary issues in estuarine physics*. Cambridge University Press.

Van Rijn, L. C. (2007). Unified view of sediment transport by currents and waves. I: Initiation of motion, bed roughness, and bed-load transport. *Journal of Hydraulic Engineering*, 133(6):649–667.

Vetsch, D., Siviglia, A., Ehrbar, D., Facchini, M., Gerber, M., Kammerer, S., Peter, S., Vonwiller, L., Volz, C., Farshi, D., Mueller, R., Rousselot, P., Veprek, R., and Faeh, R. (2015). *System Manuals of BASEMENT, Version 2.1*. http://www.basement.ethz.ch/.

Von Kármán, T. (1940). The engineer grapples with nonlinear problems. *Bulletin of the American Mathematical Society*, 46(8):615–683.

Weill, M.-E., Rhazi, M., and Gouesbet, G. (1985). Experimental investigation of oscillatory phenomena produced by a hot wire located near and below a free surface. *Journal de Physique*, 46(9):1501–1506.

Whitham, G. and Fowler, R. G. (1975). Linear and nonlinear waves. *Physics Today*, 28:55.

Wirth, A. (2015). A guided tour through buoyancy driven flows and mixing. Master. *Buoyancy Driven Flows and Mixing, France. pp.68.*

Xu, J., Noble, M., and Rosenfeld, L. K. (2004). In-situ measurements of velocity structure within turbidity currents. *Geophysical Research Letters*, 31(9).

Yaghoubi, S., Afshin, H., Firoozabadi, B., and Farizan, A. (2016). Experimental investigation of the effect of inlet concentration on the behavior of turbidity currents in the presence of two consecutive obstacles. *Journal of Waterway, Port, Coastal, and Ocean Engineering*, 143(2):04016018.

Yang, S.-Q., Dharmasiri, N., and Han, Y. (2012). Momentum balance method and estimation of boundary shear stress distribution. *Journal of Hydraulic Engineering*, 138(7):657–660.

Zhou, S., McCorquodale, J., and Godo, A. (1994). Short circuiting and density interface in primary clarifiers. *Journal of Hydraulic Engineering*, 120(9):1060–1080.

Communications du Laboratoire de Constructions Hydrauliques ISSN 1661-1179
Ecole Polytechnique Fédérale de Lausanne
Editeur: Prof. Dr A. Schleiss

N° 62 2016 M. Jafarnejad Chaghooshi
Time-dependent failure analysis of large block size riprap as bank protection in mountain rivers

N° 63 2016 S. Terrier
Hydraulic performance of stepped spillway aerators and related downstream flow features

N° 64 2016 M. Ostad Mirza
Experimental study on the influence of abrupt slope changes on flow characteristics over stepped spillways

N° 65 2016 I. Almeida Samora
Optimization of low-head hydropower recovery in water supply networks

N° 66 2016 D. Ferràs Segura
Fluid-structure interaction during hydraulic transients in pressurized pipes: experimental and numerical analyses

N° 67 2016 E. Battisacco
Replenishment of sediment downstream of dams: Erosion and transport processes

N° 68 2017 F. Zeimetz
Development of a methodology for extreme flood estimations in alpine catchments for the verification of dam safety

N° 69 2017 A. J. Pachoud
Influence of geometrical imperfections and flaws at welds of steel liners on fatigue behavior of pressure tunnels and shafts in anisotropic rock

N° 70 2017 F. Oberrauch
Hydropower design under uncertainties

N° 71 2017 S. Schwindt
Hydro-morphological processes through permeable sediment traps at mountain rivers

N° 72 2017 S. Chamoun
Influence of outlet discharge on the efficiency of turbidity current venting

N° 73 2017 N. J. Adam
Characterization of hydraulic behavior of orifices in conduits

N° 74 2018 D. Wüthrich
Extreme Hydrodynamic impact onto buildings

N° 75 2018 J. Zordan
Geomorphic work by gravity currents with varying initial conditions

ISSN 1661-1179

DOI: 10.5075/epfl-lchcomm-75

Prof. Dr A. Schleiss
Laboratoire de constructions hydrauliques - LCH
EPFL, Bât. GC, Station 18, CH-1015 Lausanne
http://lch.epfl.ch
e-mail: secretariat.lch@epfl.ch